Università degli Studi di Napoli Federico II

SCUOLA POLITECNICA E DELLE SCIENZE DI BASE

Dipartimento di Scienze della Terra, dell'Ambiente e delle Risorse

Corso di Dottorato in Scienze della Terra

Holocene vertical deformation in the offshore sector of the Campi Flegrei caldera based on seismo-stratigraphic and archaeological sea-level markers

PhD Dissertation

Camilla Marino

Tutor: Prof. Luigi Ferranti

Co-Tutor: Dr. Marco Sacchi

Thesis abstract

Rapid, positive and negative ground movements have been observed since historical time and are documented in the geological record in the coastal part of the Campi Flegrei caldera (Campanian region, Southern Italy), which formed as a consequence of the 15 ka Neapolitan Yellow Tuff (NYT) eruption. Several reconstructions of ground movements associated with ground uplift and subsidence were proposed based on volcanological and geo-archaeological observations onshore; however, the offshore deformation pattern remains poorly constrained. The southern sector of the caldera, which represents over one-third of its area, is submerged beneath the Pozzuoli Bay and includes part of the resurgent dome developed inside the caldera. Due to its history of large-scale explosive eruptions, ongoing episodes of unrest, and high population density living in the close vicinity, the Campi Flegrei caldera represents one of the world's maximum volcanic risk areas.

The current thesis is based on high-resolution multichannel seismic reflection data acquired in the offshore sector of the Campi Flegrei caldera and nearby the Gulf of Naples. Analysis of high-resolution seismic profiles integrated with coastal archaeological data has allowed the first quantitative reconstruction of long-term (~18 ka) ground deformation in the offshore part of the Campi Flegrei resurgent caldera and its peripheral areas.

The submerged caldera infill preserves the seismic record to decipher the volcano-tectonic evolution, outlining the interplay with sea level variations. The present study uses the alternation of Prograding Wedges (PWs) and Aggrading Fills (AF) to provide seismo-stratigraphic evidence of relative sea-level changes and estimate the amount of vertical deformation in the Pozzuoli Bay. Five generations of PWs have been documented as associated with distinct periods of relative ground stability separating cyclic alternations of uplift and subsidence.

In the external part NYT caldera, between Miseno and Posillipo offshore, growth of four PWs have been detected since the LGM (Last Glacial Maximum). A first wedge, PW-X1, is observed south of Penta Palummo and Miseno Banks and is related to the LGM lowstand at ~18-18.5 ka. The wedge PW-X2 is observed in the same areas of PW-X1 but in a shallower position and is dated between ~14.9-14.3 ka. A slightly younger wedge, PW-X3 (~12.3-11.9 ka), is well distributed around the main volcanic banks and external continental shelf. Finally, the shallowest wedge recognized in this sector is PW-X4 (~11.2-10.6 ka). This wedge is observed in the offshore sector between Posillipo and Nisida Island, in the northern and north-eastern flank of Penta Palummo and Miseno Banks. The PWs also record a long-term subsidence trend with a rate of 2 mm/a in the external part of the caldera.

Inside the NYT caldera, in the western sector of the Pozzuoli Bay, growth of PW1 (~9.6–9.1 ka) suggests the existence of a previous uplift that affected the peripheral caldera areas in the early stages of the post-collapse activity. Following the stability documented by PW1, the development of AF1 above PW1 underpins subsidence at ~9.1-5.9 ka.

After 5.9 ka, a rapid growth of the resurgent dome in the central part of the caldera occurred, and starting at ~5.2 ka, led to the formation of PW2a. PW2a growth was interrupted at ~4.4 ka by an abrupt uplift episode responsible for the partial erosion of the wedge on the shelf overlying the resurgent dome. A new wedge, PW2b, grew down-stepping below the older wedge until ~3.7 ka. After ~3.7 ka, subsidence caused deposition of AF2 above the wedge, but since ~2.1 ka, it was interrupted by short-term uplift episodes that led to the growth of PW3 (~2.1-1.9 ka), PW4 (~1.4-1.2 ka), and PW5 (~0.6-0.5 ka).

Displacement of coastal infrastructures belonging to the Roman age (~2 ka BP) suggests a short-wavelength vertical deformation signal confined to the Pozzuoli Bay, which reflects the contribution of intra-caldera sources. This local signal is superposed to a long-wavelength regional subsidence increasing between Naples and Procida Island from 1.5 to 2 mm/a, respectively. The east-to-west increasing subsidence reflects the transition between the uplifting Apennines and the Tyrrhenian back-arc basin.

Findings from the current thesis represent a significant advancement towards understanding the evolution of the Campi Flegrei caldera as well as the regional tectonic assessment of this sector of the Campanian Plain. The suitability of high-resolution seismic reflection data to investigate partly submerged collapse calderas may also apply to other partly or totally submerged calderas.

Chapter 1 – Introduction

1.1 Motivation and objectives

Rapid and oscillating ground movements often characterise the post-collapse evolution of calderas and are typically related to the resurgence of a central dome coupled with continued subsidence in the ring fault zone (e.g., Branney and Acocella, 2015).

This thesis focus on the ground deformation of the Campi Flegrei (CF) caldera, situated in the Campanian Plain in southern Italy (Figs. 1.1, 1.2).

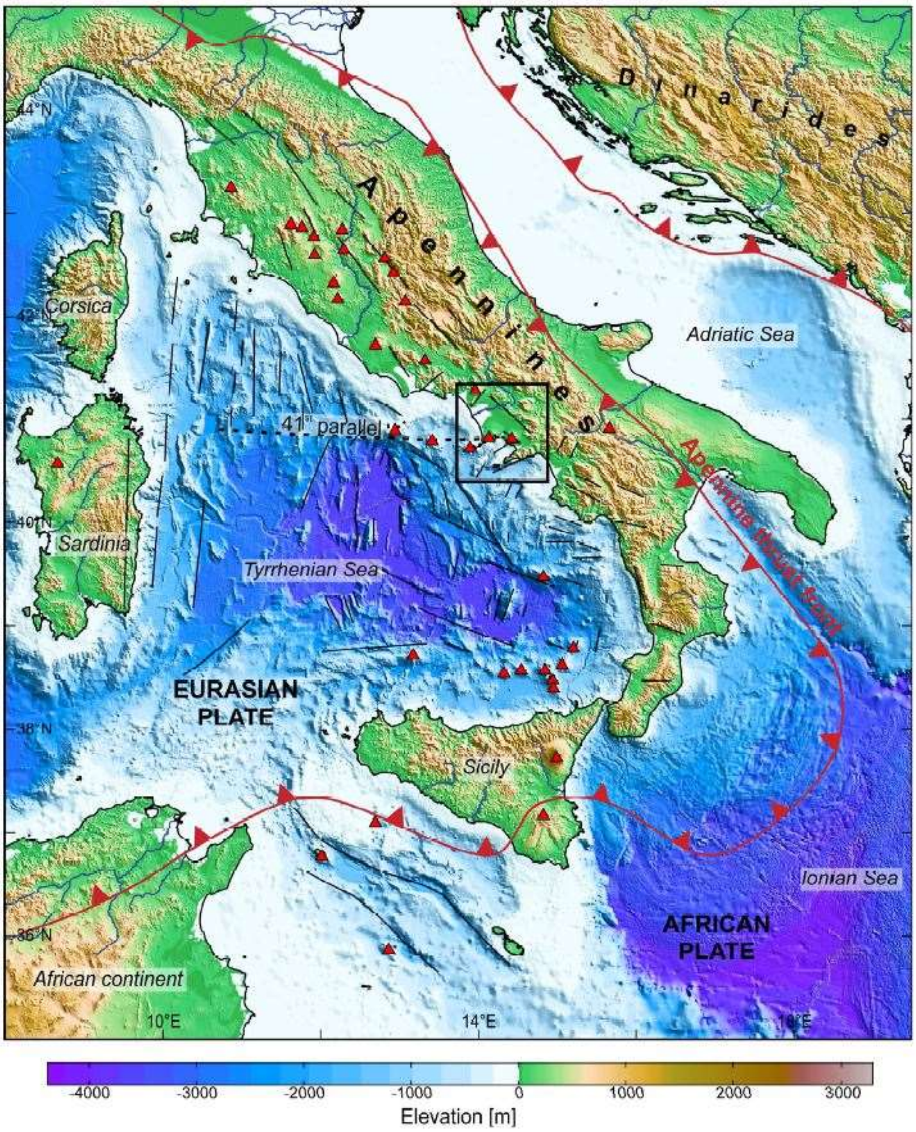

Figure 1.1. Map of the Tyrrhenian Sea and southern Italy with the African-Eurasian subduction zone indicated in dark red (from Malinverno and Ryan, 1986). Red triangles mark major Italian volcanoes. Black solid lines indicate normal faults. The black square indicates the location of the Campanian Margin.

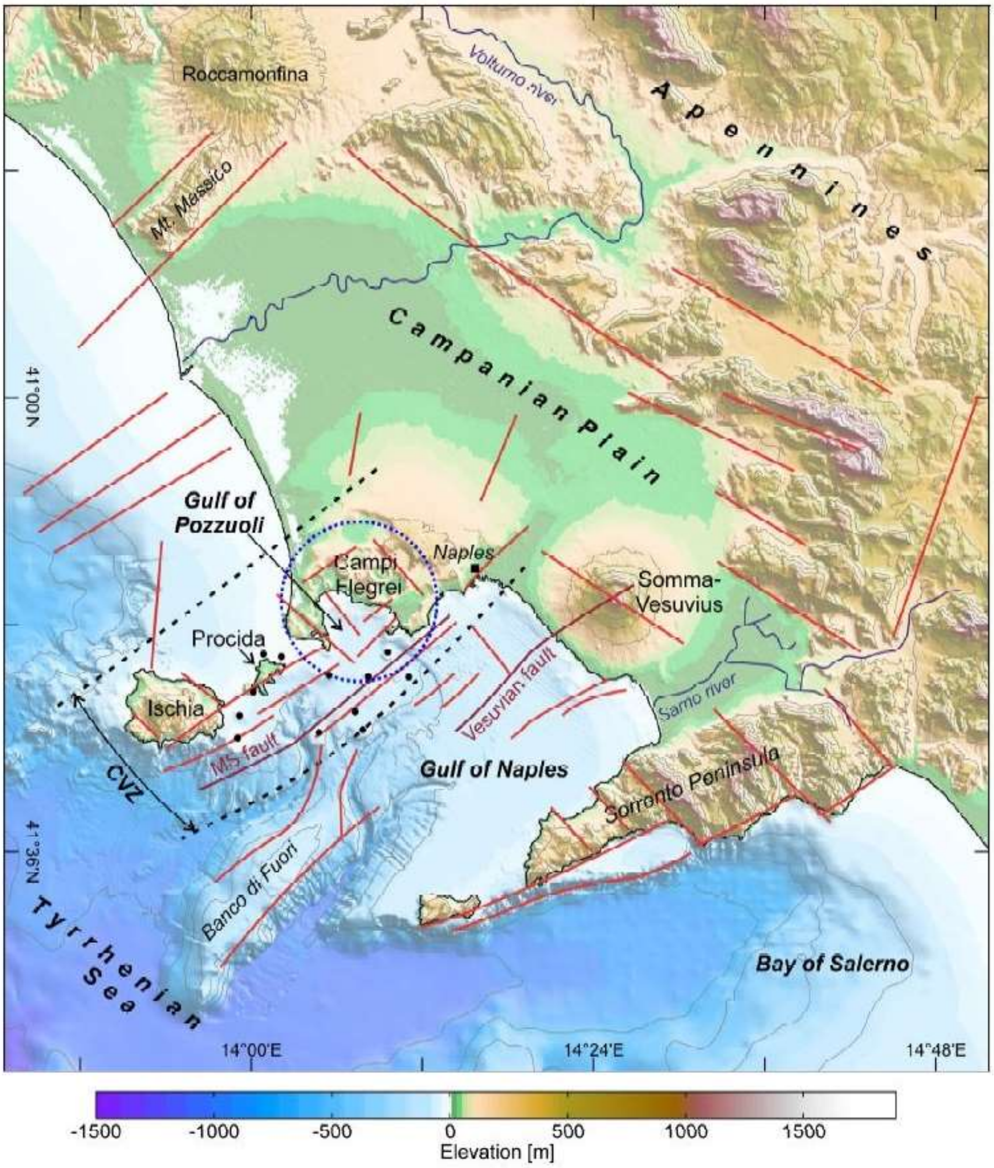

Figure 1.2. Map of the Campania continental margin, southern Italy (Becker et al., 2009). Bathymetry from D'Argenio et al. (2004). Red lines indicate major normal faults from Bruno et al. (2003).

Because of their exceptionally rich geological, historical, and current records of deformation, the ground movements in the Campi Flegrei caldera have been reconstructed with unpaired detail at both historical (Lyell, 1830; Parascandola et al., 1947; Bellucci et al., 2006; Mohrange et al., 2006) and Holocene (Marturano et al., 2018; Isaia et al., 2019) time-scales. Despite this wealth of observations, a comprehensive appraisal of post-caldera collapse deformation suffers the limitation that over one-third of the caldera lies beneath the Pozzuoli Bay (Fig. 1.3).

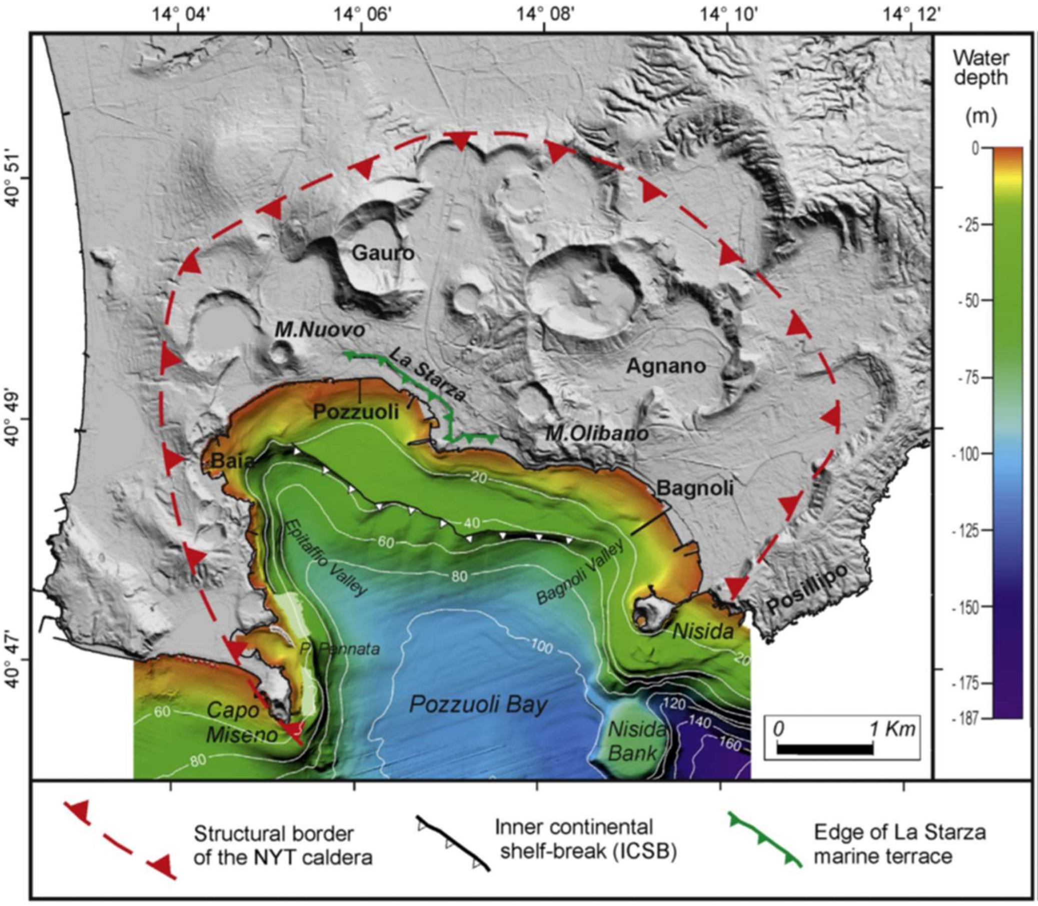

Figure 1.3. Digital elevation model (DTM) of the Campi Flegrei (from Sacchi et al., 2014).

Recurrent collapses of the central part of the CF caldera is associated with the large-magnitude eruptions of the Campanian Ignimbrite (CI) at ~39 ka (Scarpati et al., 2020) and of the Neapolitan Yellow Tuff (NYT) at ~15 ka (Orsi et al., 1992; Deino et al., 2004). The latter collapse after the NYT eruption was followed by discrete phases of intra-caldera volcanic activity (Di Vito et al., 1999) and by the resurgence of a central dome, characterised by alternations of uplift and subsidence displacements. In the onshore part, the NYT collapsed caldera corresponds to the external morphological border, which includes the CF intra-caldera vents (Fig. 1.3).

Recent onshore studies documented that ground movements at Campi Flegrei, interfering with sea-level variations, caused significant perturbations of the stratal architecture and stacking pattern of the caldera basin fill (Marturano et al., 2018; Isaia et al., 2019). These reconstructions rely on the analysis of marine-transitional sediments that are uplifted above sea-level (La Starza terrace, Figs. 1.3, 1.4) or, for historical times, on archaeological markers along the coast (Di Vito et al., 2016). Seismic profiles interpretation documented that the offshore part of the caldera also recorded similar vertical deformations (Sacchi et al., 2014; Steinmann et al., 2018; Natale et al., 2020, 2021).

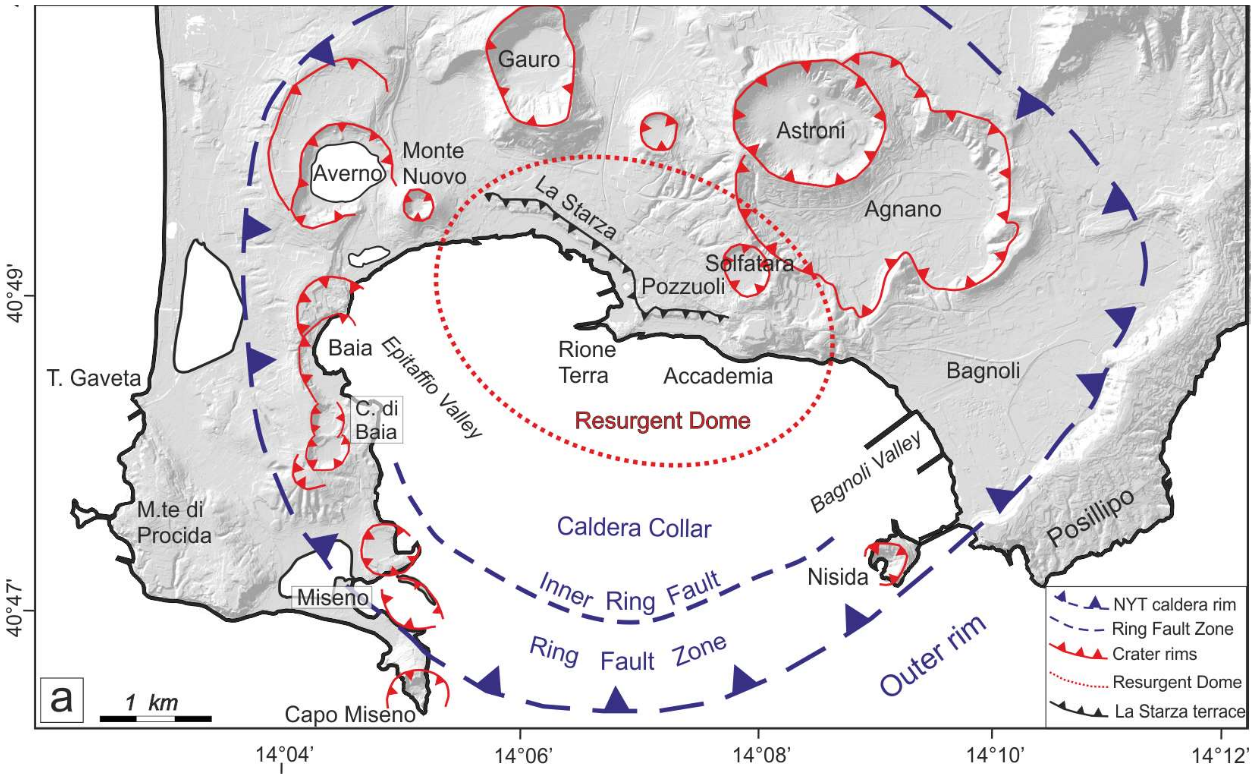

Figure 1.4. Morpho-structural map of the Campi Flegrei illustrating the main structural elements of the caldera associated with the Neapolitan Yellow Tuff (NYT) eruption and post-NYT intra calderic volcanic vents (modified after Sacchi et al., 2014 and Steinmann et al., 2018).

This thesis aims to accurately reconstruct long- to short-term deformations offshore the CF caldera by integrating high-resolution seismic profiles interpretation and analysis of coastal archaeological data. Reconstruction of the stacking pattern of depositional sequences and identification of markers related to ancient wave-base levels in seismic profiles have provided quantitative displacement estimations for the last ~18 ka. Archaeological sea-level indicators of the Roman age, which are nowadays submerged down to a few meters, supplement deformation data for the last ~2 ka BP.

For historical times, the multi-dataset analysis has allowed disentangling the effects of the post-caldera dynamics from a broader deformation signal that affects this part of the extensional margin of the Apennines. A comprehensive reconstruction of past ground deformations in the offshore part of the CF caldera contributes to understanding the past and current evolution of the caldera, which nowadays represents one of the world's highest volcanic risk areas (Charlton et al., 2020).

1.2 Calderas architecture and evolution

Caldera eruptions are among the most catastrophic natural events affecting Earth's surface and society. They have attracted particular attention in scientific communities and governmental institutions worldwide. Understanding caldera-forming mechanisms and dynamics is paramount to reliably assessing volcanic hazards and risks of future eruptions. Traditionally, calderas have been analysed based on geological field studies and borehole observations, which mainly allowed for selective and spatially limited information on complex caldera systems. More recently, analogue geophysical modelling has provided additional insights into the formation and development of calderas. In submerged caldera settings, marine seismic imaging has emerged as a powerful tool for understanding the stratigraphic architectures and structures.

In general, calderas are sub-circular topographic depressions originating from the collapse or subsidence of the top of a partly drained magma chamber during or immediately after an explosive volcanic eruption. A simplified "end-member" classification of collapse calderas is represented in Figure 1.5 (Cole et al., 2005) was established to allow for a systematic understanding of caldera subsidence geometries. The subsidence may vary, ranging from a few meters to a few kilometres depending on the style and geometry of collapse (Acocella, 2007).

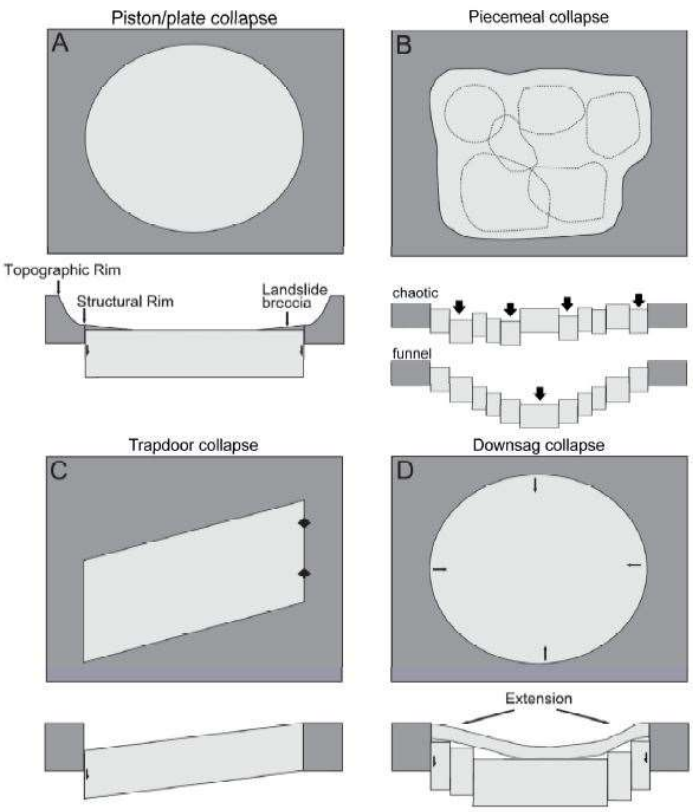

Figure 1.5. Caldera end-member models illustrating alternative subsidence geometries (modified from Cole et al., 2005).

The shape and size of caldera depressions vary and are closely linked to the tectonic setting and the geometry of the underlying magma chamber. Pre-existing structural faults may act as pathways for the ascent of magma from a deeper reservoir, thereby controlling eruptive fissures. A caldera is formed by more than one eruption, called a nested caldera complex. The intra-caldera region is separated from the extra-caldera region by a complex margin. The marginal area is characterized by intense deformation, often accompanied by a ring fracture zone, hydrothermal alteration, magmatic intrusions, and topographical instability (Branney and Acocella, 2015).

A simplified sketch illustrating a caldera-forming eruption in five stages is represented in Figure 1.6. Before a caldera-forming eruption, tumescence (i.e. uplift due to an inflation of the magma chamber) and small-scale eruptions commonly occur (Aizawa et al., 2006). Consequently, the magma chamber is quickly emptied, resulting in under-pressure. In the post-collapse phase, calderas are typically associated with short-term episodes of unrest and eruptions. Furthermore, many calderas are characterized by post-collapse resurgence (i.e., renewed inflation of the magma chamber), resulting in long-term uplift of the intra-caldera area (Smith and Bailey, 1968). The architecture of the resurgent dome depends on the aspect ratio (thickness/width) of the magma chamber roof (Acocella et al., 2007). Aspect ratios of ~1 favour the development of a resurgent block, as occurred on Ischia Island (Acocella and Funiciello, 1999), while aspect ratios of ~ 0.4 are associated with the formation of a resurgent dome as observed at the CF caldera (Acocella et al., 2001). Besides the widely accepted concept that large-scale caldera-forming eruptions severely affect the global climate, it has also been suggested that climatic changes such as sea-level and ice-load variations may initiate explosive volcanic eruptions (Albino et al., 2010).

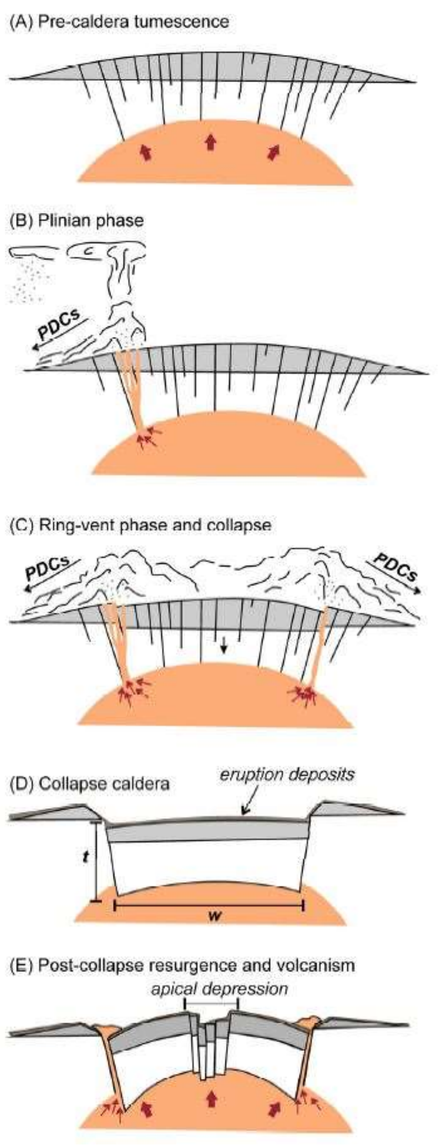

Figure 1.6. Simplified sketch illustrating a caldera-forming eruption in five stages (from Smith and Bailey, 1968).

1.3 Volcanism associated with the extensional tectonism of the Campanian Margin

Volcanism in the Campanian Plain started at about 0.5 Ma in the northernmost area at the currently extinct Roccamonfina volcano and migrated further SE to the Neapolitan area (Fig. 1.2) during Plio-Pleistocene times (Crosweller et al., 2012). Except for Procida Island, all volcanic centres (i.e. Somma-Vesuvius, Ischia Island, Campi Flegrei, Fig. 1.2) show clear evidence of recent activity as indicated by ongoing earthquakes or fumarolic activity (Paoletti et al., 2013).

The Plio-Quaternary volcanism along the Campania margin is strongly controlled by NE-SW and NW-SE trending structural faults (Fig. 1.2) that developed in the course of back-arc extensional tectonism (Bruno et al., 2003).

The eastern margin of the Tyrrhenian Sea is characterised by several basins that evolved during the latest Neogene-Quaternary across the structural boundary between the Apennine fold and thrust belt and the Tyrrhenian back-arc extensional area (Malinverno and Ryan, 1986; Lavecchia, 1988; Doglioni et al., 1991) (Fig. 1.1). These basins, which include the Campanian Plain, formed in response to orogen-parallel extension and associated transtensional tectonics that accompanied the anti-clockwise rotation of the Apennine belt and lithospheric stretching in the central Tyrrhenian basin (Patacca and Scandone, 1990; Scandone et al., 1991; Ferranti et al., 1996). The peri-Tyrrhenian basins developed within the overall context of back-arc extensional tectonism related to retreating subduction within the Africa–European convergence zone. The Campanian Plain is bounded to the east by the Apennines and the west by the Tyrrhenian Sea(Fig. 1.1). The morphology of the Campanian Margin has primarily been affected by Plio-Quaternary NW-SE and NE-SW trending normal faults displacing the Mesozoic carbonate basement (Fig. 1.2).

The Gulf of Naples is located in the southern part of the Campanian Plain. Along the Plain border, NE–SW trending normal faults controlled the development of the Quaternary basins. The area SE of the Magnaghi-Sebeto (MS) fault with the Somma-Vesuvius is mainly characterized by NE-SW trending fractures. In contrast, the sector NW of the MS fault, including the CF caldera, shows a more complex fault pattern with both NE-SW and NW-SE trending faults (Bruno et al., 2003) (Fig. 1.2). Pleistocene-to-Holocene volcanic activity in the northern part of the Gulf of Naples is distributed amongst the Somma-Vesuvius stratovolcano, the volcanic fields of Campi Flegrei, and Ischia and Procida Islands.

1.4 Volcanic districts

Somma-Vesuvius

The formation of Mt. Somma was mainly related to effusive volcanism (i.e. the generation of lava flows) (Fig. 1.2). The oldest lava flows were dated at ~0.4 and 0.3 Ma. Between 0.3 Ma and the CI eruption at 39 ka, the Vesuvian area was characterized by volcanic quiescence (Brocchini et al., 2001). Between 39 and 20 ka, the period was mainly marked by effusive activity at Mt. Somma. At ~18 ka, the effusive volcanism changed into explosive activity with the large Pomici di Base eruption leading to the first caldera formation at Mt. Somma. Afterwards, at least three additional caldera-forming events related to Plinian eruptions occurred at Mt. Somma, with the Mercato Pumice eruption at 8 ka, the Avellino eruption at 3.9 ka, and the Pompeii eruption at CE 79 (Santacroce et al., 2003; Cioni et al., 2008). The Vesuvius cone grew after the CE 79 eruption, characterized by effusive and explosive eruptions and a minor summit caldera collapse. The last eruption took place in 1944, associated with relatively mild explosive volcanism (Cioni et al., 2008).

Ischia and Procida Islands

Ischia Island's onset of volcanic activity is still not precisely known (Fig. 1.2). The oldest dated volcanic deposits revealed an age of ~150 ka. However, these dated outcrops are underlain by older (not yet dated) volcanic remnants of a complex volcanic edifice, probably formed by older explosive eruptions (Santacroce et al., 2003). The Ischia volcanic activity can be grouped into four phases: (1) >150 ka; (2) 150-33 ka, (3) 28-18 ka and (4) 10 ka–CE 1302 (with minor volcanic quiescence between 4.3 and 2.9 ka) (Civetta et al., 1991; Brown et al., 2008; Paoletti et al., 2013). The Ischia caldera was formed at ~55 ka during the Mount Epomeo Green Tuff eruption. In the post-caldera phase, between 55 and 33 ka, further major ignimbrites were emplaced (e.g. Citara Tuff). The western-central part of the Ischia caldera has been uplifted by ~900 m due to blocking resurgence, initiated between 33 and 28 ka (Tibaldi and Vezzoli, 1998; Santacroce et al., 2003). Procida Island hosts five monogenetic volcanoes (Vivara, Terra Murata, Pozzo Vecchio, Fiumicello and Solchiaro), active between 70 and 14 ka producing pyroclastic deposits and one lava dome (De Astis et al., 2004).

Campi Flegrei

Volcanism in the Campi Flegrei area started before ~80 ka. It was characterised by mainly explosive monogenetic activity, with few associated lava domes and caldera-forming eruptions such as the Campanian Ignimbrite (CI) and Neapolitan Yellow Tuff (NYT) eruptions (Rosi and Sbrana, 1987).

The last significant eruption, which emplaced the NYT, a 40 km^3 (DRE) ignimbrite (e.g., Scarpati et al., 1993), occurred at ~15 ka (Deino et al., 2004) and resulted in a large caldera collapse (Orsi et al., 1992). The NYT caldera involves a quasi-circular area of ~10 km diameter that extends from onland to the Pozzuoli Bay (Fig. 1.3; Sacchi et al., 2014; Steinmann et al., 2018).

Following the caldera collapse, several intra-caldera eruptions occurred during discrete periods between 14.9-10.6 ka (Epoch 1), 9.6-9.1 ka (Epoch 2), and 5.5-3.5 ka (Epoch 3) (Di Vito et al., 1999; Smith et al., 2011; Bevilacqua et al., 2016). Epoch 3 is further subdivided in Epochs 3a (5.5-4.55 ka) and 3b (4.44-3.7 ka) based on the existence of a brief repose period between two major phases of volcanic unrest (Isaia et al., 2009; Smith et al., 2011; Isaia et al., 2019). The resurgence-related uplift caused the emersion of mixed marine-volcaniclastic deposits, which are exposed up to 30 m above sea-level in the central part of the dome where they form the La Starza terraced sedimentary unit (Fig. 1.3; Di Vito et al., 1999; Isaia et al., 2019). The net displacement of the La Starza deposits occurred through alternating phases of uplift and subsidence, with major uplifts temporally coupled to epochs of volcanic activity (e.g., Isaia et al., 2019).

Historical ground movements since Roman times are documented by displacement of archaeological remains (e.g., Bellucci et al., 2006; Mohrange et al., 2006). The last eruption in the CF caldera occurred in 1538 CE at Monte Nuovo, venting west of Pozzuoli town (Fig. 1.3) after ~200-400 years of ground uplift and felt seismicity (Guidoboni and Ciuccarelli, 2011). In the last century, three episodes of major unrest in 1950-52, 1969–72, and 1982–84 caused notable uplift of the Rione Terra quarter in Pozzuoli (Fig. 1.3). However, they were not followed by eruptions. The last uplift phase began in 2005 and is still ongoing, with marked geodetic, seismic, and geochemical evidence of unrest since 2012 (e.g., Del Gaudio et al., 2010; Chiodini et al., 2016; Ricco et al., 2019).

1.5 Existing data records of ground movements in the Campi Flegrei

Recent research at Campi Flegrei has documented that the NYT caldera resurgence and associated ground deformation interfered with sea level changes. This interference caused a significant deviation of the stratal architecture from the standard sequence stratigraphic models developed for non-volcanic depositional systems (Sacchi et al., 2014; Marturano et al., 2018; Steinmann et al., 2018; Isaia et al., 2019).

Studies of the uplifted La Starza terrace (Figs. 1.3, 1.4) documented that the ground movements at Campi Flegrei caldera and coeval sea level variations caused sharp vertical and lateral changes in the stratal architecture indicative of abrupt changes in sedimentation depth (Di Vito et al., 2016; Marturano et al., 2018; Isaia et al., 2019). Analogously, the offshore part of the caldera is affected by the stacking of different seismic facies in the post-15 ka fill indicative of post-collapse deformation (Sacchi et al., 2014).

The analysis of the La Starza succession indicates that, in the last 15 ka, the proximal sector of the bay was characterized by alternating marine and subaerial environments (Isaia et al., 2019).

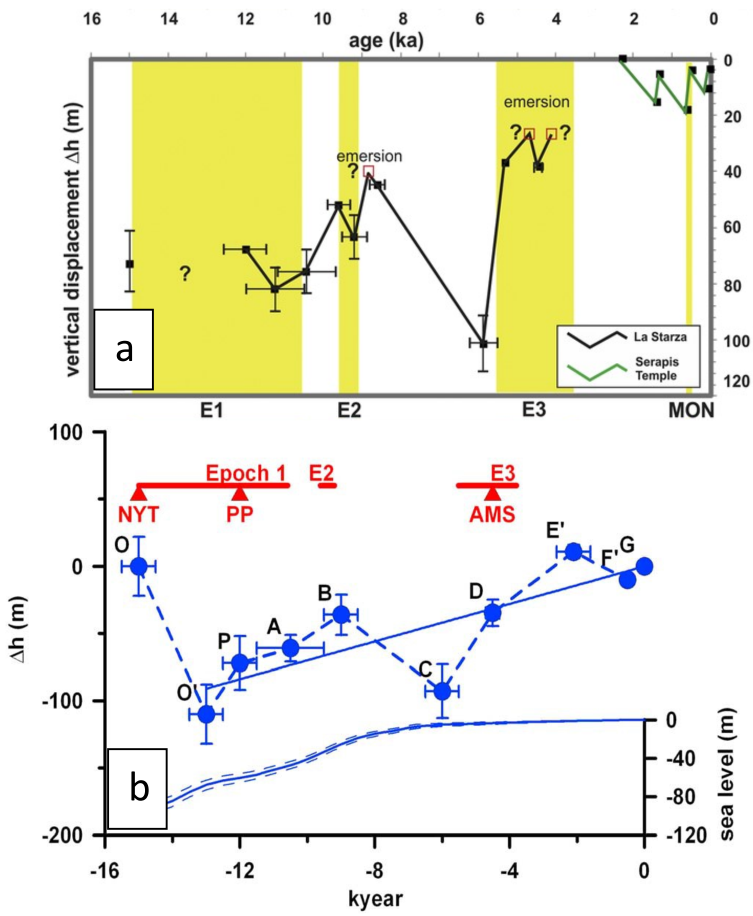

Figure 1.7. Vertical Ground displacement at the La Starza marine terrace over the last 15 ka. a) from Isaia et al. (2019). b) from Marturano et al. (2018).

The displacement of the La Starza unit deposits, which are nowadays exposed up to ~55 m above sea level, occurred through alternating phases of uplift and subsidence and resulted in a net uplift (Marturano et al., 2018; Isaia et al., 2019) (Fig. 1.7).

Periods of eruptive activity E1 (15–10.6 ka), E2 (9.6–9.1 ka) and E3 (5.5–3.8 ka) appear coupled with prevalent uplift and possible minor deflating episodes. On the contrary, the whole caldera floor subsidence occurred during quiescent periods, from 8.59 to 5.86 ka, generally after 3.8 ka and before the Monte Nuovo eruption (Isaia et al., 2019). A rapid ground uplift of ~100 m occurred between the 5.5–3.5 ka volcanic activity (Isaia et al., 2019).

Thanks to its exceptionally rich historical and current record of deformation, including displacement of archaeological markers (Lyell, 1830; Parascandola et al., 1947; Bellucci et al., 2006; Mohrange et al., 2006; Aucelli et al., 2021), the onshore historical ground movements in the CF caldera have been reconstructed with unpaired detail. Bellucci et al. (2006) suggest the occurrence of three episodes of coupled subsidence and uplift: (1) subsidence from the second century CE to about 500-600 CE, followed by uplift until about 700-900 CE; (2) subsidence from 700-900 CE until about 1430, followed by uplift until 1538; and (3) subsidence from 1538 until 1969, followed by net uplift between 1969 and 2005 (Fig. 1.8).

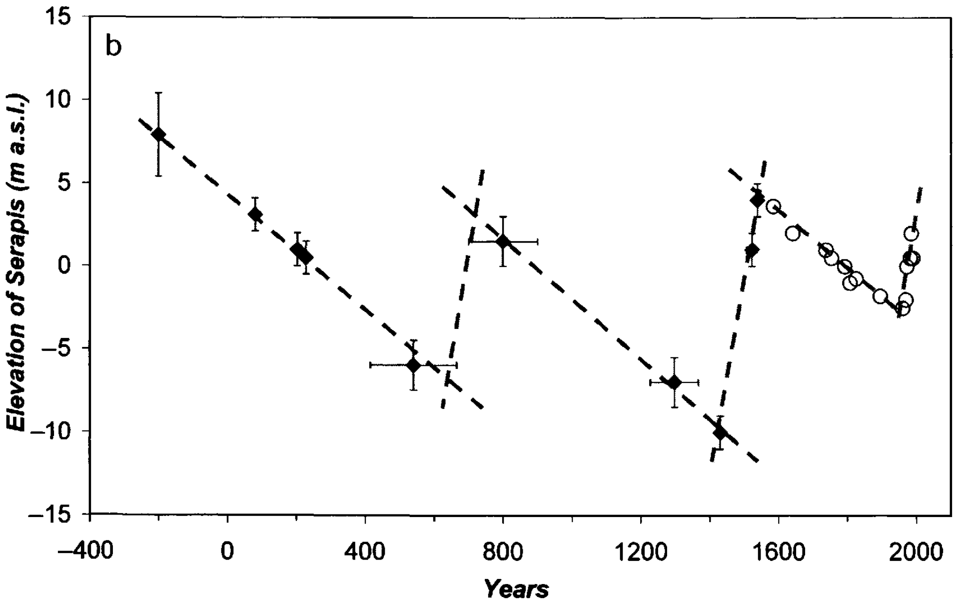

Figure 1.8. Vertical ground movements derived from Serapeum (from Bellucci et al., 2006).

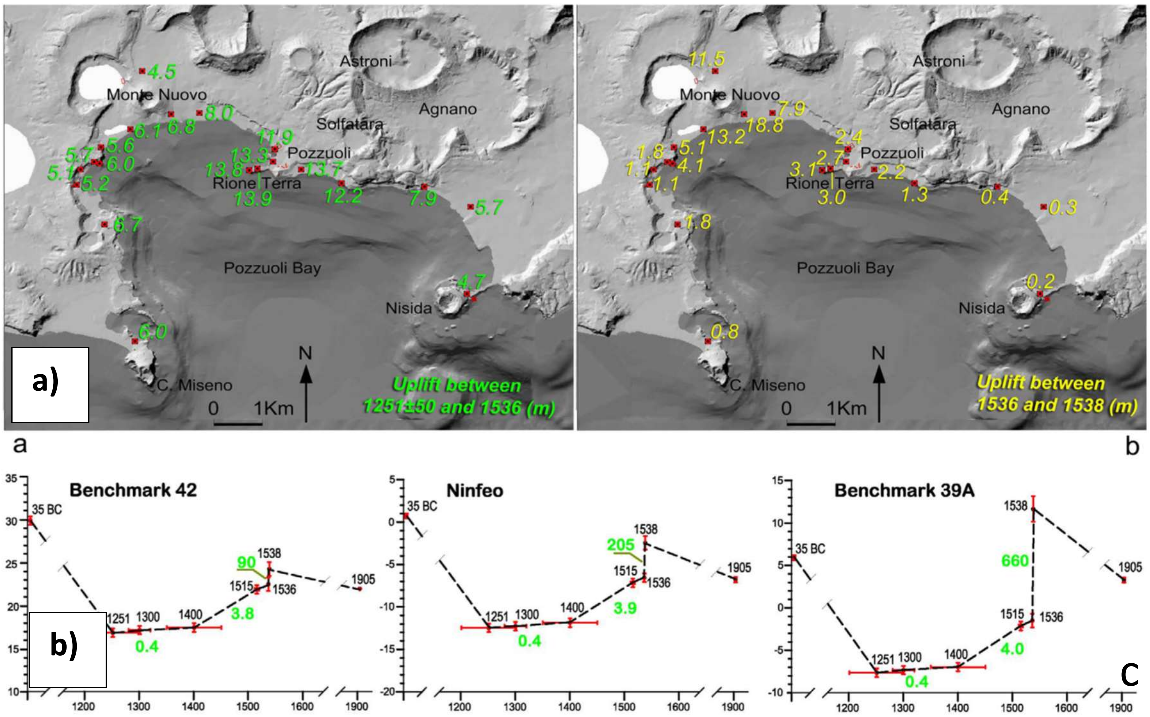

Figure 1.9. a) Distribution of the uplift preceding the Mt. Nuovo eruption. From 1251 to 1536 (a), the uplift affects the caldera, with a maximum in the Pozzuoli area. From 1536 to 1538 (b), the uplift is centred in the area of the future eruption (Monte Nuovo). **b)** Reconstruction of the elevation in the last 100 years at 3 selected sites within the Campi Flegrei caldera, obtained integrating geological, historical and archaeological data (from Di Vito et al., 2014).

The magnitude of these deformations events is about 7-10 m of uplift during about 200 years and 7-10 m as well of subsidence during about 600-800 years (Bellucci et al., 2006). The last eruption in the CF (Monte Nuovo eruption) in 1538 CE occurred after ~200 years of ground uplift (Di Vito et al., 2014). Di Vito et al. (2014) shows that between 1251 CE, but effectively from 1251 CE and 1536 CE, a general cumulative uplift affected the inner caldera, with a maximum value of 14 m in Pozzuoli (Fig. 1.9). The largest part of this deformation occurred between 1400 and 1536, with a maximum of about 12 m in Pozzuoli. The deformation from 1536 to 1538 is centred on the area of the future eruption, with a maximum uplift of ~19 m.

In the last century, three episodes of major unrest occurred in April 1950–May 1952, July 1969–July 1972 and June 1982–December 1984, accompanied by several earthquakes, causing an intense ground uplift of the central district of Rione Terra, however, they did not follow by eruptions. A maximum uplift has been estimated between 1950 and 1985 of 3.8±0.20 m, and about 1 m has been lost between 1985 and 2004 (Del Gaudio et al., 2010). A new ground uplift began starting from 2005. This uplift has different characteristics. The rate of deformation since 2005 is about 20 times slower than the 1969–1972 and 1982–1984 episodes. The last uplift phase began in 2012 and is still ongoing (Fig. 1.10) (Ricco et al., 2019).

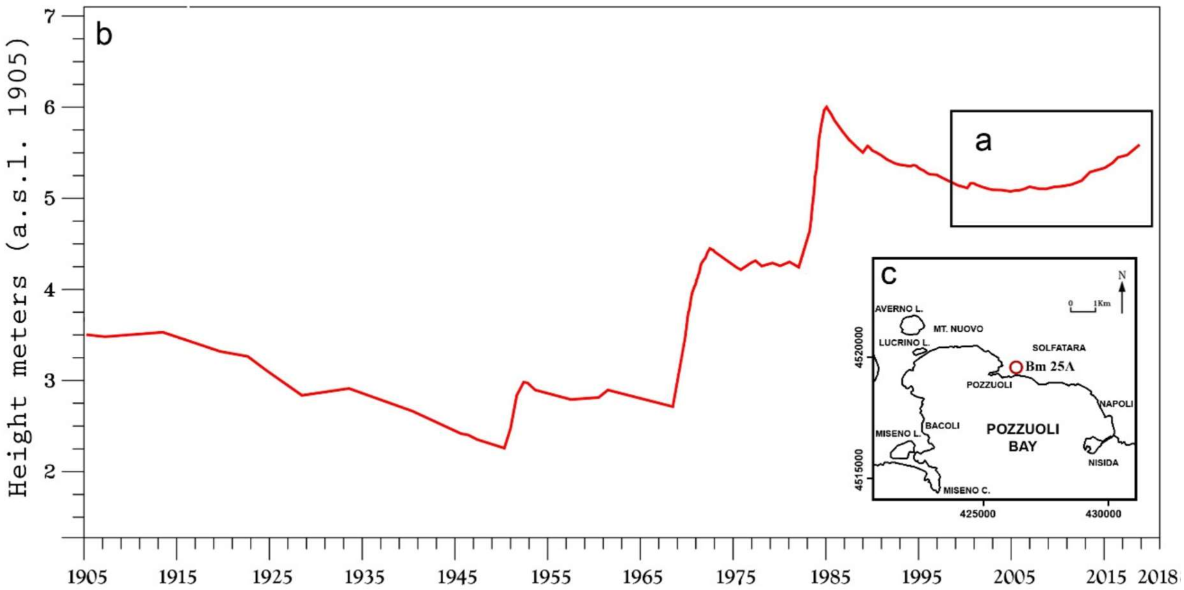

Figure 1.10. Height variations measured at benchmark 25A (inset) between 1905 and 2018 (from Ricco et al., 2019).

1.6 Background setting of the offshore Campi Flegrei caldera

Multi-scale seismic profiles analysis in the Pozzuoli Bay has provided an updated chronostratigraphic frame for the post-NYT caldera fill, represented by volcaniclastic material produced by CF eruptions interbedded with marine sediments (Sacchi et al., 2014, Steinmann et al., 2018). Previous literature on volcaniclastic sediments has greatly improved how sedimentary processes respond to volcanic activity (Fisher et al., 1991). However, shallow marine volcaniclastic systems developed and evolved within large collapse calderas in coastal areas are still poorly understood. Studies in the CF caldera documented that the coastal sedimentary fill is often accompanied by large volumes of volcaniclastic materials deposited in relatively short time intervals (Sacchi et al., 2014).

The Pozzuoli Bay represents a minor inlet of the Gulf of Naples and is characterized by a central depression with a maximum water depth of about 110 m b.s.l. The Bay of Pozzuoli is characterized by a shelf morphology (Fig. 1.3) with different terrace surfaces related to the ground movements of the caldera floor coupled with sea level variations and erosional processes (Sacchi et al., 2014).

The Pozzuoli Bay overlies over one-third of the southern part of the caldera and includes almost concentric morpho-bathymetric and structural belts (Fig. 1.4). The offshore CF caldera features an outer zone external to the morpho-structural rim, representing the remains of the NYT and older caldera collapses (Vitale and Isaia, 2014; Steinmann et al., 2018). The inner part of the rim corresponds to the ring fault zone, a locus of vigorous degassing, which is limited inward by a system of normal faults associated with the NYT caldera collapse (inner ring fault; Steinmann et al., 2018). The inner ring fault separates the ring fault zone from the caldera collar, which reaches the deepest water depths (down to -120 m) in the bay and overlies the depocenter area of the basin fill (Sacchi et al., 2014; Natale et al., 2021) (Fig. 1.4). The shallower sector of the Pozzuoli Bay forms the inner continental shelf and overlies part of the resurgent dome broadly centred at Pozzuoli town (Fig. 1.3).

Marine sediments interbedded with volcaniclastic material produced by CF eruptions and deposited in relatively short time intervals (Sacchi et al., 2014, Natale et al., 2020; 2021) represent the caldera fill. Seismic interpretation, calibrated with gravity core stratigraphy, was used to describe the main seismic stratigraphic units and understand the offshore stratal geometries and structures (Sacchi et al., 2014). Tephra layers interbedded within the cored sequence have been characterized, and absolute ages were obtained from tephrochronological analysis and AMS ^{14}C dating (Sacchi et al., 2014). Stratigraphic calibration of seismic records was provided by the detailed analysis of three gravity cores (C1062, C23 and C32) with a length of 5-6 m, collected in the Pozzuoli Bay at a water depth of ~90 to 103 m (Fig. 1.11). In this thesis, these three gravity cores have been used to calibrate the shallowest part of the caldera infill down to the 3.9 ka tephra dated in the gravity core.

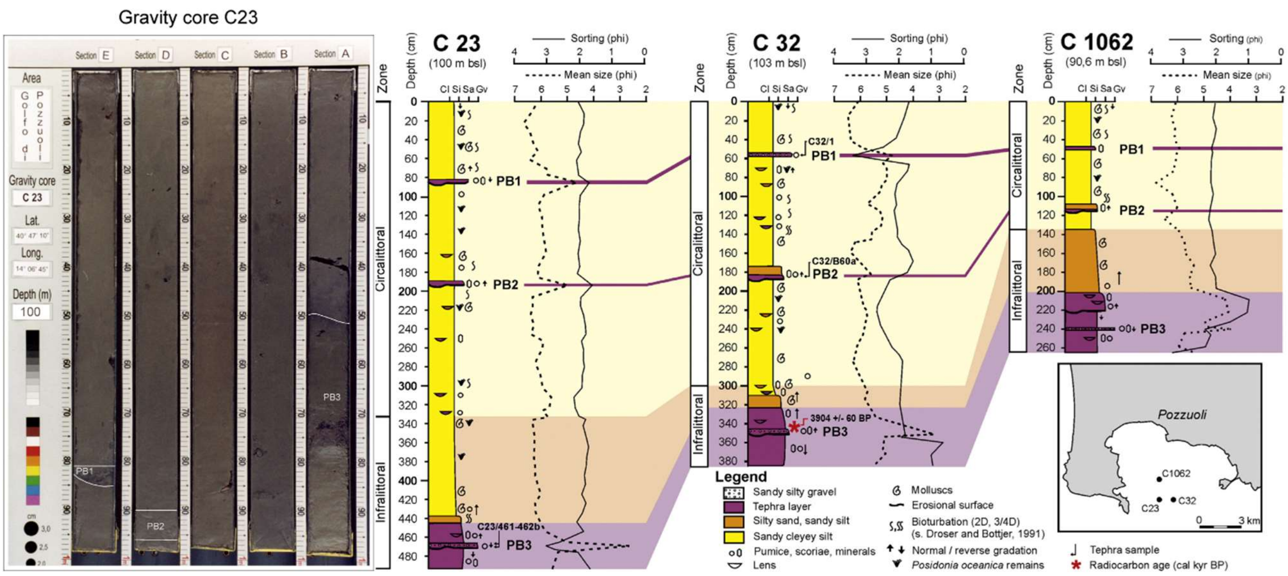

Figure 1.11. Photograph of C23 core. b) Stratigraphic correlation of gravity cores C23, C32 and C1062 and correlation with cryptotephra PB1, PB2 and PB3 within the Pozzuoli Bay (from Sacchi et al., 2014).

Steinmann et al. (2016) investigated the interplay between volcano-tectonic processes and sea-level variations in the offshore sector of the CF caldera since ~39 ka based on multichannel seismic datasets. Their reconstruction suggests two separate caldera collapses related to the CI eruption at ~39 ka and the NYT eruption at ~15 ka, outlining the existence of a nested-caldera system. Based on the E-W oriented multichannel seismic profile GeoB08–065, a 7-stage model for the CF caldera formation and evolution in interplay with sea-level variations since 39 ka is shown in Figure 1.12.

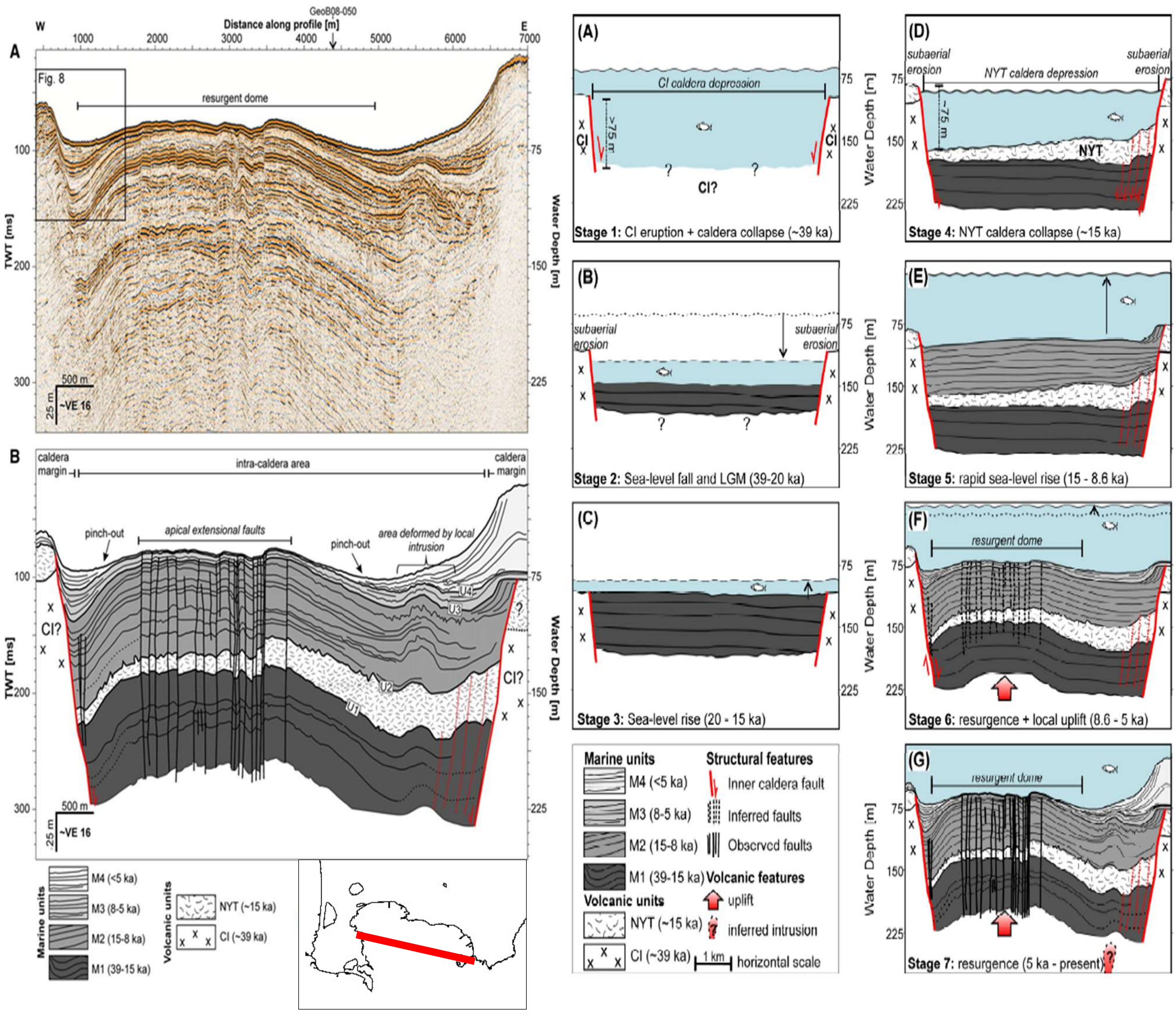

Figure 1.12. a) Reconstruction of the caldera formation and evolution since ~39 ka based on GeoB08-065. The model shows the caldera formation in the course of the CI and NYT eruption and subsequent deformation and deposition in interplay with sea-level variations (from Steinmann et al., 2016).

Sacchi et al. (2014) have summarized the post-15 ka CF caldera evolution in four stages that provide a semi-quantitative reconstruction of vertical movements following the NYT eruption (Fig. 1.13). After 15.0 ka, the NYT eruption was followed by caldera collapse along with the ring fault system. The collapsed structure hosted ~60 m of volcaniclastic and epiclastic sediments that accumulated at high depositional rates during a relatively short period (Fig. 1.13).

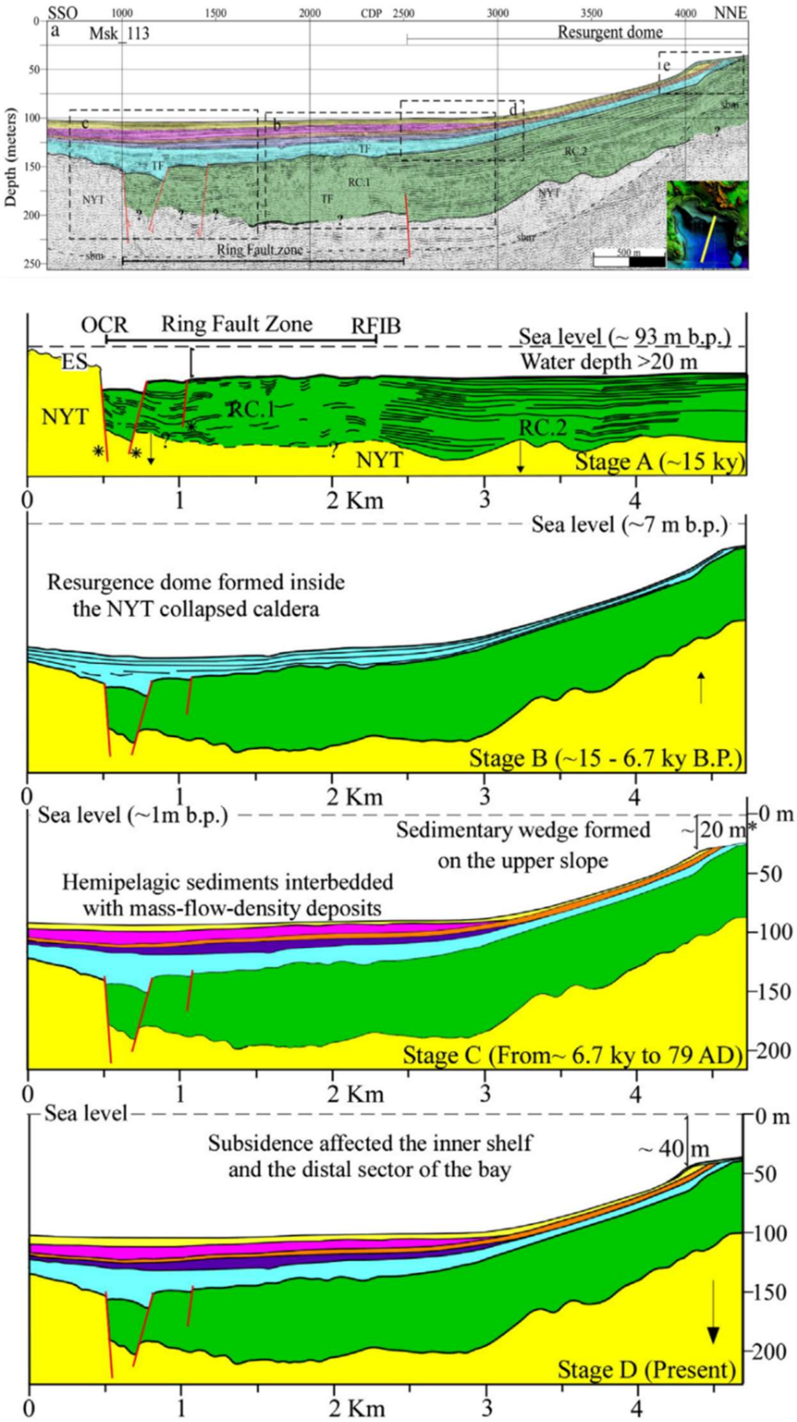

Figure 1.13. a) Depth-converted Msk_113 Sparker seismic profile and stages of evolution of the NYT caldera: a) 15.0 ka BP; b) 15.0–6.6 ka BP; c) 6.6–2.0 ka BP; d) 2.0 ka BP–Present (from Sacchi et al., 2014).

Between 15.0 and 6.7 ka, an inner caldera resurgent dome started to form in the northern sector of the future Pozzuoli Bay (Fig. 1.13). The period between 6.7 and 2.0 ka is characterized by the deposition of gravity flow units interbedded with circalittoral deposits in the deepest sector of the bay. An infralittoral prograding wedge started to form towards the inner continental shelf of the Pozzuoli Bay, at a water depth of ~20 m b.s.l. The varying thickness of the upper part of the sedimentary succession suggests that vertical movements (uplift/subsidence) with different magnitudes possibly occurred in the area during this time interval (Fig. 1.13). After ~2 ka BP, a subsidence phase has been detected offshore, in agreement with documented archaeological evidence of ground subsidence between the Roman period and the Middle Ages in the area of Pozzuoli (Fig. 1.13).

1.7 Seismo-stratigraphy in the Pozzuoli Bay

Based on the interpretation of high-resolution seismic profiles (part of the same dataset analysed here), Natale et al. (2020; 2021) distinguished seismic facies indicative of volcaniclastic-poor and volcaniclastic-rich marine sediments.

The correlation of seismic units with the coeval La Starza succession exposed on-land performed by Natale et al. (2020, 2021) has been used to date the seismo-stratigraphical and morpho-depositional features analysed in this thesis.

The first 6 m of the seismo-stratigraphic interval were calibrated using three gravity cores that contained tephra assigned to the ∼3.9 ka Capo Miseno eruption (T1), Pompei 79 CE Vesuvius tephras (T2), and 1538 CE Monte Nuovo eruption (T3) (Figs. 1.14, 1.15. 1.16) (Sacchi et al., 2014). Projection of the cored intervals on the seismic profiles indicates that these horizons correspond to high-amplitude, high-frequency continuous reflections (Natale et al., 2020). By inference, deeper reflections with similar attributes were assigned by Natale et al. (2021) to products of older eruptions, whose age is retrieved by calibrating unit-bounding unconformities with their dated continental counterparts exposed at La Starza (Isaia et al., 2019). The high-amplitude reflections are intercalated within semi-transparent to sub-chaotic seismic reflections. This seismic facies corresponds to prevailing marine deposits with minor volcaniclastic input.

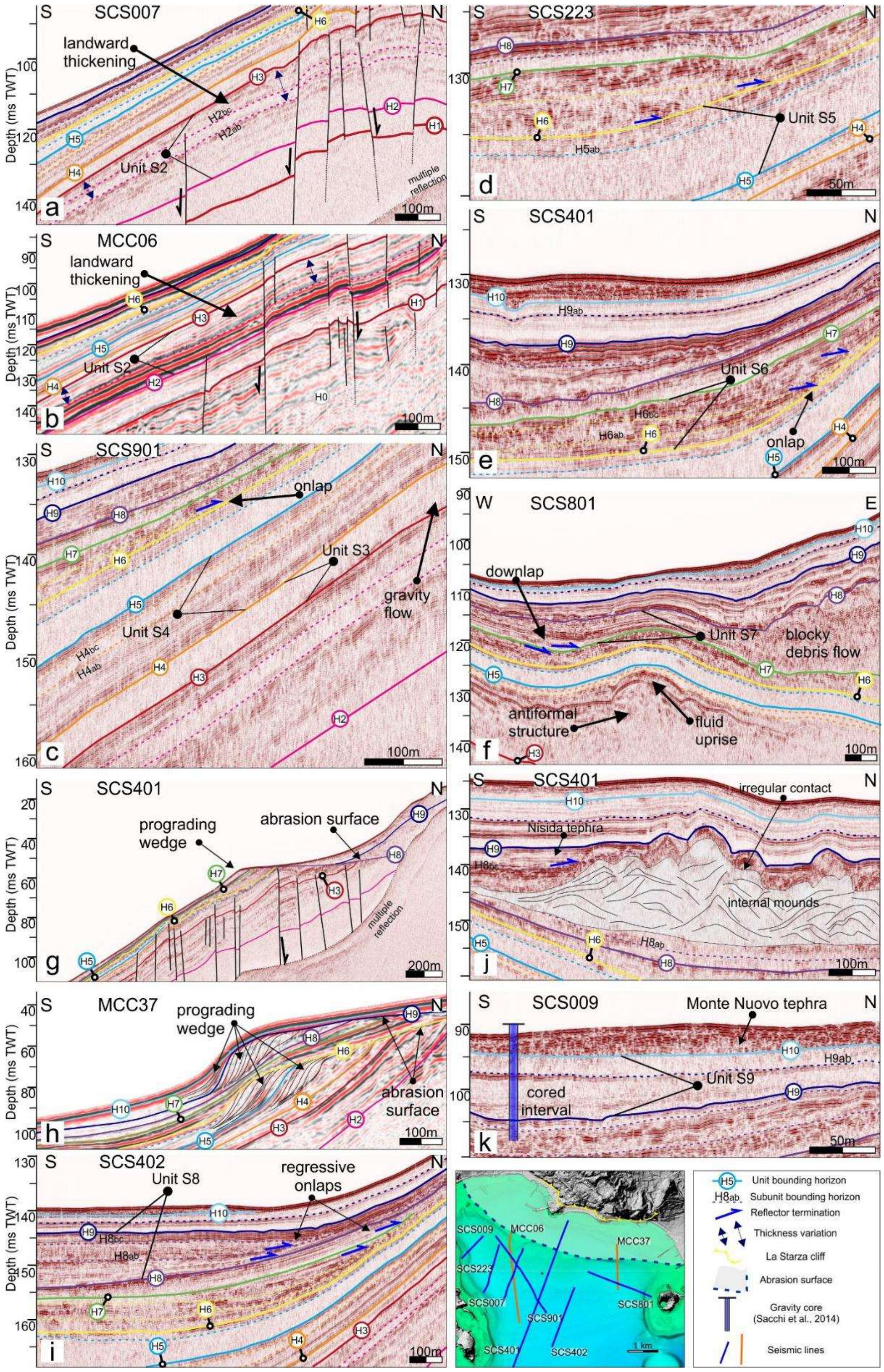

Figure 1.14. (a, b) Landward thickening of unit S2, bounded on top by horizon H3. (c) Main characteristics of units S3 and S4. (d) Unit S5 (e) Unit S6 and its three subunits and unit S9 seismic expression. (f) Antiformal structure. (g) Major abrasion surface (H8) topping the apical dome area. (h) Two generations of abrasion surfaces and prograding wedges on the eastern part of the gulf. (i) Regressive stacking pattern marked by shifted onlap terminations and subdivision of S8 unit. (j) Stratigraphic position of Capo Miseno tephra located in the upper part of S8b subunit. Map inset showing the location of the seismic lines (from Natale et al., 2021).

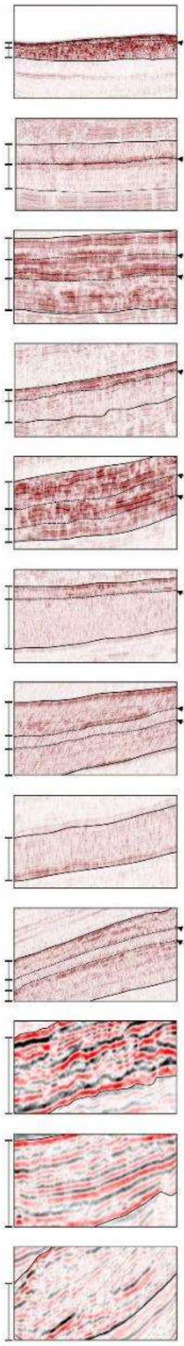

Seismic unit	Seismic sub-unit	Bounding horizon	Continuity	Seismic Amplitude	Reflection Configuration	Reference tephra/layer	Age range ka BP	La Starza Intervals
S10	S10b S10a	H10ab H10	Variable	High	Subparallel to chaotic	MN	0-0.6	
S9	S9b S9a	H9ab H9	Reflection free with interbedded continuous	Low with interbedded medium-amplitude reflections	Parallel to subparallel	AD 79	0.6-3.7	
S8	S8c S8b S8a	H8bc H8ab H8	Variable	High	Subparallel	CM, NIS AST-FOL AV-2-SOL	3.7-4.4	h3
S7	S7b S7a	H7ab H7	Discontinuous	Low to moderate	Subparallel to chaotic	PU	4.4-4.55	h2
S6	S6c S6b S6a	H6bc H6ab H6	Variable	High	Subparallel to chaotic	AMS MSA-PA2 AV1-CIG AG1-2	4.55-5.5	g2-h1
S5	S5b S5a	H5ab H5	Reflection-free and continuous	Low to moderate	Chaotic to parallel	rizholites beds paleosol B	5.5-9.1	f-g1
S4	S4c S4b S4a	H4bc H4ab H4	Continuous with interbedded reflection free	Moderate to high	Subparallel to chaotic	CSD-PSN B-FdB	9.1-9.6	d-e
S3		H3	Continuous	Low to moderate	Parallel	paleosol A	9.6-10.46	c
S2	S2c S2b S2a	H2bc H2ab H2	Continuous with interbedded reflection free	Moderate to high	Parallel	So1-PP	10.46-12.3	a-b
S1		H1	Continuous	Moderate to high	Subparallel	La Pigna Arch.AV	12.3-14.3	
S0		H0	Continuous	Low with interbedded high-amplitude reflections	Parallel to subparallel	LaP-GAU MOF-BV	14.3-14.9	
NYT			Discontinuous	Low with interbedded high-amplitude reflections	Chaotic	NYT	>14.9	

Figure 1.15. Seismic units and seismic patterns of the last 15 ka fill of the Pozzuoli Gulf, and related age attribution, reference tephra and correspective La Starza intervals (Smith et al., 2011; Bevilacqua et al., 2016; Isaia et al., 2019). NYT: Neapolitan Yellow Tuff; BV: Bellavista; MOF: Mofete; GAU: Gauro; LaP: La Pietra; So1: Soccavo 1; PP: Pomici Principali; B-FdB: Baia-Fondi di Baia; CSD: Costa San Domenico; PSN: Pigna San Nicola; AG1-2; Agnano 1-2; AV1: Averno 1; CIG: Cigliano; A3: Agnano 3; MSA: Monte Sant'Angelo; PA2: Paleoastroni 2; AMS: Agnano Monte Spina; PU: Pozzuoli Unit; AV2-SOL: Averno 2 – Solfatara; AST: Astroni; CM: Capo Miseno; NIS: Nisida; MN: Monte Nuovo (from Natale et al., 2021).

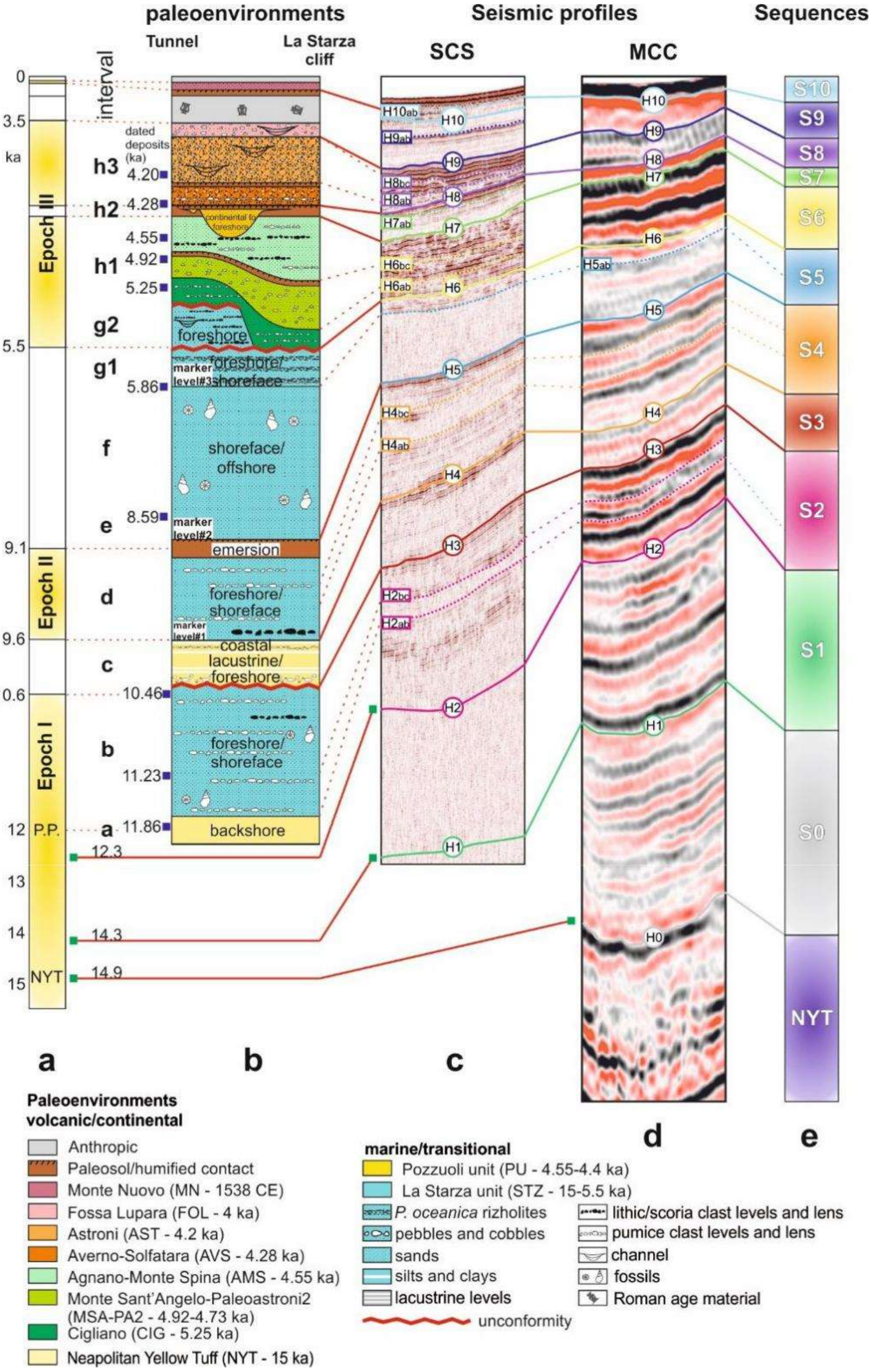

Figure 1.16. (a) Chronostratigraphic log of the post-NYT volcanism. (b) La Starza stratigraphic intervals (modified after Isaia et al., 2019), (c) SCS seismic type section with also indicated sub-horizons, (d) MCC seismic type section. (e) Seismic sequences and corresponding colour code adopted in the figures (from Natale et al., 2021).

1.8 Definition of seismic units

Figures 1.14, 1.15 and 1.16 show the seismic units and patterns of the last 15 ka fill of the Pozzuoli Bay, related age attribution and reference tephra related to La Starza intervals proposed by Natale et al. (2021). I have taken part in this study that describes the results of a companion PhD project at the University of Naples. Therefore, the general results of the above paper are incorporated in the present thesis as a basis for developing original observations and interpretations.

The following paragraphs illustrate the main features of the seismic units singled out by Natale et al. (2021) (Fig. 1.10). The seismic features and labelling used in this thesis reflect the terminology of Natale et al. (2021).

Unit NYT (Neapolitan Yellow Tuff)

Seismic unit NYT is the base of the caldera basin fill, as defined offshore by Steinmann et al. (2016). NYT generally exhibits chaotic seismic facies with mainly discontinuous, low to high amplitude reflections (Figs. 1.15, 1.16).

Units S0-S1

A facies of medium-amplitude, more or less continuous reflectors characterizes unit S0. It has an average thickness of ~20 m, which keeps almost constant moving from the present shelf to the basin until the inner border of the caldera, where it is confined. Unit S0 is bounded upward by a sharp seismic amplitude and continuity variation, defining unconformity H1. Compared to S0, the overlying unit S1 is defined by increased amplitude and continuity and a slight decrease of the reflection frequency. The sequence has an average thickness of ~10 m with no significant lateral variations (Figs. 1.15, 1.16).

Unit S2

A sharp variation in reflection attributes characterizes the transition between S1 and S2 units across H2. Unlike the underlying units, S2 shows high amplitude, high-frequency continuous reflectors. It includes three subunits, from bottom to top: S2a, S2b, and S2c. The lowermost S2a subunit exhibits constant thickness (~8 m) with high-amplitude reflectors and upward frequency decrease. Seismic facies and geometric features sharply change within overlying subunit S2b, showing marked transparent facies with poor lateral continuity and some parallel reflectors locally. The uppermost S2c subunit lies concordantly on top of S2b, showing more reflective facies, with continuous mid-amplitude and mid-frequency reflectors (Figs. 1.14, 1.15, 1.16).

Unit S3

S3 is identified by a sharp change of the internal characters of the seismic unit, featuring a 3.4 m thick sub-transparent facies with interspersed medium to high amplitude, discontinuous reflectors, particularly in its middle-top part (Figs. 1.14, 1.15, 1.16).

Unit S4

S4 is composed of three subunits (S4a-c). S4a is located at the base and is characterized by stratified medium-amplitude, mid-frequency reflectors, with higher amplitude upward, alternating with transparent reflectors mainly in its lower part with increasing thickness toward the collar area. Subunit S4b is characterized by sub-transparent facies with locally poorly continuous reflectors mainly toward its top and shows a gentle decrease in thickness from the basin to the dome (Figs. 1.14, 1.15, 1.16). Finally, a sharp contact characterizes the transition to the overlying S4c, represented by high amplitude continuous reflectors with significant thickening passing from the dome apical zone to the collar (Fig. 1.14c).

Unit S5

Sequence S5 features two sub-units (S5a-b). Subunit S5a is a well-recognizable stratigraphic marker in SCS and MCC lines (Marker B in Natale et al., 2020) that exhibits transparent facies with discontinuous low amplitude reflectors toward the top. It is characterized by marked thickness variations recording up to ~6 m in the collar zone. Subunit S5b includes medium-to-high amplitude parallel to sub-parallel reflectors, with a slightly variable thickness (averagely around 0.5 m), generally preserved in the dome area (Figs. 1.14c, 1.14d, 1.15, 1.16).

Unit S6

Unit S6 overlies with a paraconformity horizon H6 and is characterized by high and very-high amplitude, continuous to chaotic reflectors in the basin (Figs. 1.14, 1.15, 1.16). The basal contact evolves laterally to an angular unconformity toward the dome apical zone. This unit encompasses subunits S6a-c, separated by internal unconformities and representing discrete depositional events (Figs. 1.14e, 1.15, 1.16).

Unit S7

S7 shows a lobe-like, transgressive pattern in paleobathymetric lows and N-S oriented lines. This unit comprises the basal subunit S7a, defined by mainly transparent facies with interspersed high-amplitude continuous reflectors, displaying unconformable contact with the underlying sequence.

On the other hand, a sharp change in seismic facies, which shift toward higher amplitude and frequencies, is present within overlying S7b, which display continuous to chaotic reflectors (Figs. 1.14e, 1.14f, 1.15, 1.16).

Unit S8

In the basin, S8 overlies paraconformity H8, which evolves to an angular unconformity toward the dome area, producing a pronounced abrasion surface (Fig. 1.14g, 1.15, 1.16). This unit is divided into three subunits, as significant facies and geometric variations are recognized within the sequence. Subunits S8a and S8b highlight prograding onlap terminations and lobate features (Fig. 1.14i). The lowermost subunit S8a is marked by chaotic mid-amplitude and high-frequency reflectors showing a slight thickness increase from east to west. S8b is mainly composed of laterally discontinuous high amplitude reflectors. S8c, which represents a stratigraphic marker on both datasets, is composed of parallel stratified high frequency and amplitude reflectors that mantle the underlying sequences. Furthermore, this horizon was cored and calibrated by three gravity cores (Sacchi et al., 2014). To the west and east, its overall thickness increases toward Capo Miseno (Fig. 1.14j) and Nisida, respectively.

Units S9-S10

Unit S9 features low amplitude, locally transparent reflectors with a high-amplitude, continuous reflector halfway its thickness, and includes the Vesuvius 79 CE and Ischia 60 CE tephras, as recognized by Sacchi et al. (2014). The overall thickness in the collar zone ranges between 4 and 7 m, reaching its maximum value in the Epitaffio and Bagnoli valleys. Laterally discontinuous high amplitude reflectors characterize S10 with internal geometries and valley-ponding features in the Epitaffio valley, where it reaches its maximum thickness. This sequence has been calibrated with gravity cores and correlated to the 1538 CE Monte Nuovo tephra (Fig. 1.14k, 1.15, 1.16).

Chapter 2 – Datasets and Methods

The multichannel seismic data used in this thesis were acquired during two joint Italian-German and Italian-Hungarian research expeditions on the R/V URANIA in 2008 (CAFE_GeoB08) and 2014 (SEISTEC_2014), respectively (Fig. 2.1). This dataset was processed and provided by the Institute for Coastal Marine Environment of the National Research Council (IAMC-CNR) (Italy) and the University of Bremen. The seismic dataset was integrated with a marine Digital Terrain Model (DTM) analysis based on a mosaic of multibeam bathymetry provided by the ISMAR-CNR of Naples (Fig. 2.1; Somma et al., 2016).

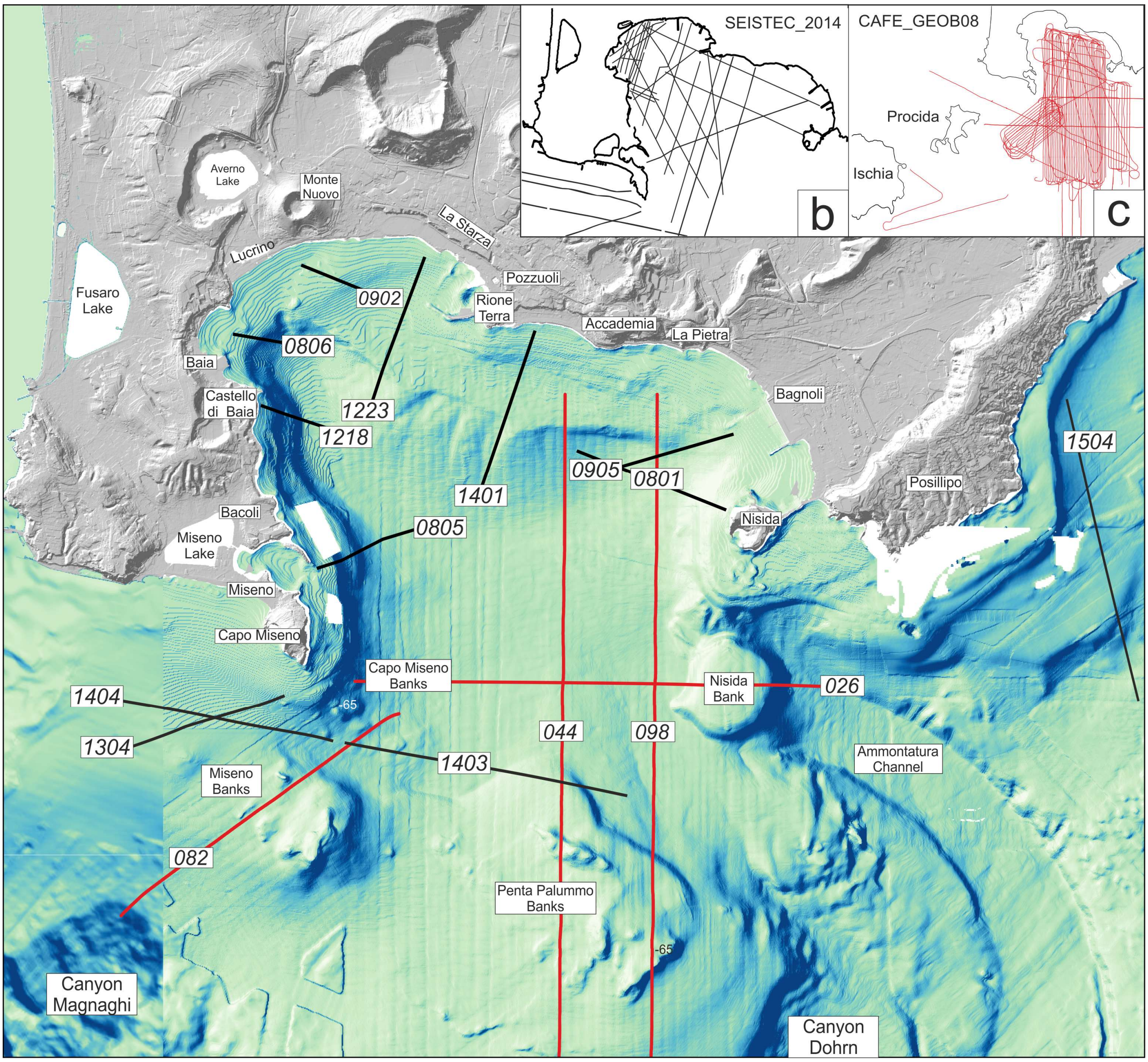

Figure 2.1. a) Seismic profiles showed in this study. b) Solid black lines: Seistec_2014 seismic profiles. c) Solid red line: CAFE_GEOB08 seismic profiles.

2.1 SEISTEC (2014) seismic profiles

The SEISTEC seismic profiles dataset includes a grid of more than 150 km of profiles acquired using the uniboom IKB-Seistec profiler (Simpkin and Davis, 1993; Mosher and Simpkin, 1999) (Fig. 2.1b). Seistec seismic lines were interpreted using the Geo-Suite AllWorks® software package (Geo-Marine Survey System, 2012). The SEISTEC system comprises a 2.5 m long catamaran supporting the boomer source and receiver (Fig. 2.2). The source is an IKB model B3 wide band electrodynamic "boomer" producing a single positive peak pressure impulse with a primary pulse width of 120 ms. The receiving system is a line-in-cone receiver adjacent to the boomer plate (70 cm). The source emits useful frequencies in the range 1–20 kHz and, thanks to this wide frequency band, allows the resolution of reflectors spaced 20 cm apart. Penetration is up to 100 m in soft sediments and 200 m in deep-water soft sediments. Vertical resolution reaches up to 0.1 m near the seafloor. A velocity of 1650 m/s (Sacchi et al., 2014) has been used for time to depth conversion. The depth-converted sections are displayed with a vertical exaggeration of 6–8× to enhance the visibility of low-angle stratigraphic boundaries and better display the internal architecture of the units. These profiles have a vertical resolution of 0.1 m and a horizontal resolution of 0.4 m. The seismic signal penetration is strongly influenced by the high signal attenuation of the volcaniclastic rocks, especially in tuffs and fluid-saturated sediments, and it typically reaches TWT depths between 100-150 ms.

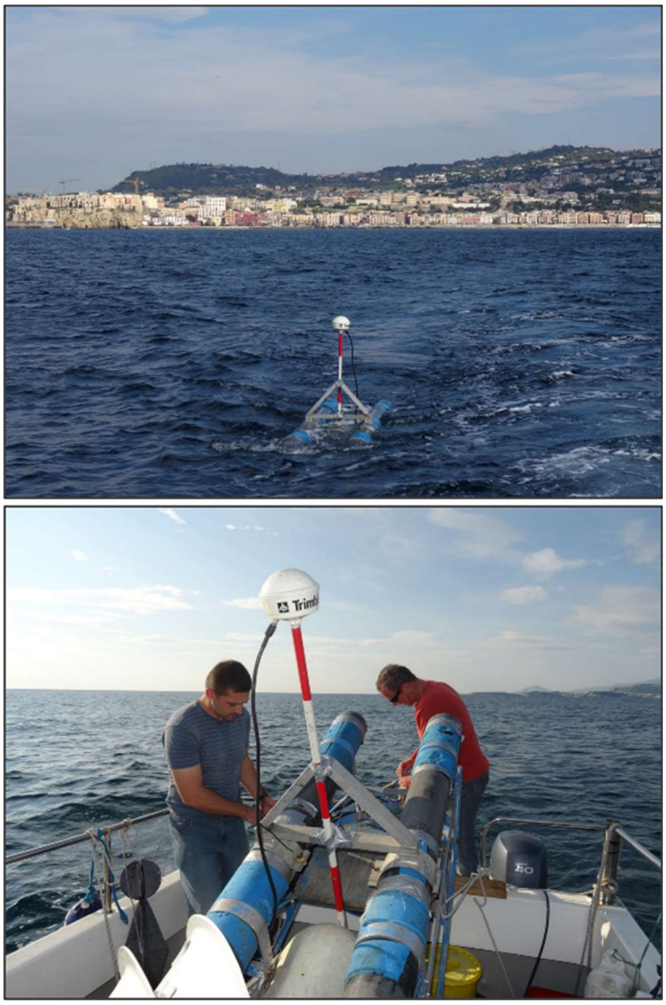

Figure 2.2. IKB-Seistec profiler setting in the Pozzuoli Bay.

2.2 CAFE (GEOB08) seismic profiles

During the CAFE cruise on the R/V URANIA in the Gulf of Naples and Pozzuoli Bay in January 2008, 146 multichannel seismic profiles with a total length of ~1.500 km were collected (Fig. 2.1c). The orientation of the grid profiles is mainly N-S trending (around 50 lines) with 10 E-W crossing lines and other 30 NE-SW oriented lines crossing the offshore sector of the Campi Flegrei caldera in the Pozzuoli Bay. The average lateral profile spacing grid was 120-150 m. Two seismic sources were deployed and shot alternatingly: (1) a Sodera GI-Gun with 2x1.7 L chamber volume and a frequency range of approximately 30-500 Hz and (2) a Sodera Mini-GI-Gun producing high frequencies of up to 1000 Hz. Both GI-Guns were towed at ~1.5 m water depth. These profiles have a vertical resolution of 2 m, a spatial resolution of 5 m, and a signal penetration exceeding 350 ms. The processing procedure (Steinmann et al., 2016) improved overall imaging depth compared to previous works in literature, allowing to follow seismic units beneath the shallow multiple reflections and the fluid-bearing layers.

2.3 Seismo-stratigraphic RSL indicators

The approach proposed in this thesis relies on detecting changes in the stacking pattern and facies of seismo-stratigraphic units used to reconstruct the Relative Sea-level (RSL) history at suitable locations in the bay. Seismo-stratigraphic bodies have been identified, and they are characterised by sigmoidal reflections indicative of depositional processes related to the storm wave-base level. These shore-parallel bodies are interpreted as infralittoral Prograding Wedges (PWs), which developed along the inner continental shelf margin (Casalbore et al., 2017). Although, they can be observed at different depths along the continental and insular shelf, forming during lowstand, transgressive and highstand conditions. The PWs typically form under the combined action of waves and across-shore currents, which causes the by-pass of infralittoral sediments across the margin to feed successively prograding clinoforms. As a result, a toplap surface, typically with sub-horizontal or gently inclined seaward topsets, develops on top of the prograding wedge (Fig. 2.3).

Each PW is formed by a series of clinoforms (foreset) characterized by a topset and a bottomset surfaces corresponding to the upper and the lower part, respectively. The convex-upward edge of clinoforms (or rollover point) is recognised in seismic profiles, and its depth is referred to storm wave-base level.

In Figure 2.3a, the black diamond on the first clinoform edge (PW top edge) represents the starting of a prograding phase, and the black circle on the youngest clinoform edge (PW base edge) is the end of progradation.

The development of PWs with sub-horizontal or slightly descending position (trajectory) of successive clinoforms edges marks a relative still-stand of the sea-level (Fig. 2.3a; Chiocci et al., 2011). When a clear difference in depth of clinoforms edges allows recognition of two (or more) distinct prograding bodies, this feature represents a down-stepping PW. This case has been interpreted as a temporary interruption of the still-stand by an abrupt RSL fall (Fig. 2.3b). The abrasion surface, merging seaward with the topset of the younger wedge, develops at the expense of the older wedge brought above the wave-base level (Fig. 2.3b).

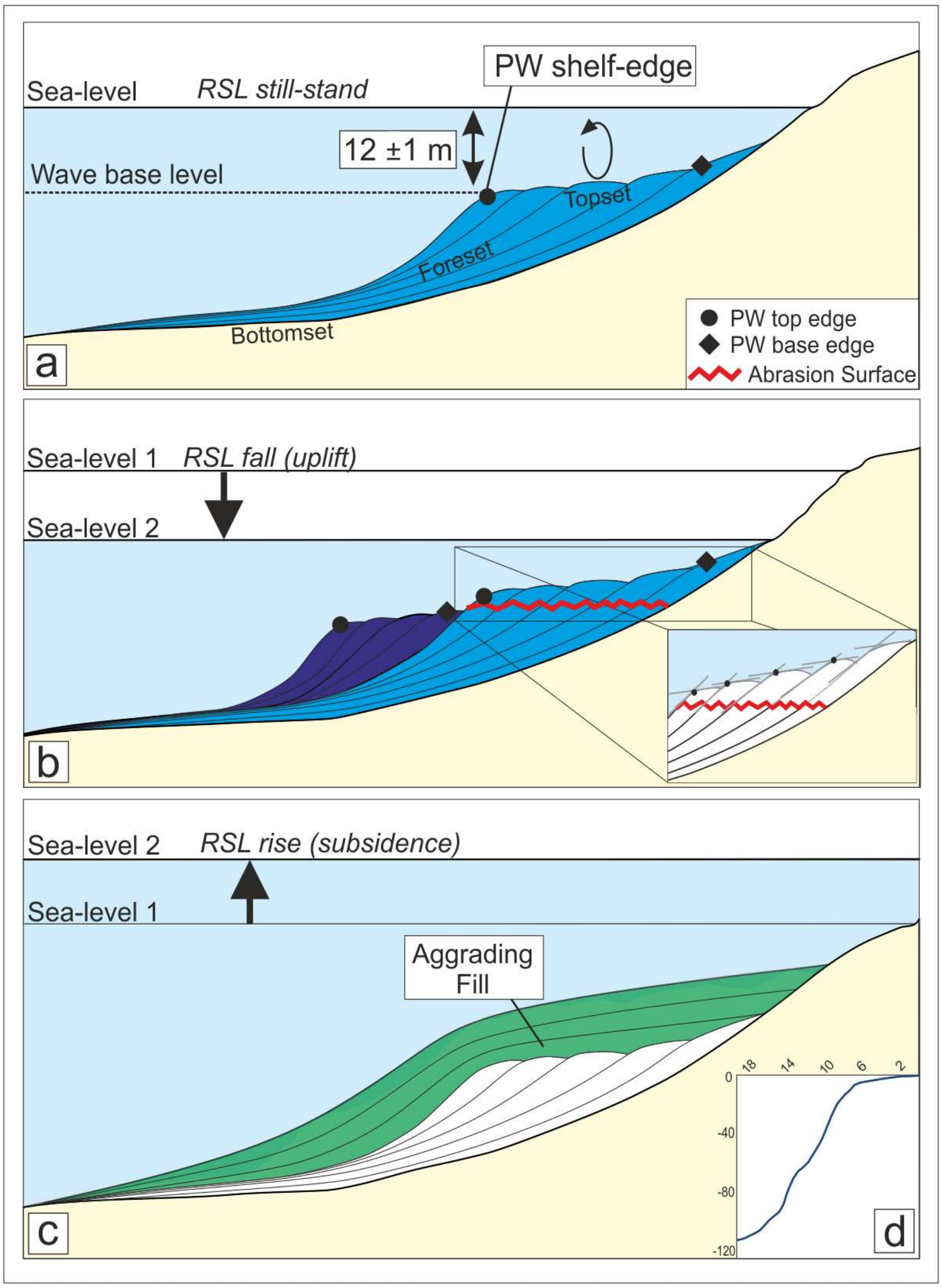

Figure 2.3. Seismo-stratigraphic RSL indicators. a) Prograding Wedge (PW) developing during an RSL still-stand; b) Compound prograding wedges (light-blue and dark-blue) developing during an RSL fall; c) Aggrading Fill (AF) developing during an RSL rise. d) Sea-level curve (from Lambeck et al., 2011).

This erosion of the topset of the older wedge hampers an accurate picking of the wedge shelf-edge. Therefore, it has been provided with a graphical reconstruction of the eroded wedge based on the geometric similarity with preserved PWs (size and length) and its internal stratigraphical pattern (clinoform inclination) (Fig. 2.4).

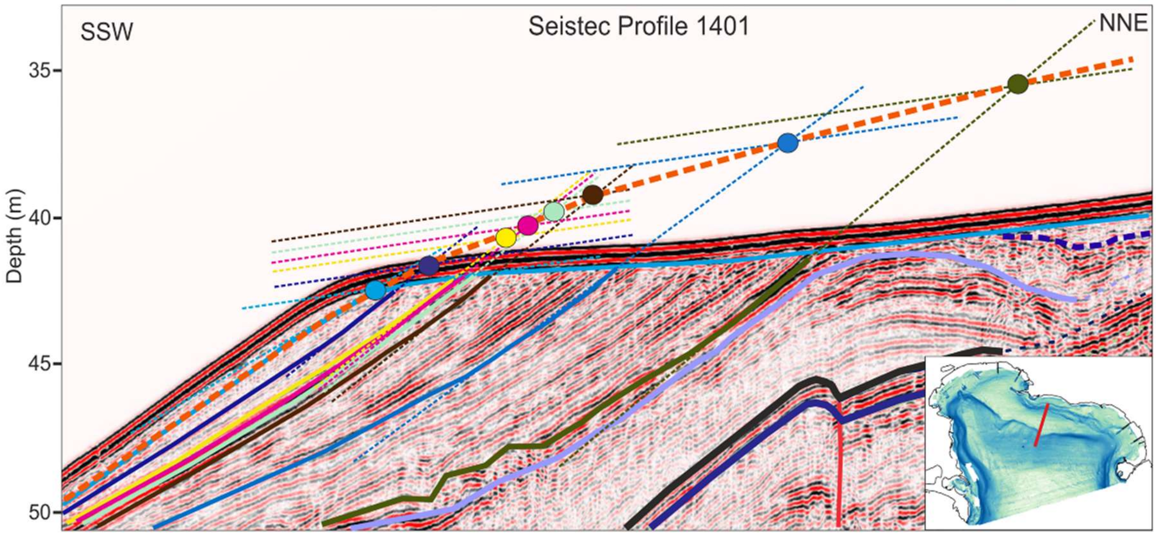

Figure 2.4. Graphical method to reconstruct the paleo-shape of the prograding wedge.

The prograding wedges studied here are intercalated with aggrading basin fills (AF), which formed below the wave-base level. The development of an AF that mantles an older wedge documents an RSL rise (Fig. 2.3c).

In the Pozzuoli Bay, the development of the basin fill, including PWs and AFs, was controlled by the interplay of local processes, such as volcano-tectonics movements and sedimentary inputs, with external forcing related to global and regional sea-level changes. Sea-level changes in the Mediterranean Sea were determined by the temporally variable eustatic change and by the spatially uneven glacio-hydro-isostatic response to glacial-interglacial cycles at the level of the mantle-crust boundary (Lambeck et al., 2011; Anzidei et al., 2014). Since the Last Glacial Maximum (~20 ka), the sea-level rose from ~120 m to its current position in this part of the Mediterranean (Fig. 2.3d). The rate of sea-level rise was fast and punctuated by brief slowing until ~6.8 ka when it progressively decreased until today rate.

Assignment of a storm wave-base depth, based on available present-day observations, allows to refer old PWs to their coeval SL and thus to infer RSL changes. Estimates of this depth vary by location and are greater (20-30 m) in exposed settings like ocean-bounded shelves (Hernández-

Molina et al., 2000). For the relatively more sheltered setting of western Calabria in the Mediterranean Sea, Pepe et al. (2014) proposed a 20 m water depth formation for the PW edge.

Considering that the Pozzuoli embayment forms a secondary inlet of the Gulf of Naples (Fig. 1.2), a shallower depth for PW edge formation at 12±1 m in the Pozzuoli Bay has been estimated (Fig. 2.3a). This estimate has been built on the meteo-marine data analysis computed by Benassi et al. (2006) of and carried out between 1999-2000 that compare the significant wave heights simulated in different coastal zones within a 200 m ray from the Gulf of Pozzuoli. The simulations show that the maximum height of the waves of ~3.5 m at Pozzuoli Bay is due to the circumstance that this location is partly sheltered. Diversely, in the Gulf of Naples, maximum wave heights of more than ~5.5 m have been measured because this represents a more exposed sector.

The depth uncertainty for PW edges includes the contribution from various error sources (measurement, velocity assignment to seismic units for time-to-depth conversion, paleo-bathymetry estimates, paleo-sea level position). The PW depth uncertainty adopted here is the spatially averaged uncertainty on predicted sea-level provided by Lambeck et al. (2011). This uncertainty includes inaccuracies in paleo-sea level position is ±1 for markers younger than ~3.7 ka and is ±2 m for older markers (Fig. 2.3d). This depth uncertainty that increases in time is given not only by the paleo-sea level prediction of Lambeck et al. (2011) but also by the variable geometric characteristic of the PWs. In particular, the vertical and lateral extension of the PW has changed through time because the older ones (5-10 ka) are larger and better developed than the younger ones (last 1 ka). The PW older than 5-10 ka have a lateral development of ~500 m, while the youngest ones of ~50 m.

The relative chronology of PWs and intercalated AFs (Table S1) was reconstructed by correlating the boundaries of these seismic bodies with some of the seismic reflectors identified in the basin fill by Natale et al. (2021). The age uncertainty derives from the error associated with absolute ages that date the identified reflectors and is generally limited to a few centuries.

When a difference exists between the observed depth of a PWs and the coeval position predicted by sea-level curves, it is possible to infer the occurrence of positive or negative vertical displacement. Thus, correction for sea-level changes allows calculation of the vertical tectonic component. This study uses the sea-level prediction by Lambeck et al. (2011) for site n°8 (about 10 km north-west to Pozzuoli), the closest to the CF caldera, including its time-dependent uncertainty.

Thanks to intersection points between seismic lines, it was possible to reconstruct the distribution of picked horizons in the Pozzuoli Bay (Fig. 2.5). According to the seismo-stratigraphic reconstruction performed by Natale et al. (2021), it was possible to trace the key seismic horizons to constrain the development and ages of prograding wedges and aggrading fills used in this thesis.

Major seismo-stratigraphic elements recognized offshore are shown in Figure 2.5 and include:

(a) the presence of high amplitude and high-frequency reflectors interbedded with more transparent and chaotic seismic facies.

(b) structural elements such as faults and anticlines.

(c) the presence of blanketing zones of reflections within the profiles indicates preferential paths for fluids ascending through the shallower sediment layers.

d) When the continuity of seismic reflectors was lacking due to acquisition interruption or slumping events, a step-over method was used to continuously interpret horizons (inset in Fig. 2.5c).

e) different generations of prograding parasequences system at different depths (Fig. 2.5d).

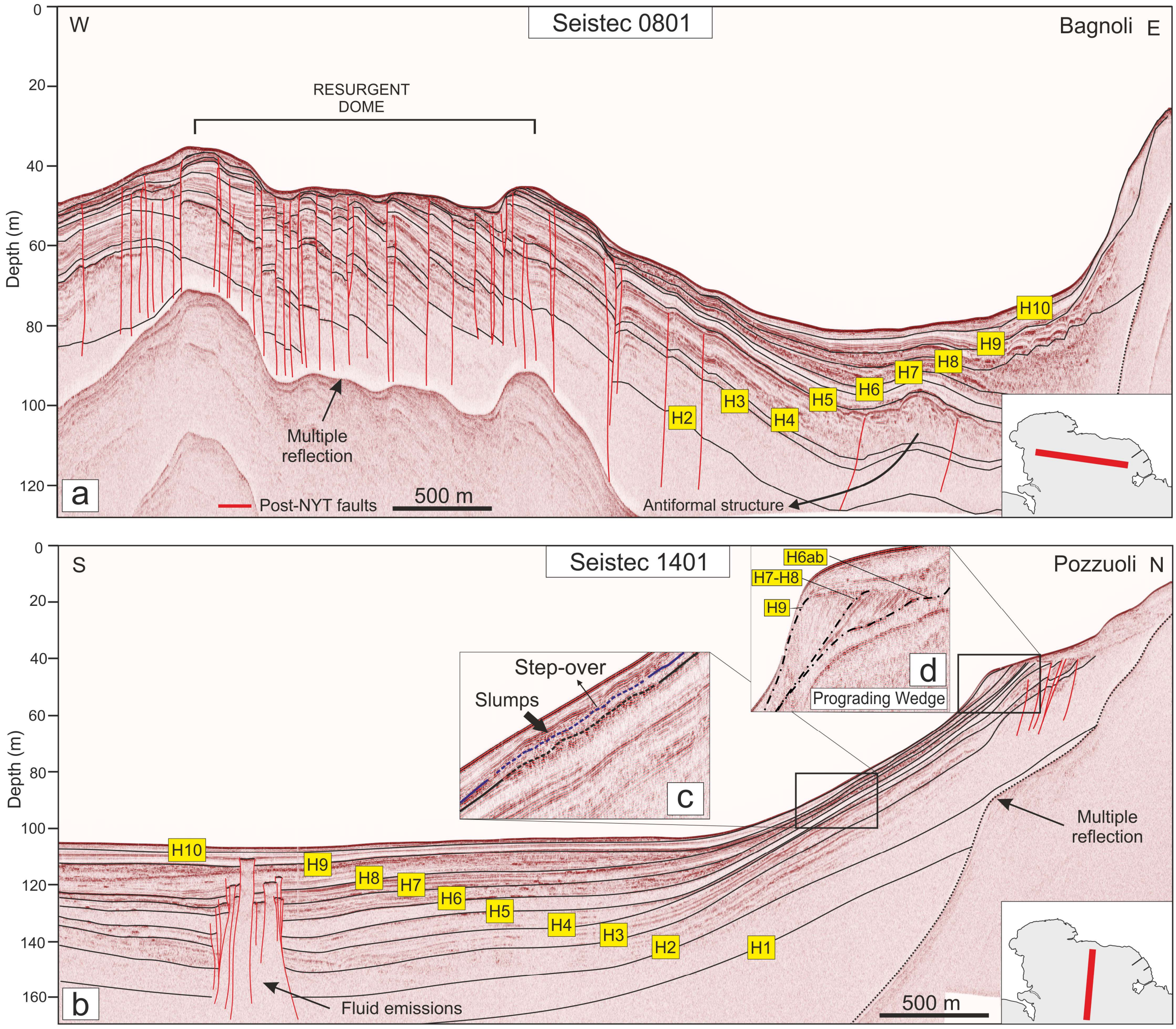

Figure 2.5. Interpreted seismic profile showing the sedimentary infill, traced seismic horizons (H1 to H10) and structural elements in the offshore sector of the caldera. a) E-W oriented line (SEISTEC_0801). b) N-S oriented line (SEISTEC_0401). c) step-over method used to continuously interpret the seismic horizons. d) Evidence of prograding wedge and its relative seismic horizons.

2.4 Archaeological RSL indicators

Archaeological remains of ancient maritime coastal settlements located in zones of small tidal ranges can provide information on RSL changes. In this thesis, the archaeological structures have been used to define the relationship to sea-level at the time of construction (e.g., Lambeck et al., 2004; Anzidei et al., 2014; Anzidei et al., 2016). The CF caldera's archaeological indicators of paleo sea-level are extensively found because of its strategic position on ancient maritime routes, favourable climate, and abundance of resources that encouraged an attractive settling place since the early Greek colonisation.

Several submerged archaeological sites mainly testify to historical coastal modifications, such as Portus Julius and Pisoni villa. These remains belong to the Roman age and are dated between the 1st century BCE (Before the Common Era) and the 1st century CE (Common Era) and nowadays are now positioned in a depth range between -5 and -2 m b.s.l. (Passaro et al., 2013). However, the most studied archaeological site in this area is the "Macellum", the ancient Roman market, the so-called "Serapeum templum", located in Pozzuoli (Parascandola, 1947; Cinque et al., 1985; Morhange et al., 2006 and references therein). The lithophaga perforations on the central part of its columns nowadays positioned at 7 m above the sea level have been long used as a paleo sea-level gauge (Lyell, 1830, Morhange et al., 2006) and can be considered an important witness of fast RSL variations due to bradyseismic crisis in this site. The archaeological data used in this thesis (Table S2) located between the Gulf of Naples and Pozzuoli (Fig. 2.6) include original observations of Roman Age structures (sites 1 to 16; Fig. 2.7) and an additional dataset of published measurements (sites R1 to R8; Fig. 2.8).

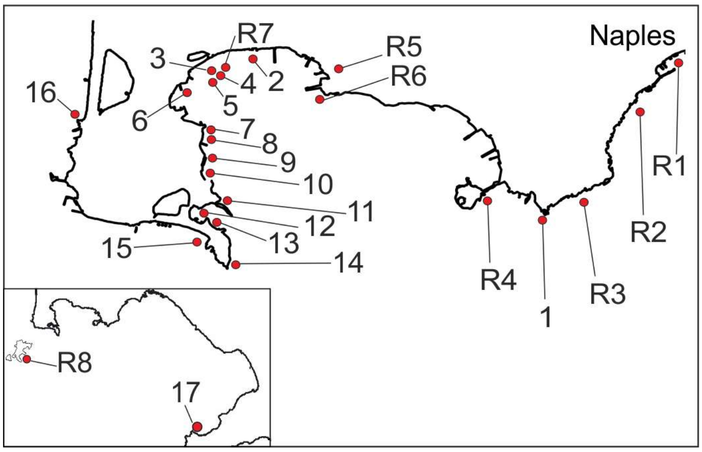

Figure 2.6. Map of coastal archaeological data distribution (red dots) from original data (numbers) and published (R-numbers) in the Pozzuoli Bay and Gulf of Naples.

Archaeological remains at sites 1 to 16 were surveyed between 2011 and 2018 and corrected for tides using the national tide gauge station POPT located in Pozzuoli Porto (INGV website).

The archaeological indicators fall into three classes (Auriemma and Solinas, 2009), which have different reliability in past sea-level positioning, as reflected by the variable uncertainty.

The first class is represented by harbour structures (HA) and includes pillars (PR), docks (DK), and bollards (BL) (Figs. 2.7c, d, f; 2.8a, b; 2.9a). The pillars (*pilae*) were used as breakwaters or reefs to protect the harbour from storms and form bases for dock piers. Estimation of functional elevation (i.e., the emerged part to the average sea-level at the time they were operational) changes depending on the specific use of the pillars (Auriemma and Solinas, 2009). The docks were used as a walkway to reach the boats and for loading goods. The bollards represent small structures connected to docking to moor the boats and are ring-, cylindrical- or mushroom-shaped (Figs. 2.8a, b). For this class, a functional height of 0.6±0.2 m has been considered (Antonioli et al., 2007).

The second class consists of structures built at sea level in the tidal range. These fish tanks (FT) or *piscinae,* introduced between the end of the second century BCE and the beginning of the first century CE for fish culture (Figs. 2.7a, b, g; 2.8c to f; 2.9b). The fish tanks related to the maritime villas built between the 1st century BCE and the 1st century CE are accurate markers in the studies of RSL changes (Antonioli et al., 1998; Lambeck et al., 2004; Auriemma and Solinas, 2009; Evelpidou et al., 2012; Morhange and Marriner, 2015). The fish tanks consisted of single or multiple tanks used for fish farming (Varro, 37 BCE; Columella, 30 CE) interconnected with the open sea through channels, specifically the tidal range. In their treaties, Varro and Columella described the different construction techniques for fish tanks, which varied according to the coastal type. There are essentially three constructional elements directly linked to the sea level at the time of fish tank's construction: *crepidines* (a foot-walk border surrounding the tank and the internal pools); channel system (canals which allowed tidally controlled water exchange); *cataractae* (closing gates located at the access of the canal into the basin or the communication passage between each tank). A functional height of 0.2±0.1 m has been adopted (Lambeck et al., 2004).

The last class is represented by structures built onland and includes floors (FL) and roads (RD) (Figs. 2.7h; 2.9c). A functional height of 1.0±0.4 m is estimated for roads considering their minimum operation range and the local geomorphology (Anzidei et al., 2014). The FL data analysed in this thesis is represented by the marble pavement of the *Macellum,* constructed around 80 BCE during the Flavian epoch. Since historical times, lithophaga perforations on the columns' central part have long been used as a paleo sea-level marker (Fig. 2.7e). However, in this thesis, the marble floor has been used as the main archaeological marker, and its RSL elevation has been estimated at +3.1 m (Bellucci et al., 2006) (Fig. 2.9d).

This estimation provides the functional height for the *Serapeum* site at construction. The functional height specific to each marker has been used to derive the coeval paleo sea-level that, compared to the predicted Roman eustatic curve (Lambeck et al., 2011), which provided an estimation of net ground motion during the last 2 ka BP.

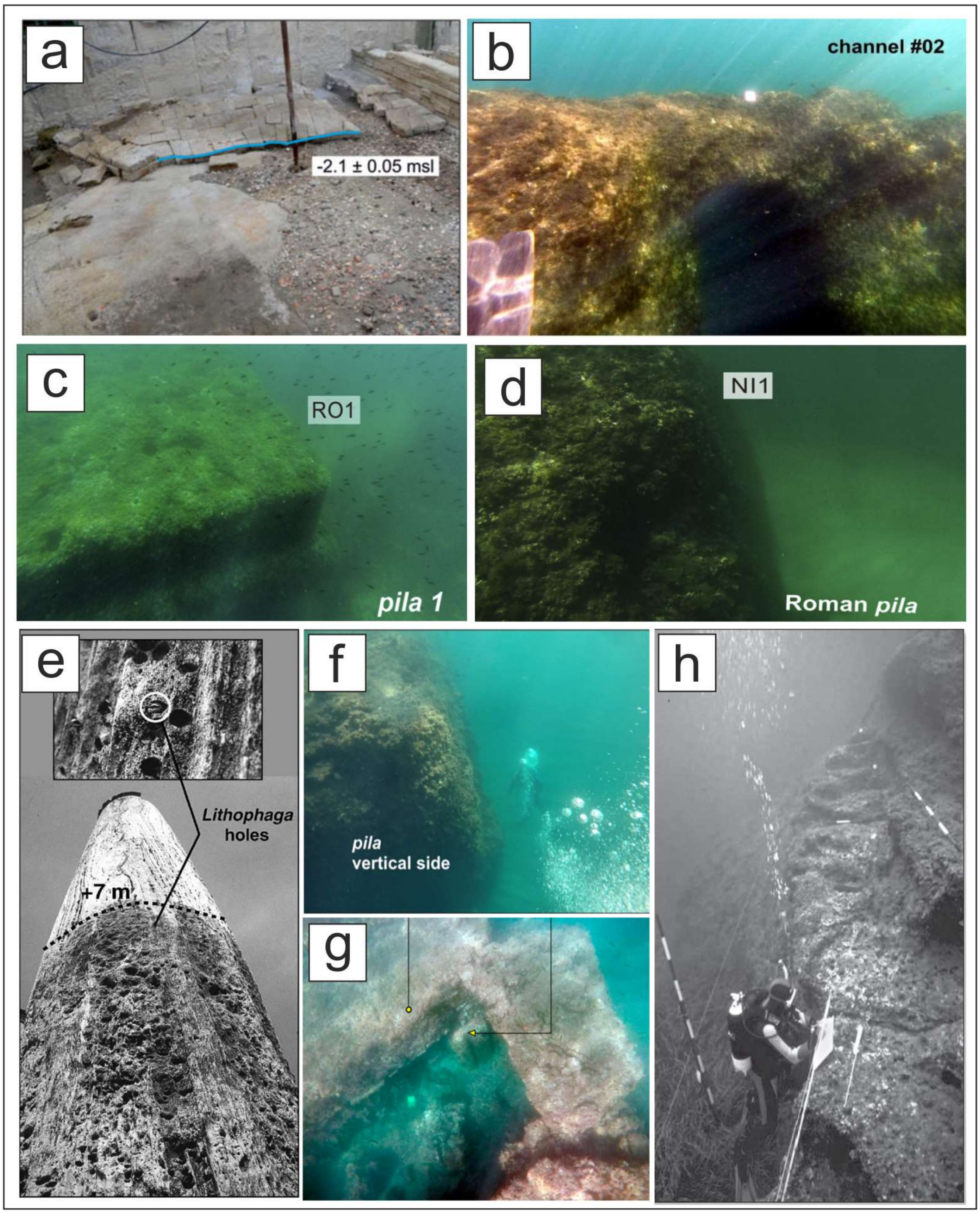

Figure 2.7. Archaeological sites from published data a) Fish tanks walkway off in Naples port (site R1; Vacchi et al., 2019). b) Fish tank off to Castel dell'Ovo (site R2; Pappone et al., 2019). c) Pier off to Marechiaro (site R3; Aucelli et al., 2019). d) Pier off to Nisida (site R4; Aucelli et al., 2019). e) Macellum (Serapeum) marble columns (site R5; Morhange et al., 2011). f) Roman piers in Rione Terra offshore (site R6; Aucelli et al., 2018). g) Fish tanks in Portus Iulius (site R7; Aucelli et al., 2020). h) Bronze-Age to roman-age stepped stairs (site R8; Putignano et al., 2014).

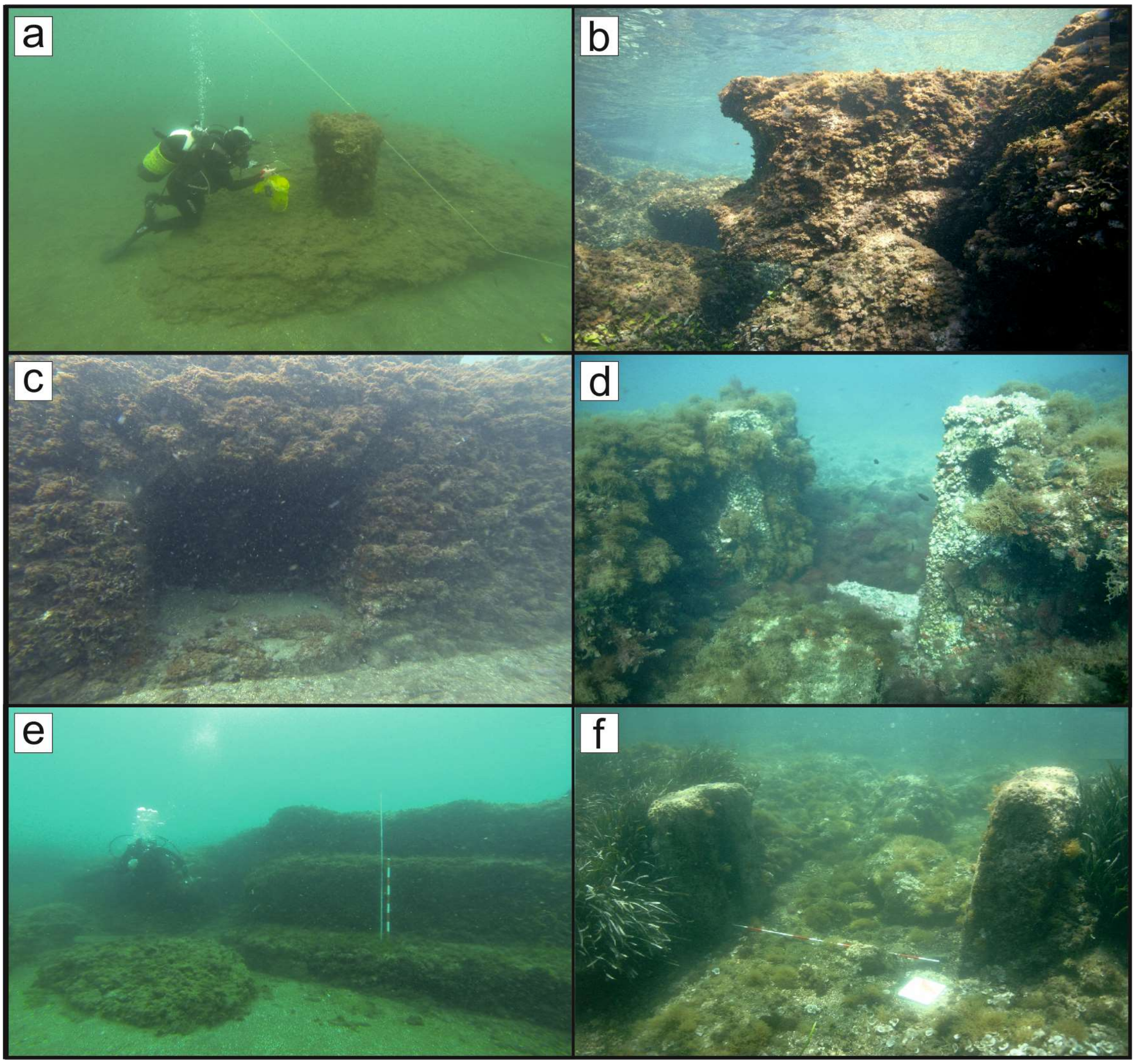

Figure 2.8. Original archaeological data analysed in this thesis. a) Channel of the fish tank at Gaiola islet (site 1). b) Bollard and the pier located offshore M. Nuovo (site 3). c) Channel of the Portus Iulius fish tank offshore M. Nuovo (site 5). d) External walls of the fish tank located offshore Castello di Baia (site 7). e) Channel of the Punta Pennata fish tank (site 11). f) Bollard of the military harbour at Capo Miseno (site 12).

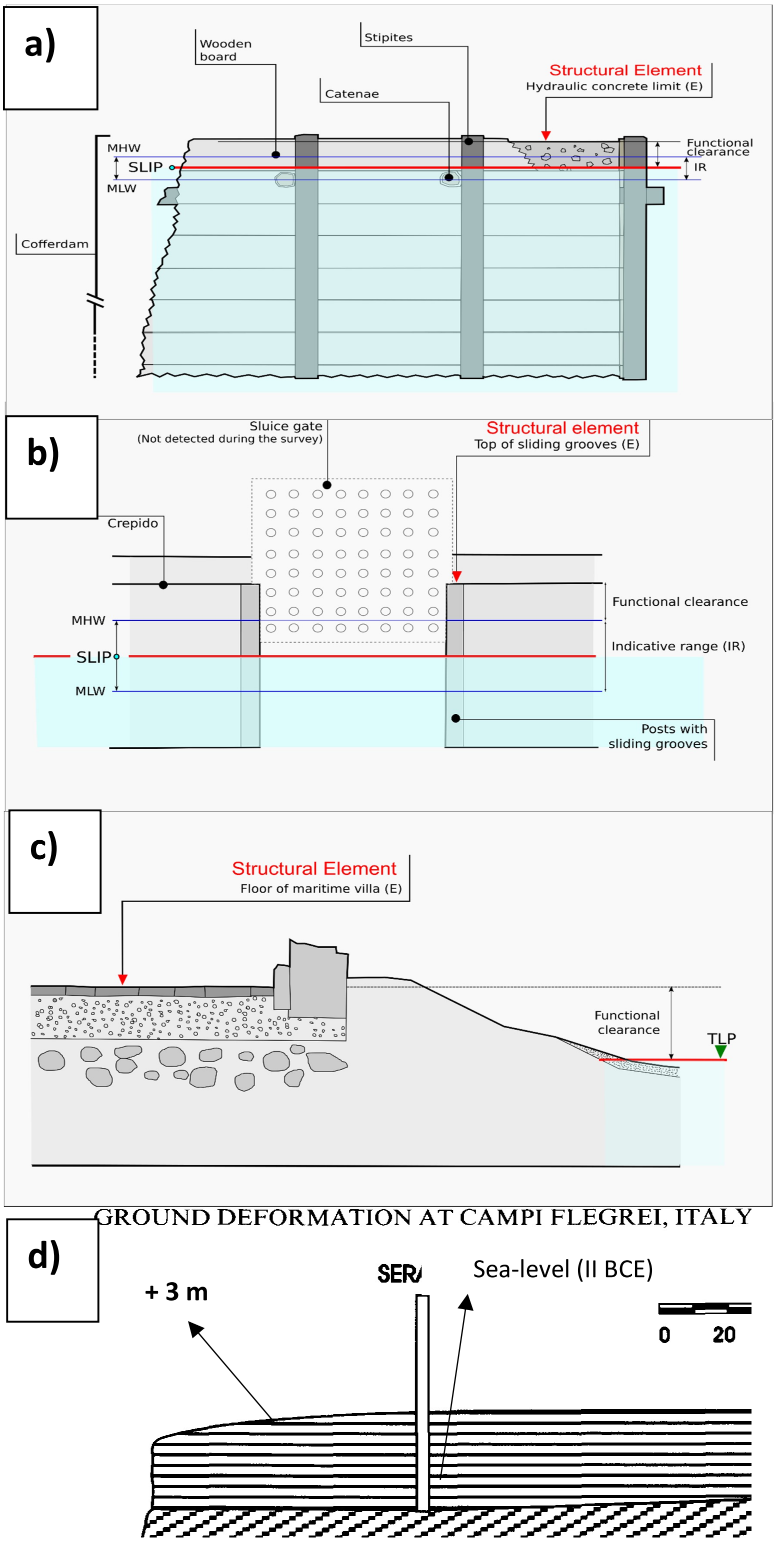

Figure 2.9. a) Pillar. b) Fish tank. c) Villa floor (from Aucelli et al., 2020). d) Serapeum floor (from Bellucci et al., 2006).

Chapter 3 – RSL indicators in the Campi Flegrei caldera offshore

3.1. Morpho-bathymetric analysis for RSL indicators

The high-resolution bathymetric map of the Pozzuoli Bay and its most peripheral areas shows a set of stepped terraces on the shelf and the upper part of the slope (Fig. 3.1). These terraces are associated with the PWs observed in seismic profiles and are limited seaward by a sharp bathymetric break coinciding with the PW edge (Figs. 3.2 (a to h) and 3.3 (a to d)).

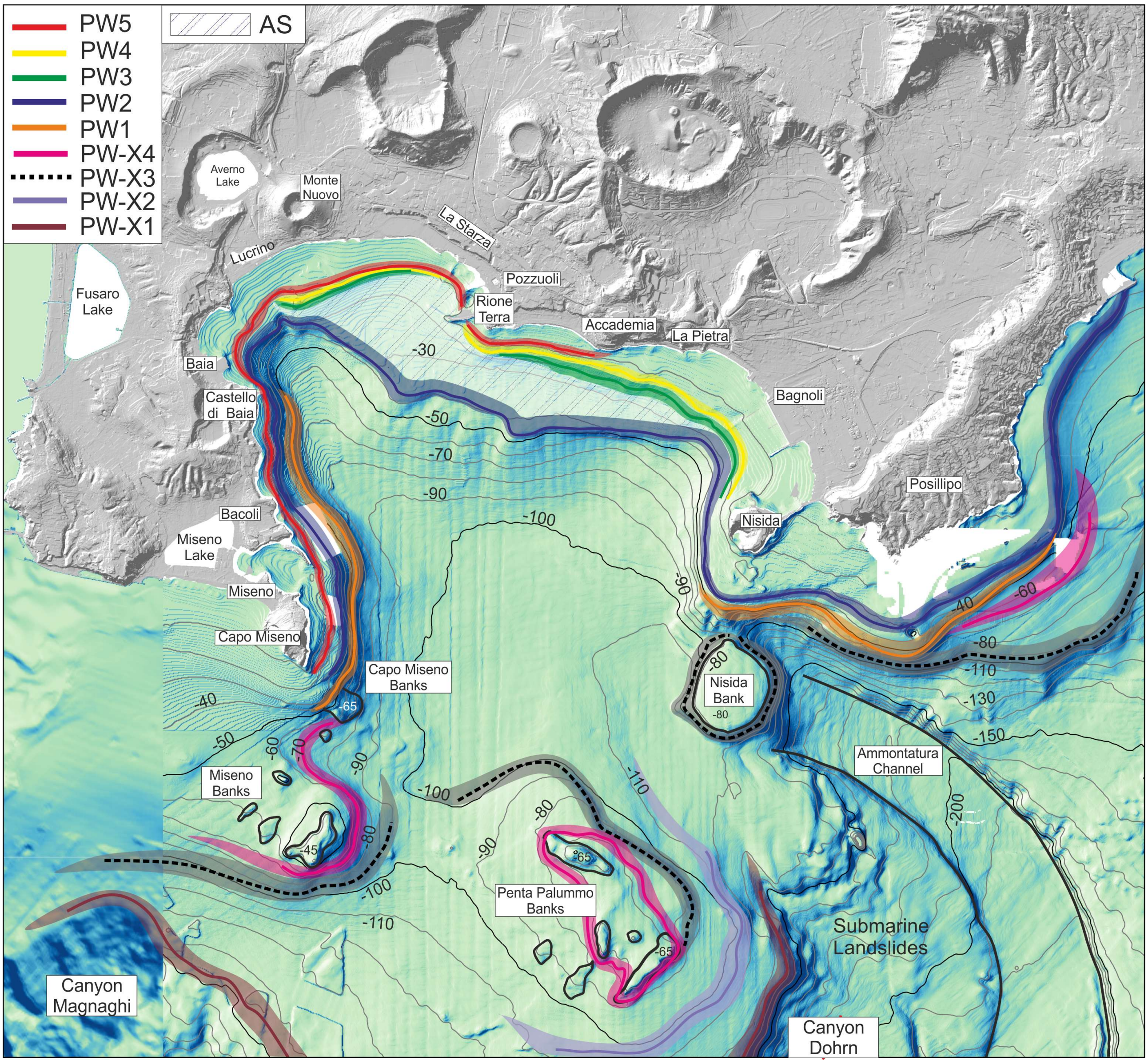

Figure 3.1. Distribution of depositional terraces (coloured areas) corresponding to prograding wedge (PW) edges (coloured solid/dotted lines) in the Pozzuoli Bay. PW1 to PW5 are referred to PWs younger than 10 ka and located in the internal part of the Pozzuoli Bay. PW-X1 to PW-X4 are referred to the PWs older than 10 ka and located in the external part of the Pozzuoli Bay.

.

The deepest terrace inside the CF offshore caldera is observed in the western sector of the bay from Castello di Baia to Miseno at a depth of 60-65 m, and its edge is identified as PW1 (Fig. 3.1). A shallower terrace (PW2) has an outer shelf-edge that develops at depths of 20-25 m and 30-35 m in the western (Baia to Miseno) and eastern sectors (Bagnoli to Nisida), respectively (Figs. 3.1; 3.2g and 3.2h). The central sector of the bay is characterised by a 1-2 km wide, NW-SE trending flat shelf developed from Monte Nuovo to Bagnoli offshore. The shelf-break is limited by a terraced body corresponding to PW2, whose outer edge is found at depths that increase from 20 m in the northwest up to 42 m in the southeast (Fig. 3.2).

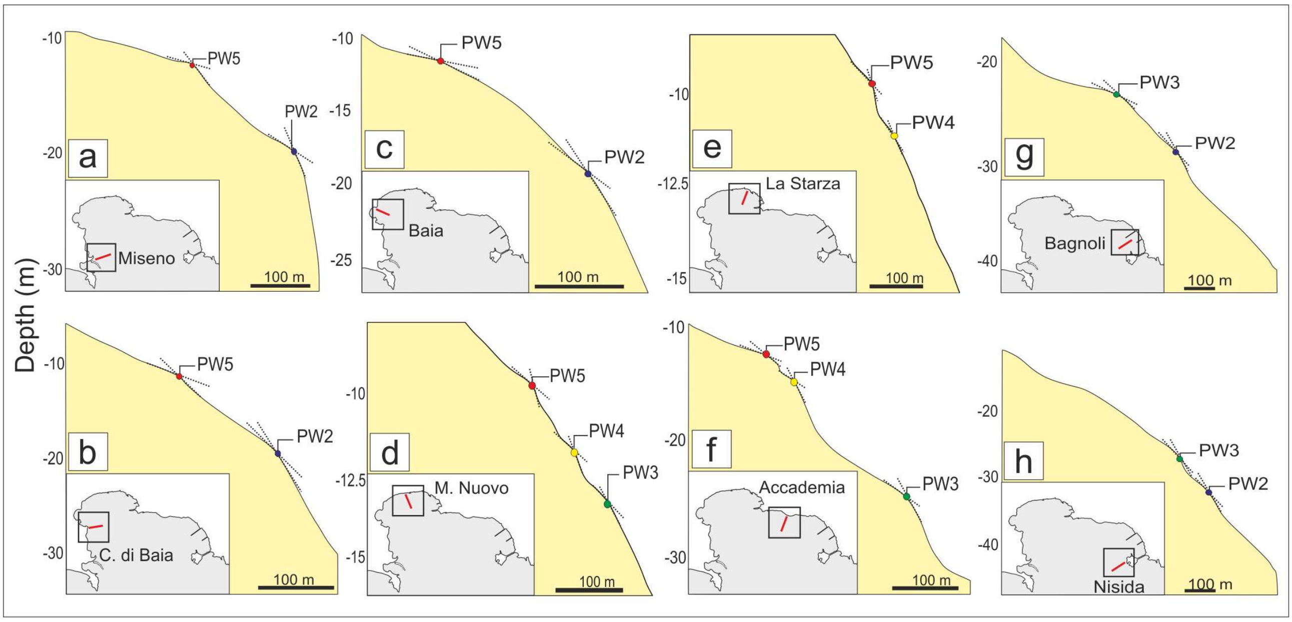

Figure 3.2 (a to h). Bathymetric profiles across the inner continental shelf and slope of the Pozzuoli Bay show terraced surfaces and associated outer rims (coloured dots) corresponding to the edges of PW2 to PW5. Bathymetric profiles are located along or nearby the traces of seismic lines.

Three shallower terraces are developed on the inner part of the shelf and have a relatively narrower width compared to deeper terraces. Between Rione Terra and Accademia, these upper terraces associated with PW3, PW4, and PW5 have outer edges at depths of 22-24 m, 15-17 m, and 10-12 m, respectively (Figs. 3.2, 3.2e and 3.2f). The deepest and intermediate inner shelf terraces PW3 and PW4 merge, moving west beneath Rione Terra (Fig. 3.1). Further to the west, between La Starza and Monte Nuovo, the two deeper terraces reappear beneath the shallower terrace (PW5), whose edge is found at 10-15 m depth. This uppermost terrace limits seaward a SW-NE trending up to 1 km wide coastal embankment that overhangs the deeper NW-SE trending shelf (Fig. 3.1).

In the western sector between Baia and Miseno, terraces associated with PW3 and PW4 are not present. Only the shallowest PW5 is identified with an edge depth at 12 m, together with PW2

(Figs. 3.1, 3.2a to 3.2d). In the eastern sector, from Accademia to Nisida, the three terraces PW2, PW3, and PW4 are observed with edges at depths of 35, 25, and 17 m, respectively.

The deepest wedge outside the CF offshore caldera is observed south of the Penta Palummo and Miseno Banks, at the border of the Canyons Dohrn and Magnaghi at a depth of 150-160 m, and its edge is identified as PW-X1 (Figs. 3.1, 3.3a, b).

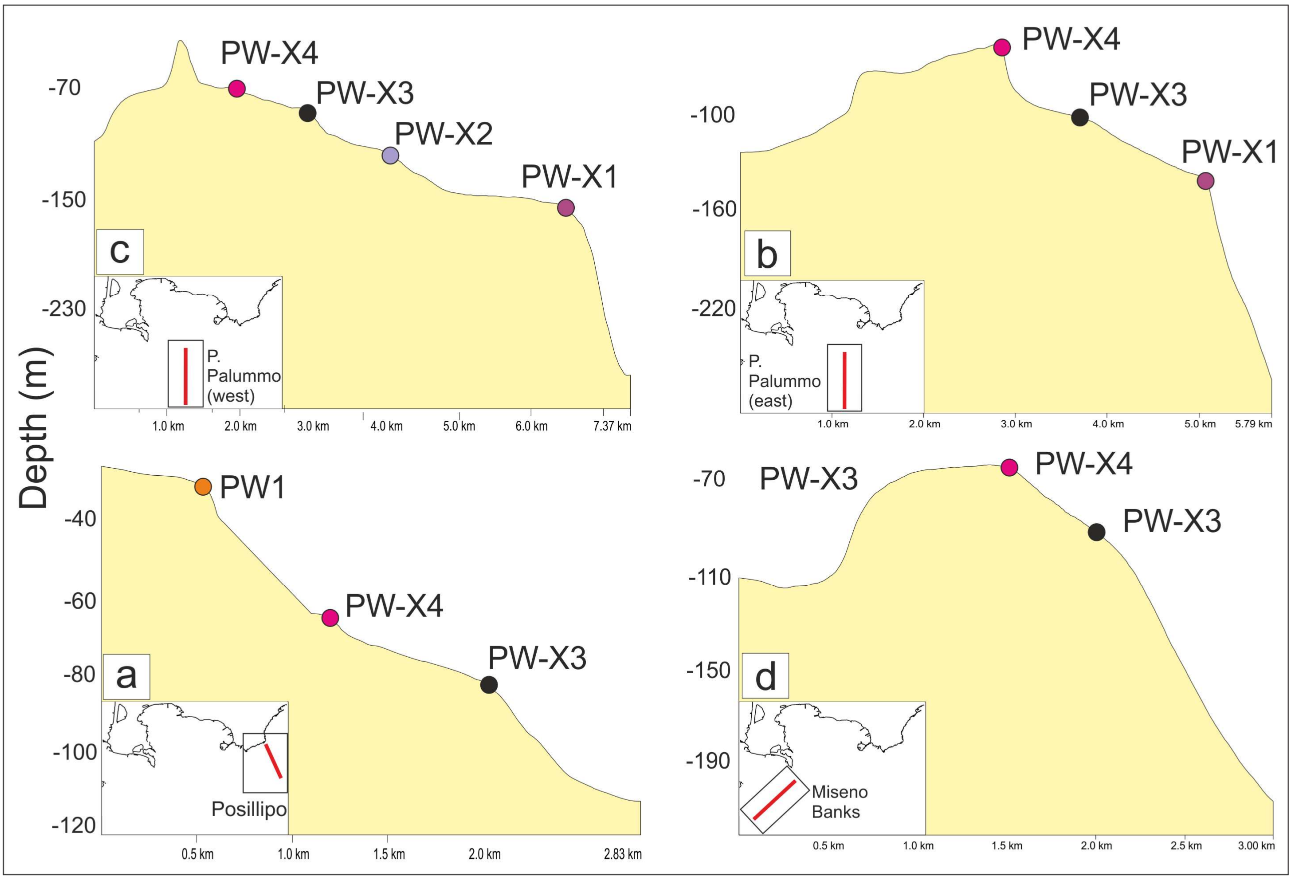

Figure 3.3 (a to d). Bathymetric profiles across the outer sector of the Pozzuoli Bay show terraced surfaces and associated outer rims (coloured dots) corresponding to the edges of PW-X1 to PW-X4. Bathymetric profiles are located along or nearby the traces of seismic lines.

A shallower wedge (PW-X2) has an outer shelf-edge that develops at a depth of 110-120 m in the south-eastern flank of Penta Palummo Banks (Figs. 3.1; 3.3a). A well-developed wedge PW-X3 is found off to the coast of Posillipo, around Nisida Bank and in the south-eastern flank of Penta Palummo and Miseno Banks at a depth of 90-100 m (Figs. 3.1, 3.3a to d). The shallowest wedge outside the CF caldera is PW-X4 and is observed in the same areas of PW-X3 at a depth of 70-80 m (Figs. 3.1, 3.3a to d).

3.2. Seismo-stratigraphic analysis

3.2.1 The Pozzuoli Bay

The morpho-bathymetric analysis discussed above supports the seismo-stratigraphic analysis that led to the recognition of different generations of PWs on seismic profiles, considering that morphological slope breaks can be related to different processes (Table S1).

The deepest wedge (PW1) recognized in the internal part of the Pozzuoli Bay is only observed in seismic lines in the western sector of the bay between Castello di Baia and Miseno (Figs. 3.1, 3.4a, 3.5a). The clinoforms are well developed in the older part of the wedge and are marked by few medium-amplitude and discontinuous reflections (Figs. 3.4a, 3.5a). In the upper part, the wedge shows an aggradation component marked by a series of sub-horizontal medium amplitude reflections. Arrangement of clinoforms edges displays a down-sloping geometry, with the toplap surface lying at depths between 65-70 m (Figs. 3.4a, 3.5a).

An aggrading fill (AF1), whose geometry is controlled by the underlying wedge, mantles the oldest PW1. AF1 is characterised by prevailing semi-transparent seismic facies with occasional thin and faint, low to moderate amplitude and continuous reflections (Figs. 3.4a, 3.4b, 3.4c and 3.5a). The thickness of AF1 between PW1 and PW2 reaches up to 10 m at the shelf edge, thinning on the slope formed by the youngest foresets, and increases again toward the basin (Fig. 3.4a, 3.5a).

The following wedge PW2 corresponds to the outer part of the shelf terrace off Pozzuoli and is followed along the whole shelf-break. It represents a compound wedge formed by two individual seismo-stratigraphic bodies, PW2a and PW2b (Figs. 3.4a-3.4d and 3.5a-3.5d). PW2a shows seismic facies characterised by alternating low-to-high amplitude, high-frequency continuous reflections (Figs. 3.4a to 3.4c and 3.5a). In the central and western sectors (Fig. 3.1), the upper part of PW2a is truncated by an abrasion surface (AS) that underlies the shelf terrace and geometrically merges with the toplap surface of younger PW2b clinoforms (Figs. 3.4a to 3.4c and 3.5a). Consequently, the topsets of PW2b are laterally contiguous with the basal part of PW2a foresets (Figs. 3.4a, 3.4b, 3.4c, 3.5a). In the western sector, the basal part (foresets to bottomsets transition) of PW2a is found at a depth of 20 m (Figs. 3.4a, 3.5a). Moving eastward offshore Pozzuoli, this depth increases from 35 to 42 m (Figs. 3.4b, 3.4c).

Unlike PW2a, younger PW2b is relatively well preserved everywhere at the shelf-break (Figs. 3.4a-3.4c, 3.5a and 3.5d). The seismic facies displays alternated semi-continuous and sub-transparent reflections (Fig. 3.4c). In the central sector (Rione Terra and La Starza lines, Fig. 3.1), PW2b shows a toplap surface that merges landward with the AS that truncates PW2a (Figs. 3.4a to 3.4c, 3.5b).

The depth distribution of PW2b edges is highly scattered. Offshore La Starza, the shelf edge of both oldest and youngest PW2b clinoforms lies at depths of 30 m (Figs. 3.4b, 3.5c), whereas offshore

Rione Terra, they are found at 40 m depth (Fig. 3.4c). In the eastern side of the bay offshore Bagnoli and Nisida, PW2b offlap breaks have a descending trajectory from 30 at the base to 34 m at the top (Fig. 3.4d, 3.5d). Along the western side, between Baia and Miseno, PW2b basal and top edges of clinoforms are at depths of 20 and 22 m, respectively (Fig. 3.4a).

An aggradation fill (AF2) develops above PW2 and covers the shelf of the Pozzuoli Bay with a maximum thickness of 15-20 m toward the coast. AF2 shows a prevailing transparent seismic facies, with few intercalated high-amplitude continuous reflections (Figs. 3.4a-3.4d, 3.5a-3.5d).

Three smaller prograding wedges (PW3, PW4, and PW5) are interbedded within the upper part of AF2, and they spatially coincide with the shallowest three terraces visible in bathymetry (Figs. 3.1 and 3.2a to c). In the central sector between Rione Terra and Accademia, the clinoform edges of the three bodies lie at water depths of 20 m, 13 m and 10 m, respectively (Fig. 3.4c). Between Rione Terra and Baia, the edges of the three wedges have shallower depths of 14 m, 12 m and 10 m, respectively (Fig. 3.4a). In the north-eastern sector, between Accademia and Bagnoli, the PW3 and PW4 shelf edge lies at a depth of 25 and 17 m, respectively. South of and including Bagnoli, PW4 is not observed in the seismic profiles because of lack of seismic coverage (Figs. 3.1 and 3.4d). Off Nisida, PW4 is neither observed in seismic images and bathymetry (Fig. 3.5d). In the western sector from Baia to Miseno offshore (Fig. 3.1), only the shallowest PW5 is imaged at 12 m (Figs. 3.4a and 3.5a). The younger PWs (PW3, PW4 and PW5) are characterized by a reduced lateral extension of about 50 m compared to the 500 m extension of PW2 and PW1. Furthermore, the observed clinoforms are poorly developed, with no evidence of high-amplitude and continuous seismic reflectors.

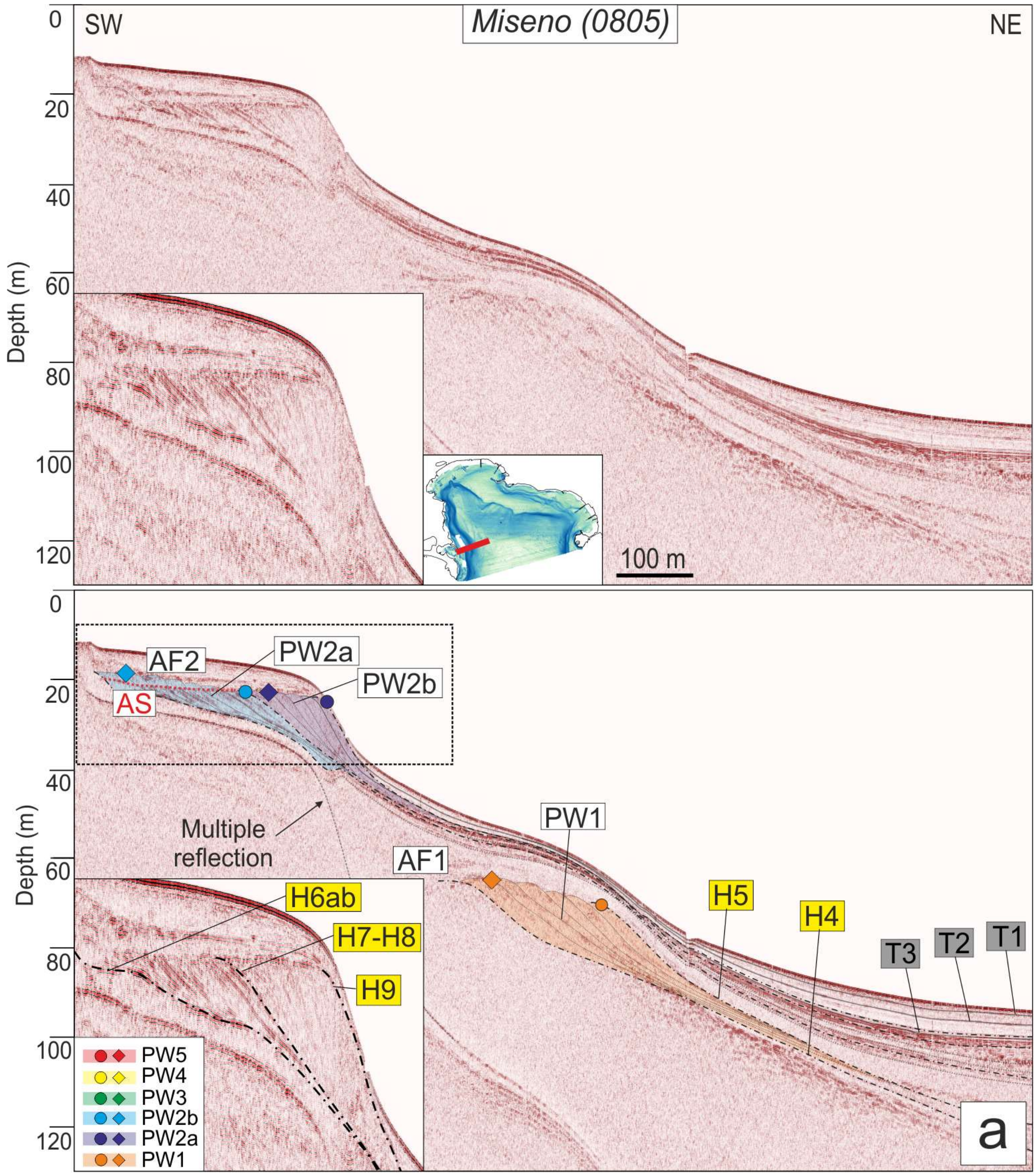

Figure 3.4 (a). Uninterpreted (top) and interpreted (bottom) seismic profiles (SEISTEC_0805) in the western sector of the Pozzuoli Bay. Coloured diamonds and dots are the oldest and youngest edges of individual PWs, respectively. Insets show zoomed view of PW2a and PW2b.

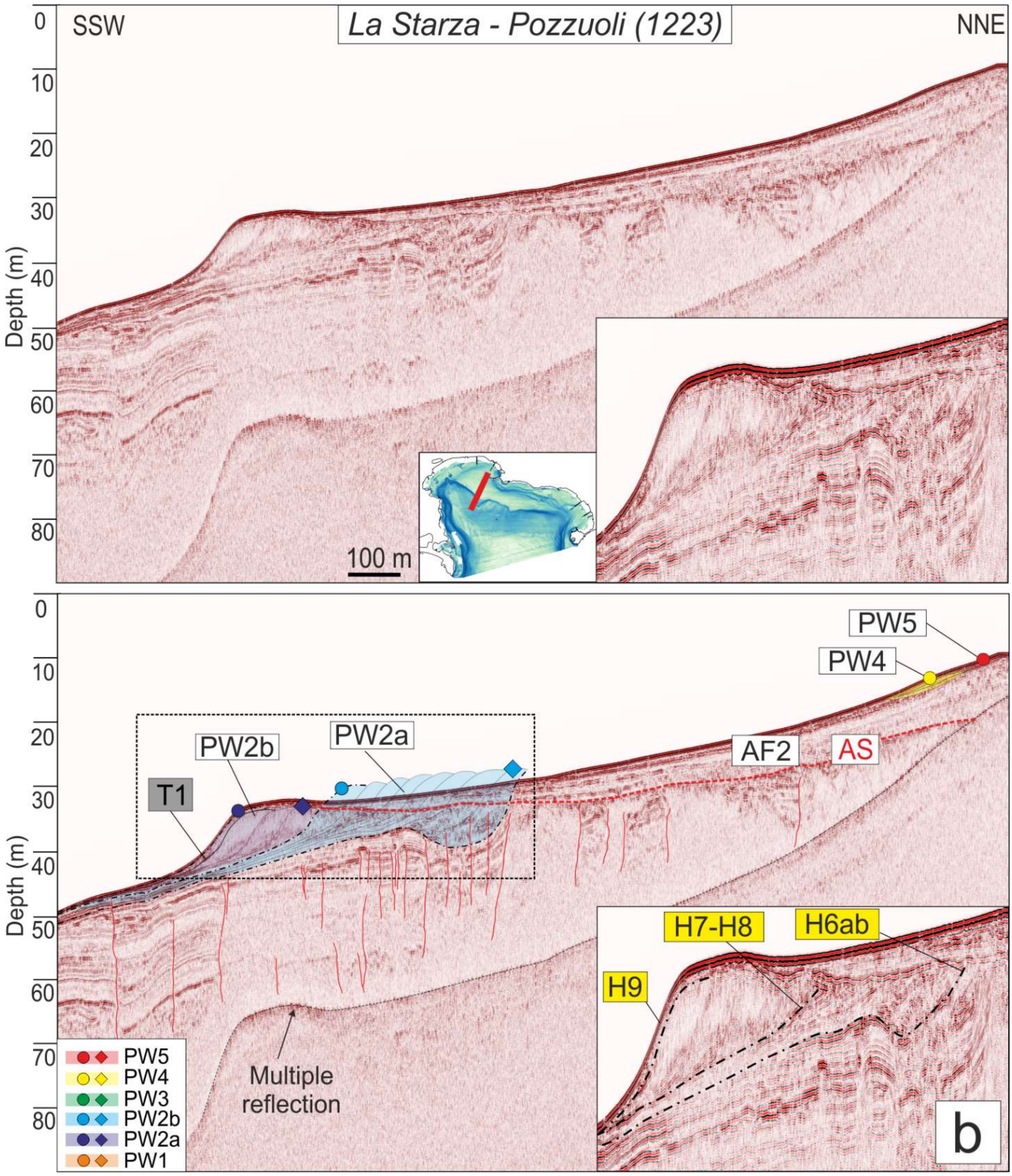

Figure 3.4 (b). Uninterpreted (top) and interpreted (bottom) seismic profile (SEISTEC_1223) in the central sector of the Pozzuoli Bay. Coloured diamonds and dots are the oldest and youngest edges of individual PWs, respectively. Insets show zoomed view of PW2a and PW2b.

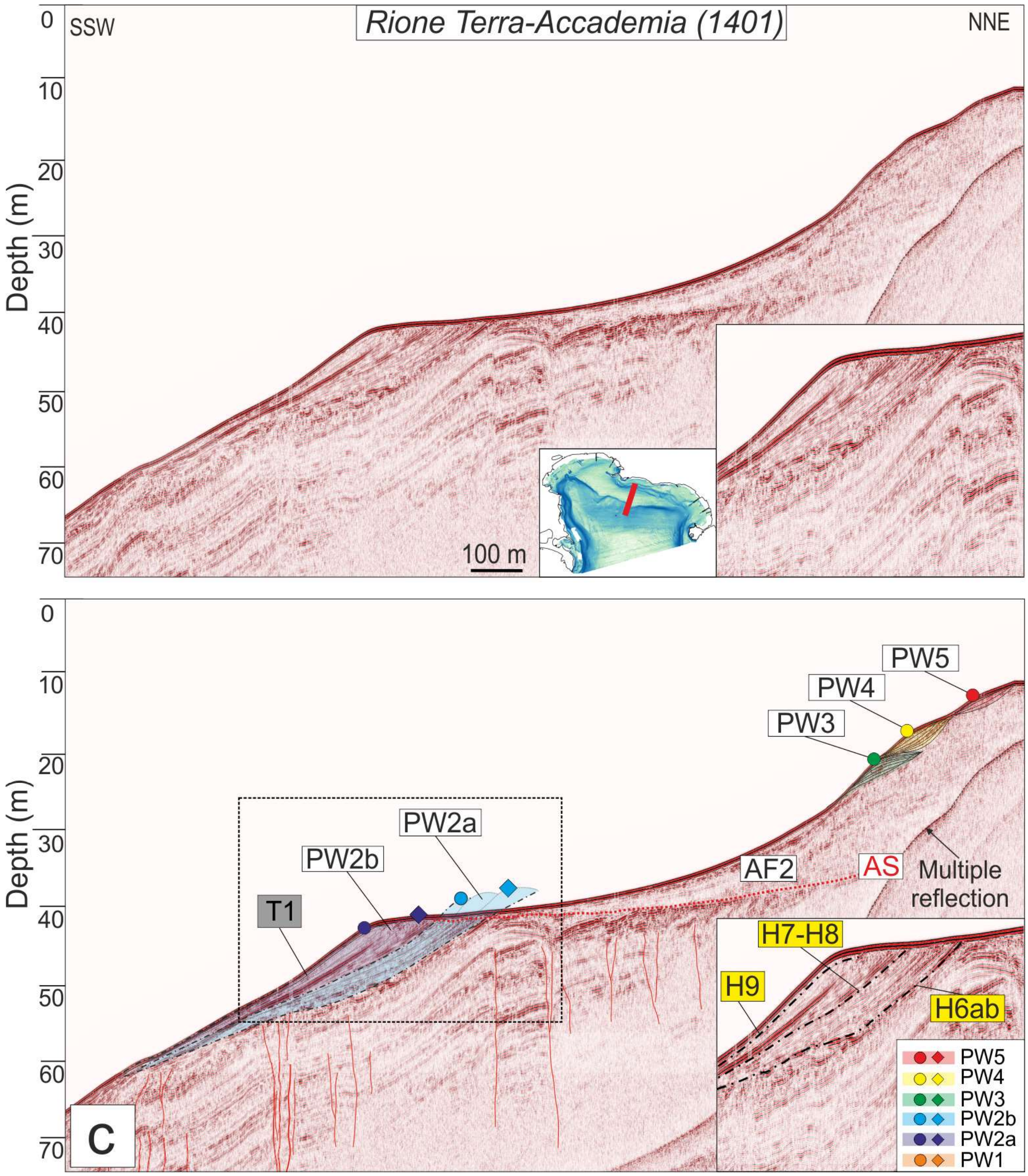

Figure 3.4 (c). Uninterpreted (top) and interpreted (bottom) seismic profiles (SEISTEC_1401) in the central sector of the Pozzuoli Bay. Coloured diamonds and dots are the oldest and youngest edges of individual PWs, respectively. Insets show zoomed view of PW2a and PW2b.

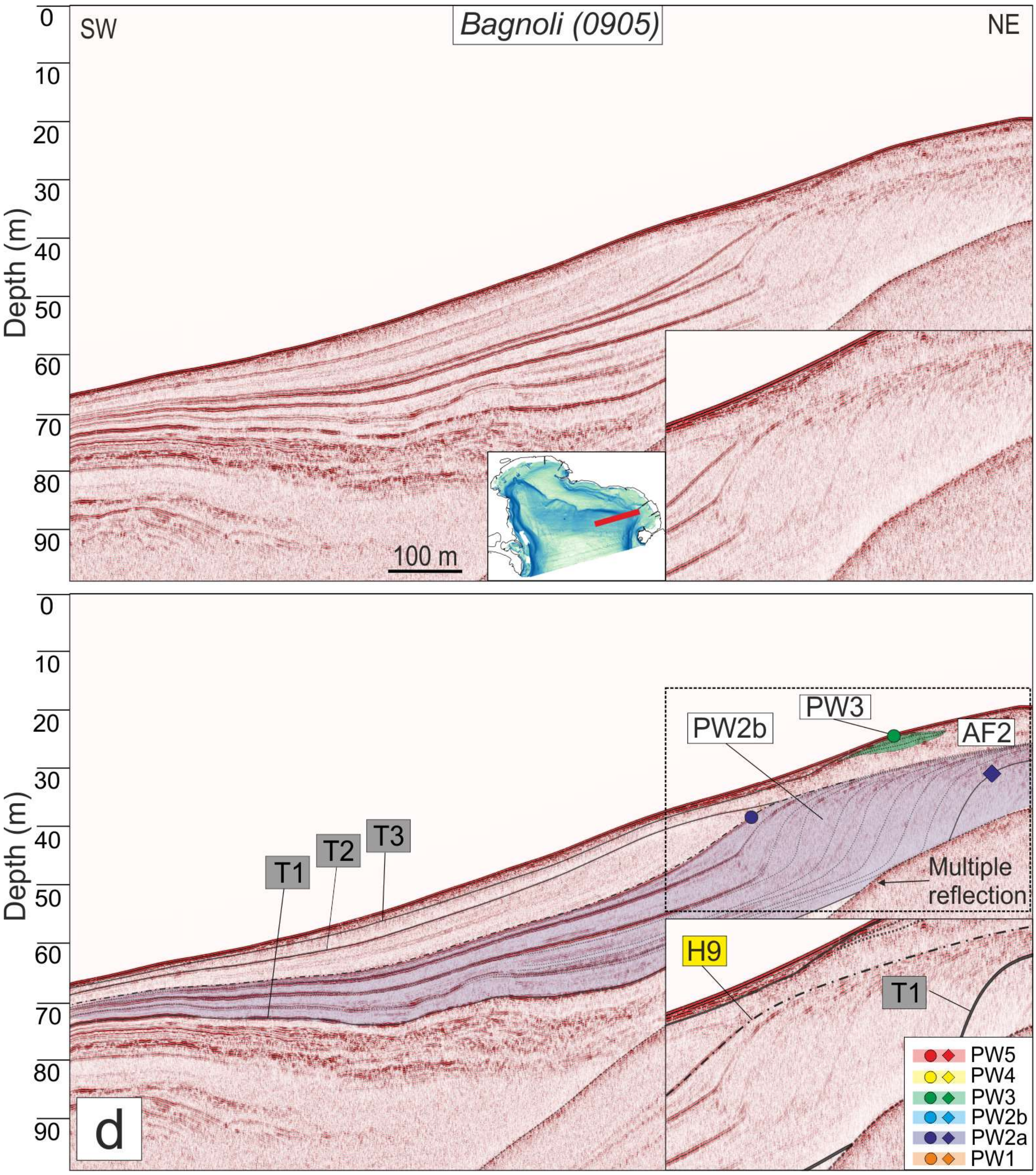

Figure 3.4 (d). Uninterpreted (top) and interpreted (bottom) seismic profiles (SEISTEC_0905) in the eastern sector of the Pozzuoli Bay. Coloured diamonds and dots are the oldest and youngest edges of individual PWs, respectively. Insets show zoomed view of PW2a and PW2b.

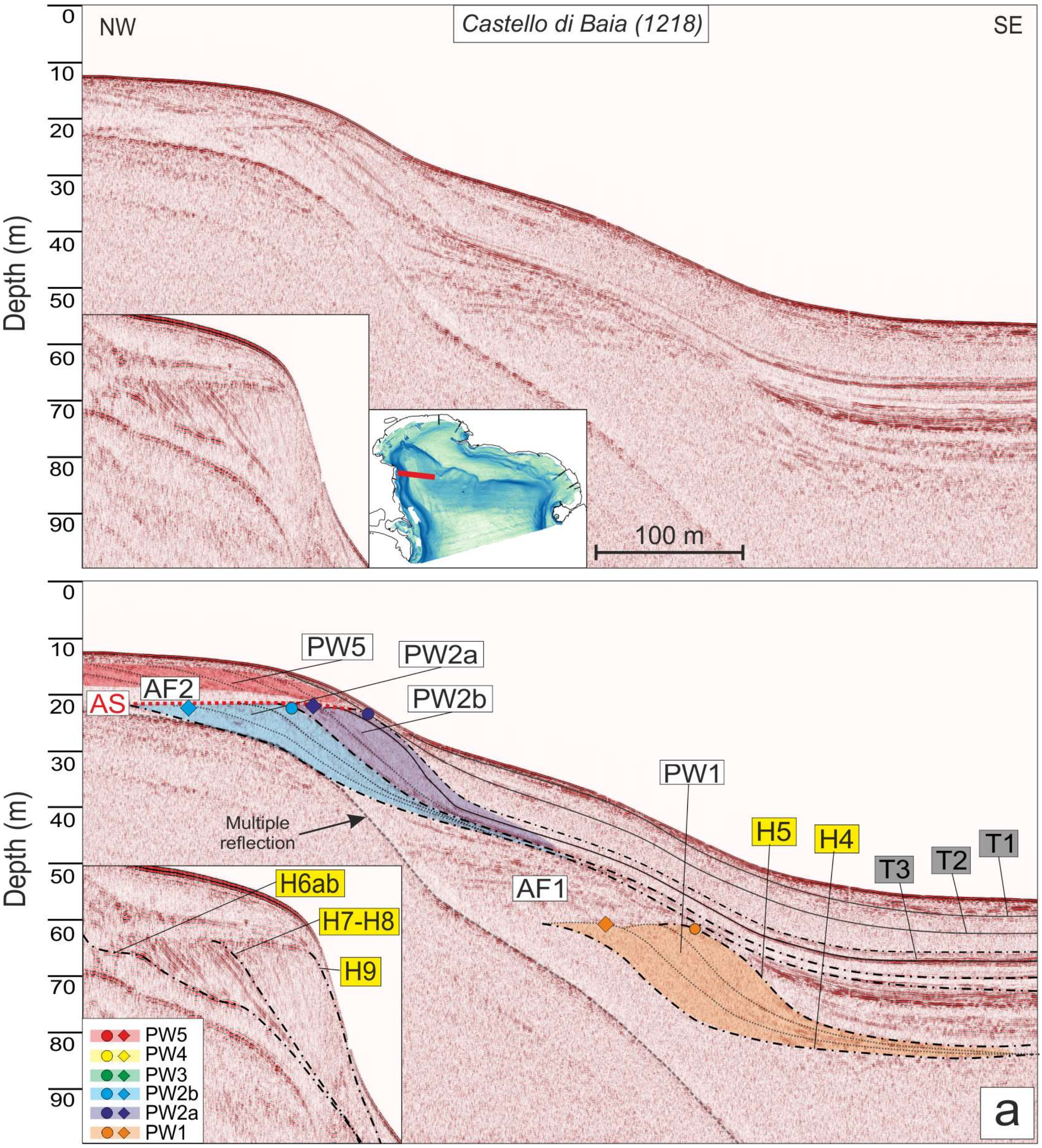

Figure 3.5 (a) Uninterpreted (top) and interpreted (bottom) seismic profile (SEISTEC_1218) in the western sector of the Pozzuoli Bay. Coloured diamonds and dots are the oldest and youngest edges of individual PWs, respectively. Insets show zoomed view of PW2a and PW2b.

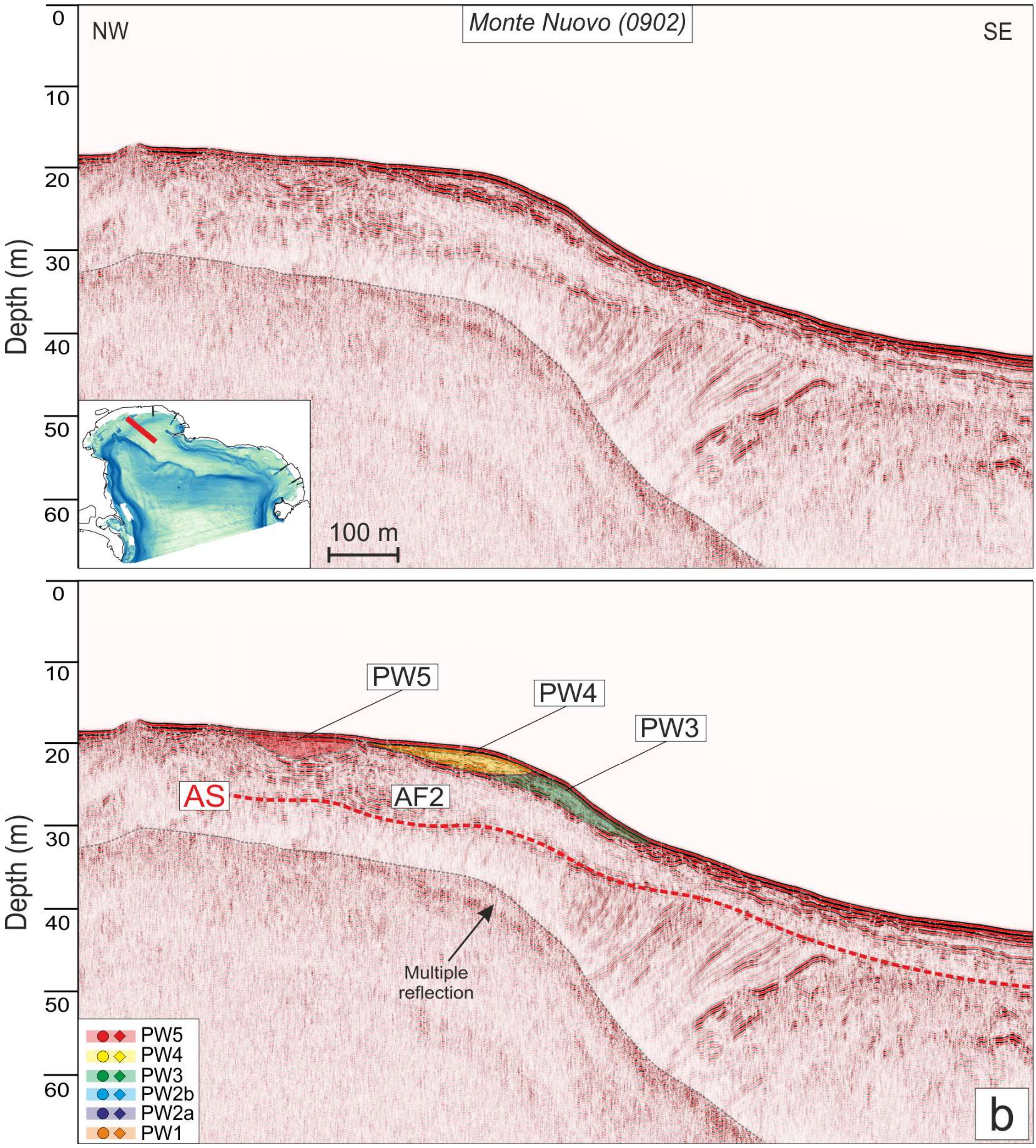

Figure 3.5 (b). Uninterpreted (top) and interpreted (bottom) seismic profiles (SEISTEC_0902) in the north-western sector of the Pozzuoli Bay. Coloured diamonds and dots are the oldest and youngest edges of individual PWs, respectively. Insets show zoomed view of PW2a and PW2b.

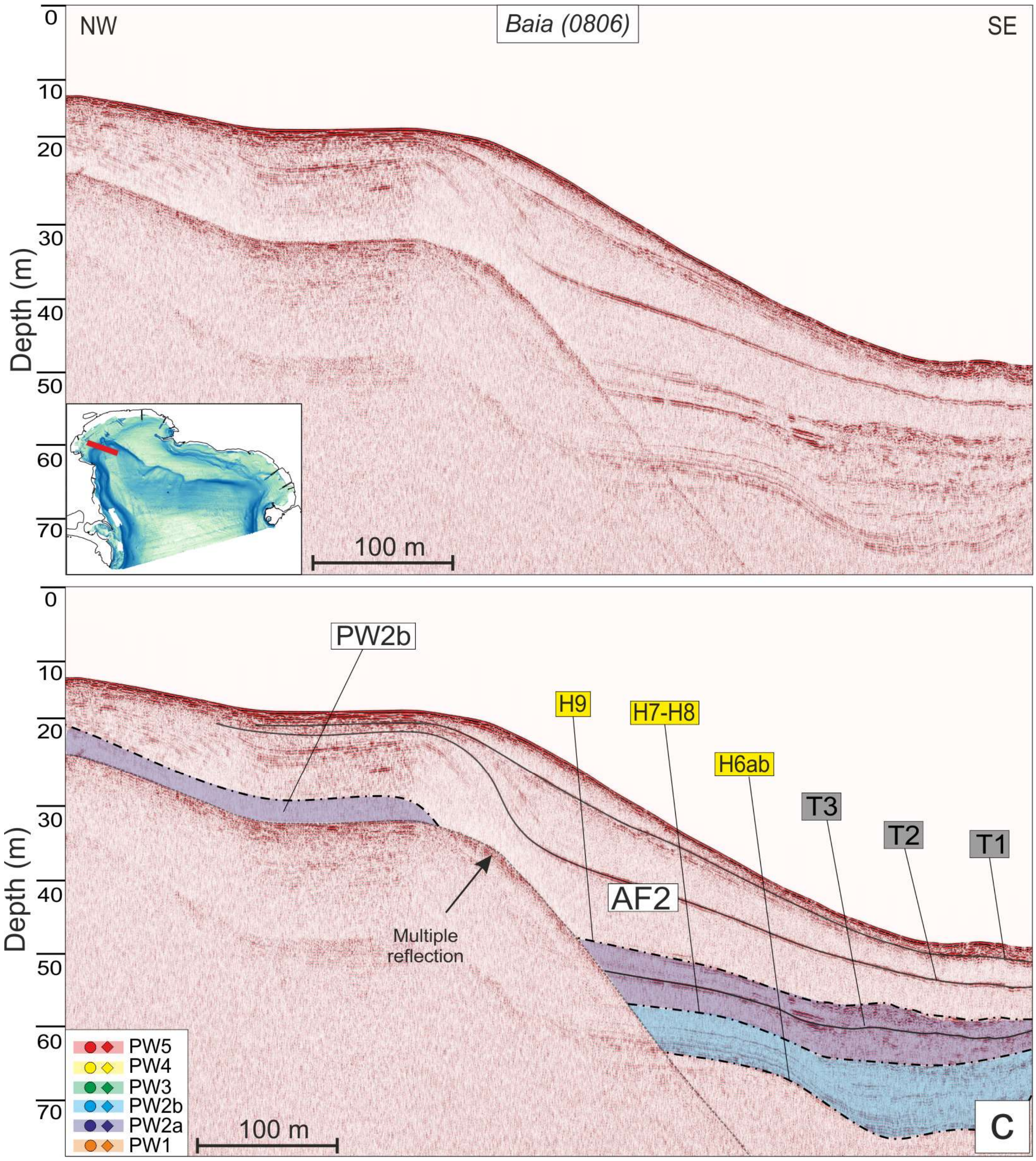

Figure 3.5 (c). Uninterpreted (top) and interpreted (bottom) seismic profile (SEISTEC_0806) in the north-western sector of the Pozzuoli Bay. Coloured diamonds and dots are the oldest and youngest edges of individual PWs, respectively. Insets show zoomed view of PW2a and PW2b.

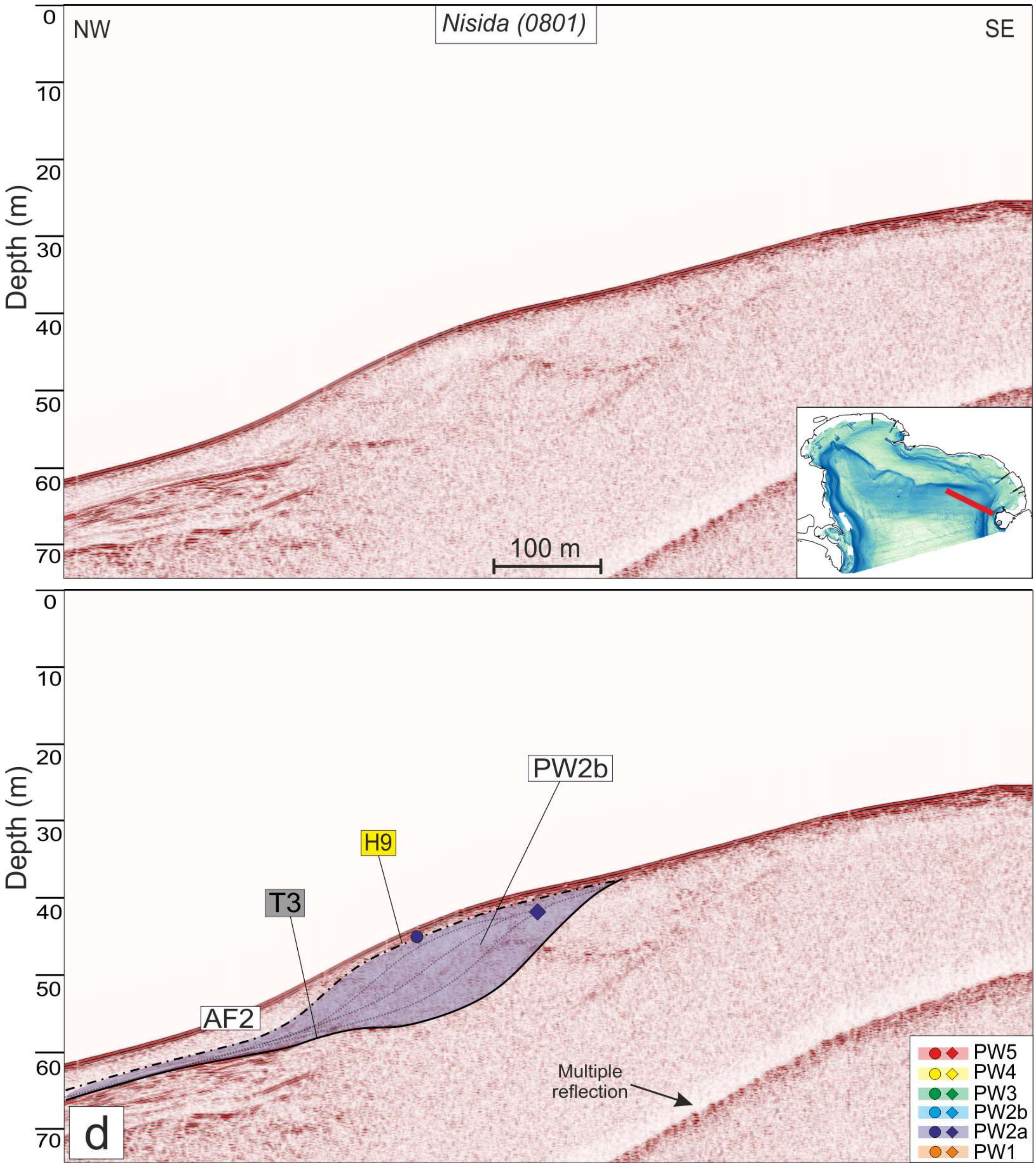

Figure 3.5 (d). Uninterpreted (top) and interpreted (bottom) seismic profile (SEISTEC_0801) in the south-eastern sector of the Pozzuoli Bay. Coloured diamonds and dots are the oldest and youngest edges of individual PWs, respectively. Insets show zoomed view of PW2a and PW2b.

3.2.2 The Posillipo-Miseno offshore

In the most peripheral sectors of Pozzuoli Bay and offshore the bay, corresponding to the southern part of the ring fault zone (Fig. 1.4), the seismic profile analysis has led to identifying four generations of prograding wedges, from PW-X1 to PW-X4 (Figs., 3.6 and 3.7) (Table S1). These wedges are associated with as many depositional terraces as evidenced by the morpho-bathymetric analysis (Fig. 3.3).

The deepest wedge (PW-X1) has been observed in the most southern sector of the bay, limited at the lower boundary from the Canyon Dohrn (Figs. 3.1, 3.7a, c, d). The clinoforms are well developed and marked by few medium to high-amplitude and discontinuous reflections (Figs. 3.7a, c, d). In the upper part of the wedge, a marked abrasion surface is present and is characterized by continuous and sub-parallel high-amplitude reflections. Arrangement of clinoforms edges displays a down-sloping geometry, with the toplap surface lying at depths between 150-160 m (Fig. 3.7a, c, d). There is limited evidence of aggrading fills after the development of PW-X1 because of the distal location compared to the Pozzuoli Bay. The following wedge PW-X2 is observed only in the south-eastern flank of the Penta Palummo Banks, corresponds to its outer part of the shelf terrace (Fig. 3.1). PW-X2 shows seismic facies characterised by medium amplitude and high-frequency reflections (Figs. 3.7a, d) to discontinuous and chaotic facies (Fig. 3.7c). This wedge lies at a depth of 110-115 m.

Shallower PW-X3 is well developed in the external part of the Pozzuoli Bay. It extends in the Posillipo Hill offshore, in the shelf-break of Nisida Bank, in the north-eastern deepest flank of Penta Palummo Banks and in the south-eastern part of Miseno Banks (Fig. 3.1). PW-X3 is characterized by continuous and sub-parallel high-amplitude reflections (Fig. 3.7a to 3.7d). In Figures 3.6b and 3.6c, the internal reflections are not clearly visible because of the low signal penetration, but the wedge shape is still evident. The edge of PW-X3 lies to a depth of about 90-100 m.

The shallower wedge observed in the external part of the Pozzuoli Bay is PW-X4. This wedge is characterized by a seismic facies with discontinuous and medium-amplitude reflectors (Fig. 3.6d, 3.7a, 3.7c). The wedge has an evident morpho-bathymetric expression and is recognized off to Posillipo, in the Procida channel and around the Miseno banks. Moreover, it is weakly evident with an irregular shape in the Penta Palummo Banks (Fig. 3.1). PW-X4 edge lies at a depth of 70-80 m (Figs. 3.6 a, c., 3.7d).

The presence of prograding wedges has also been observed offshore the southeast part of Ischia Island. Figure 3.8 shows a well-developed prograding wedge around the submerged Ischia Bank, and its shelf-edge lies at a depth of 60 m, just below a large abrasion surface found at 35 m below the sea level (Fig. 3.8).

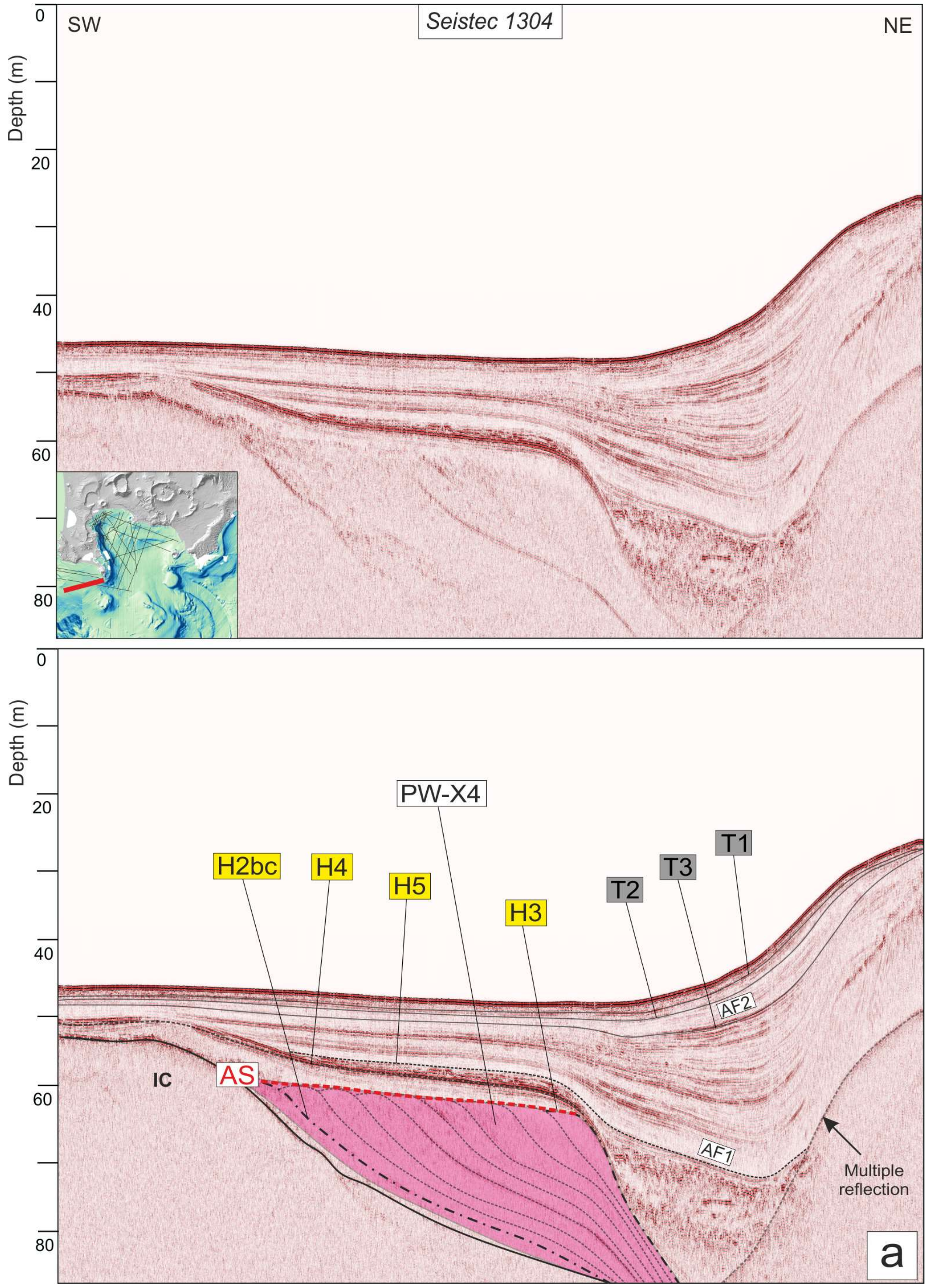

Figure 3.6 (a). Uninterpreted (top) and interpreted (bottom) seismic profile (SEISTEC_1304) in the external sectors of the NYT caldera in the Pozzuoli Bay.

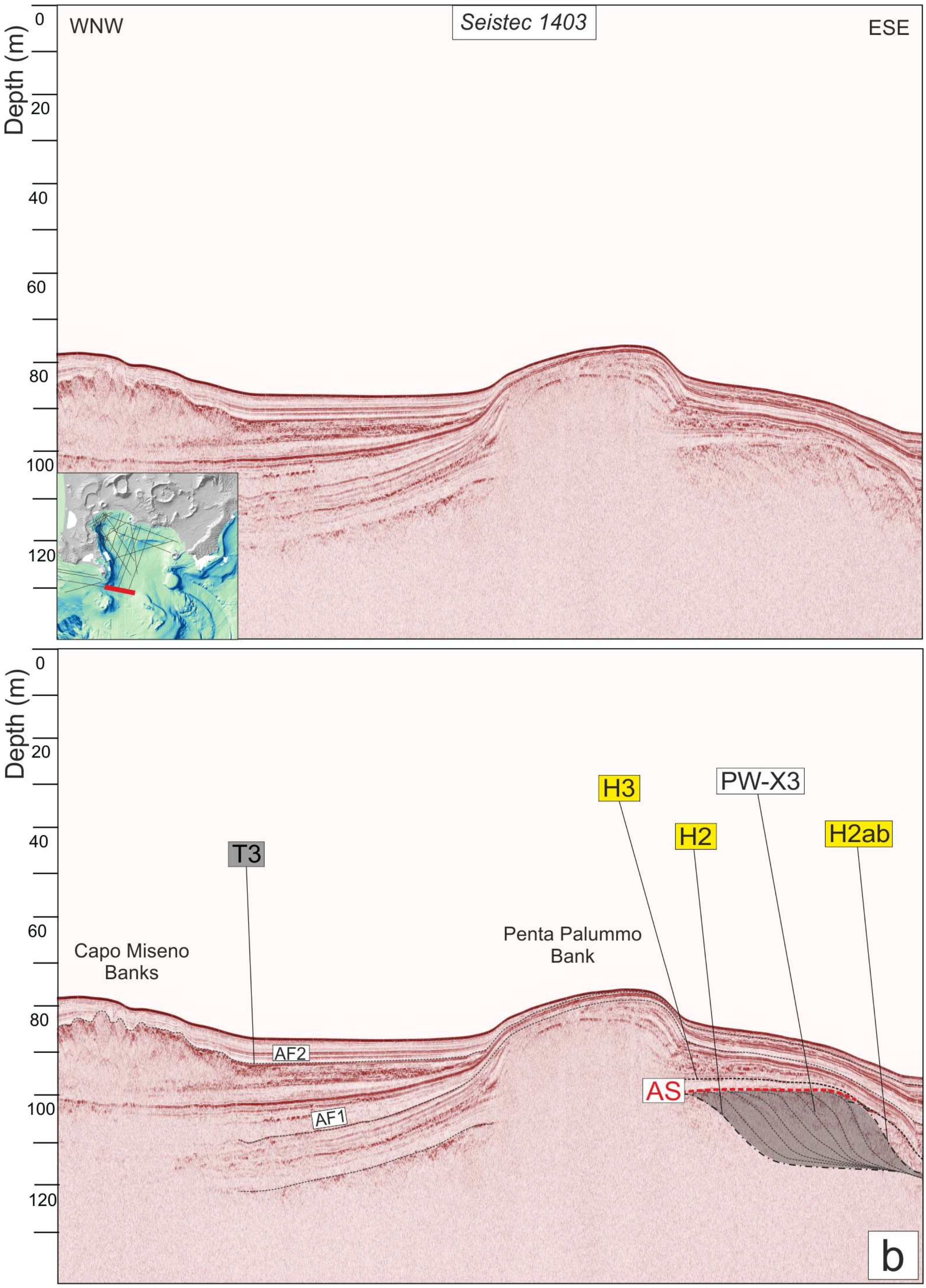

Figure 3.6 (b). Uninterpreted (top) and interpreted (bottom) seismic profile (SEISTEC_1403) in the external sectors of the NYT caldera in the Pozzuoli Bay.

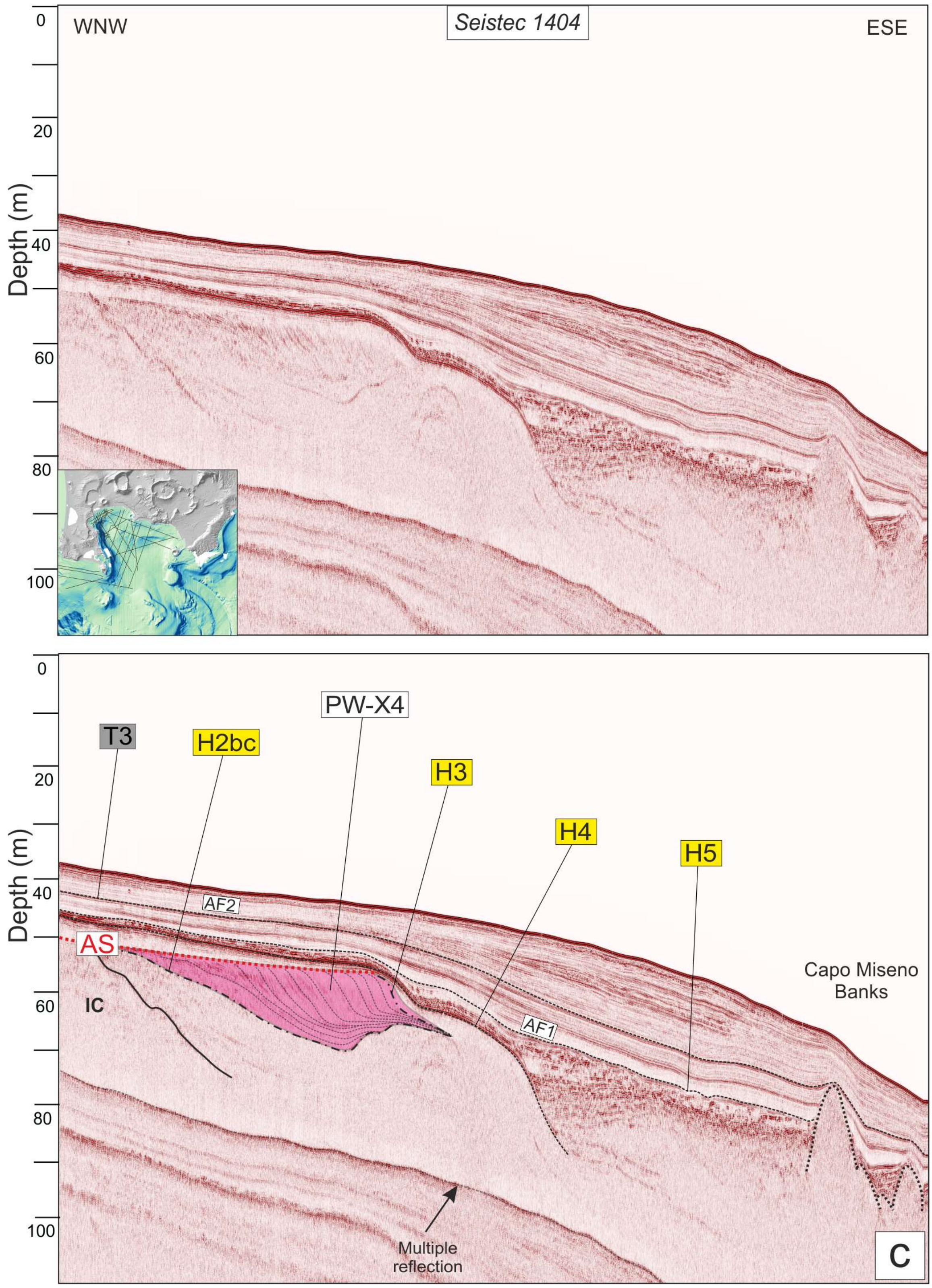

Figure 3.6 (c). Uninterpreted (top) and interpreted (bottom) seismic profile (SEISTEC_1404) in the external sectors of the NYT caldera in the Pozzuoli Bay.

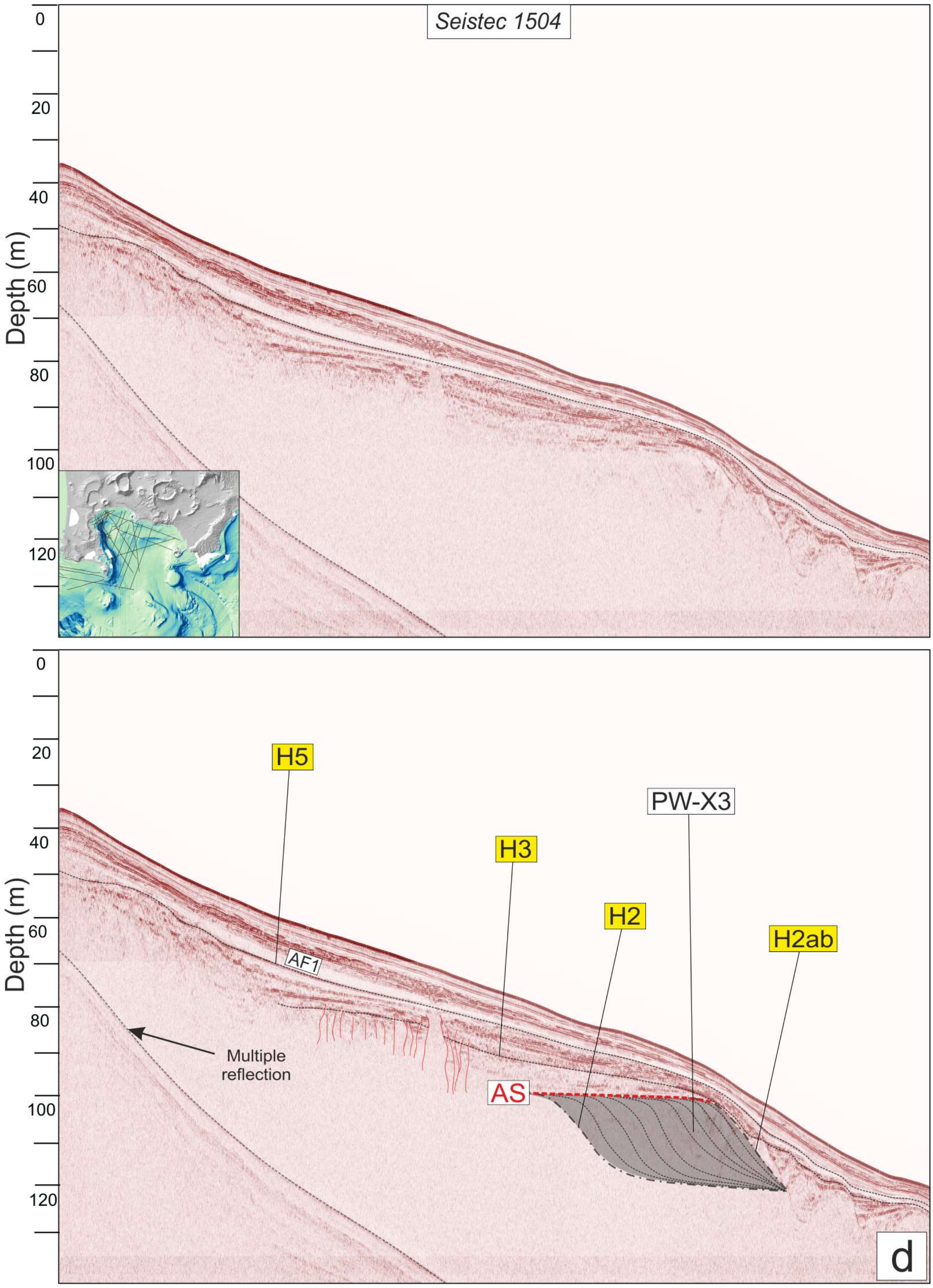

Figure 3.6 (d). Uninterpreted (top) and interpreted (bottom) seismic profile (SEISTEC_1504) in the external sectors of the NYT caldera in the Pozzuoli Bay.

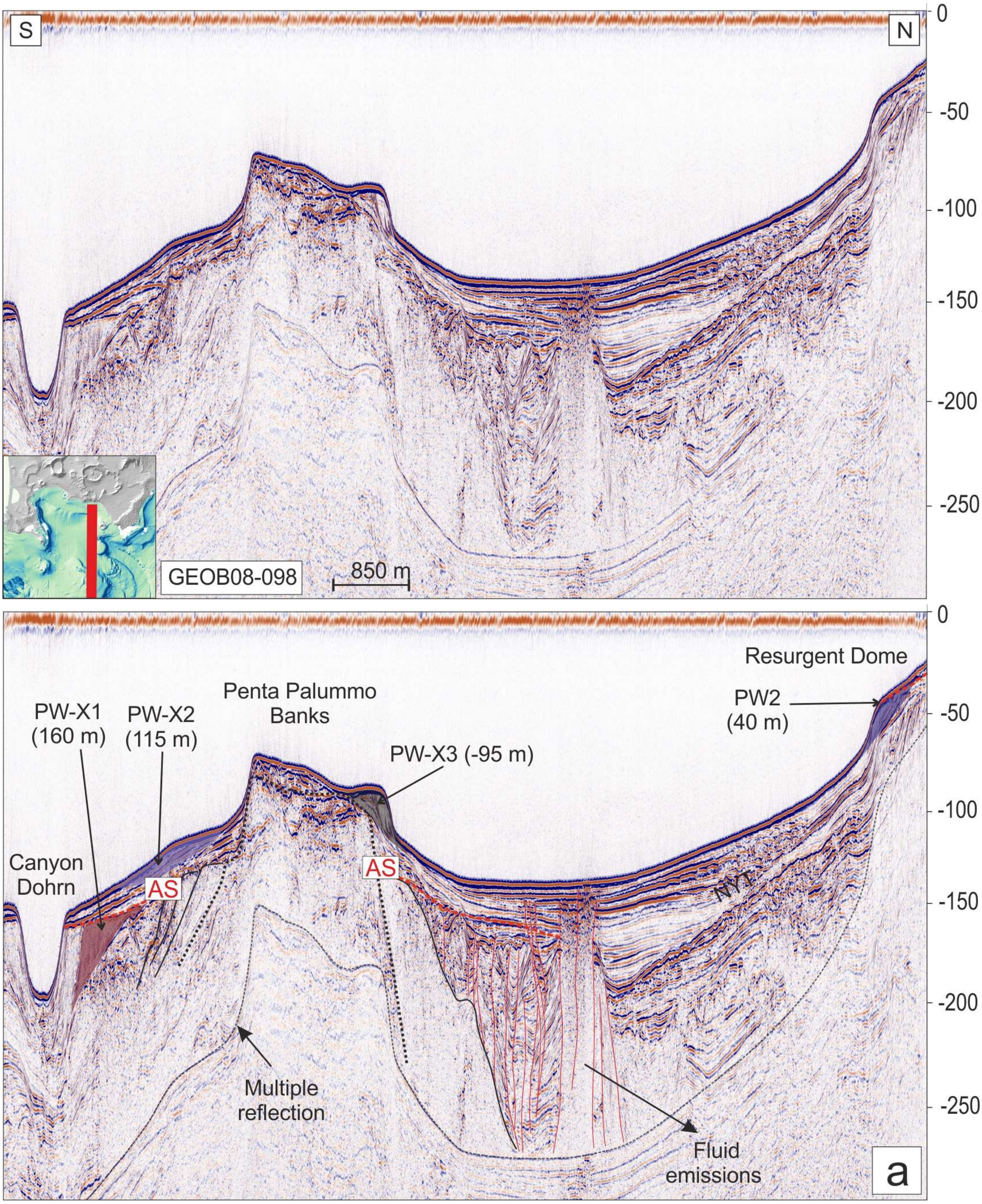

Figure 3.7 (a). Uninterpreted (top) and interpreted (bottom) seismic profile (CAFE_098) oriented N-S and located in the southern east part of Penta Palummo banks in the external sectors of the NYT caldera in the Pozzuoli Bay.

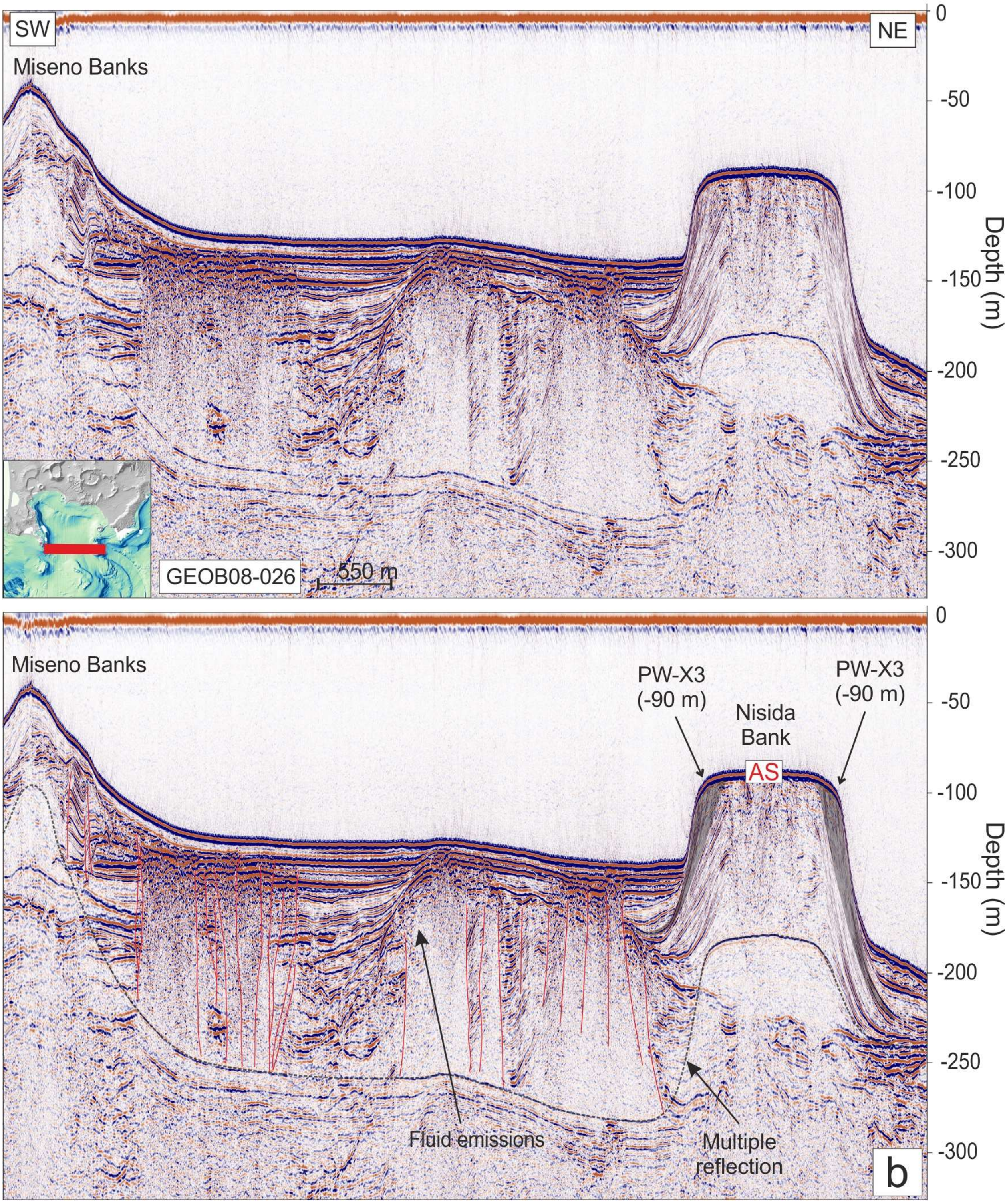

Figure 3.7 (b). Uninterpreted (top) and interpreted (bottom) seismic profile (CAFE_026) oriented E-W and crosses the Nisida bank until the Miseno banks located in the external sectors of the NYT caldera in the Pozzuoli Bay

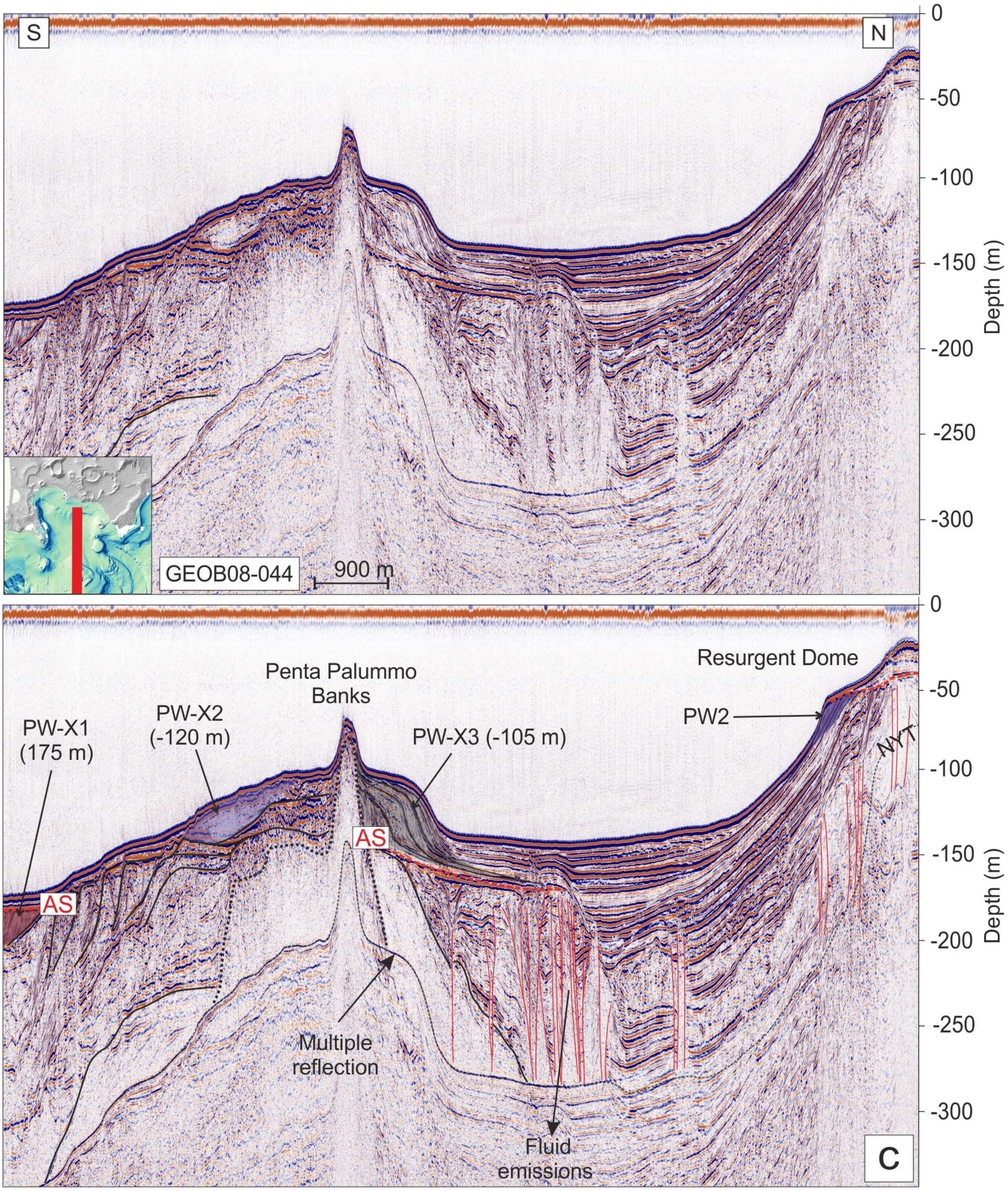

Figure 3.7 (c). Uninterpreted (top) and interpreted (bottom) seismic profile (CAFE_044) oriented N-S and located in the southern east part of Penta Palummo banks, in the external sectors of the NYT caldera in the Pozzuoli Bay.

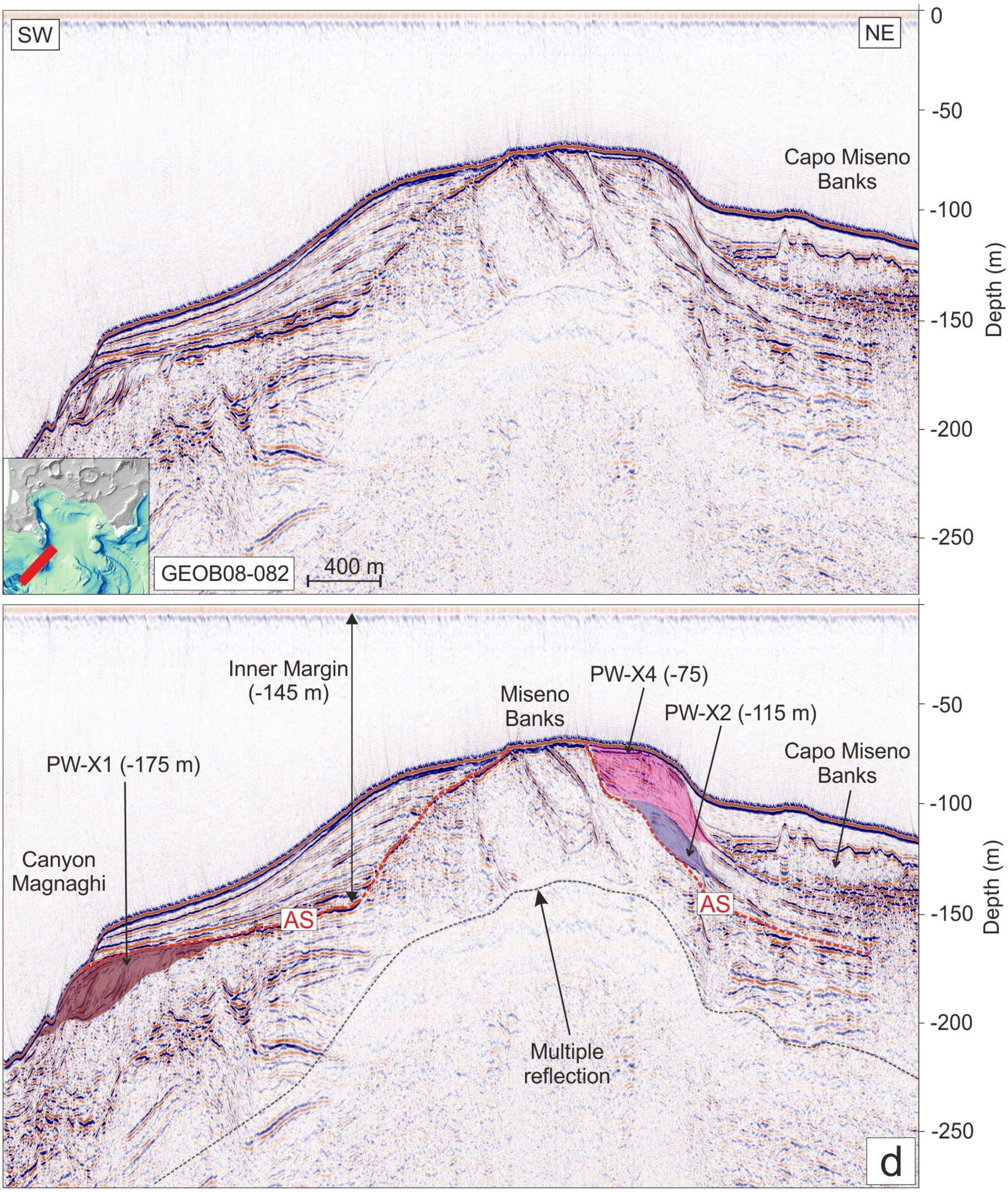

Figure 3.7 (d). Uninterpreted (top) and interpreted (bottom) seismic profile (CAFE_082) NE-SW oriented line located in the south-west in correspondence of the Miseno and Capo Miseno banks in the external sectors of the NYT caldera in the Pozzuoli Bay.

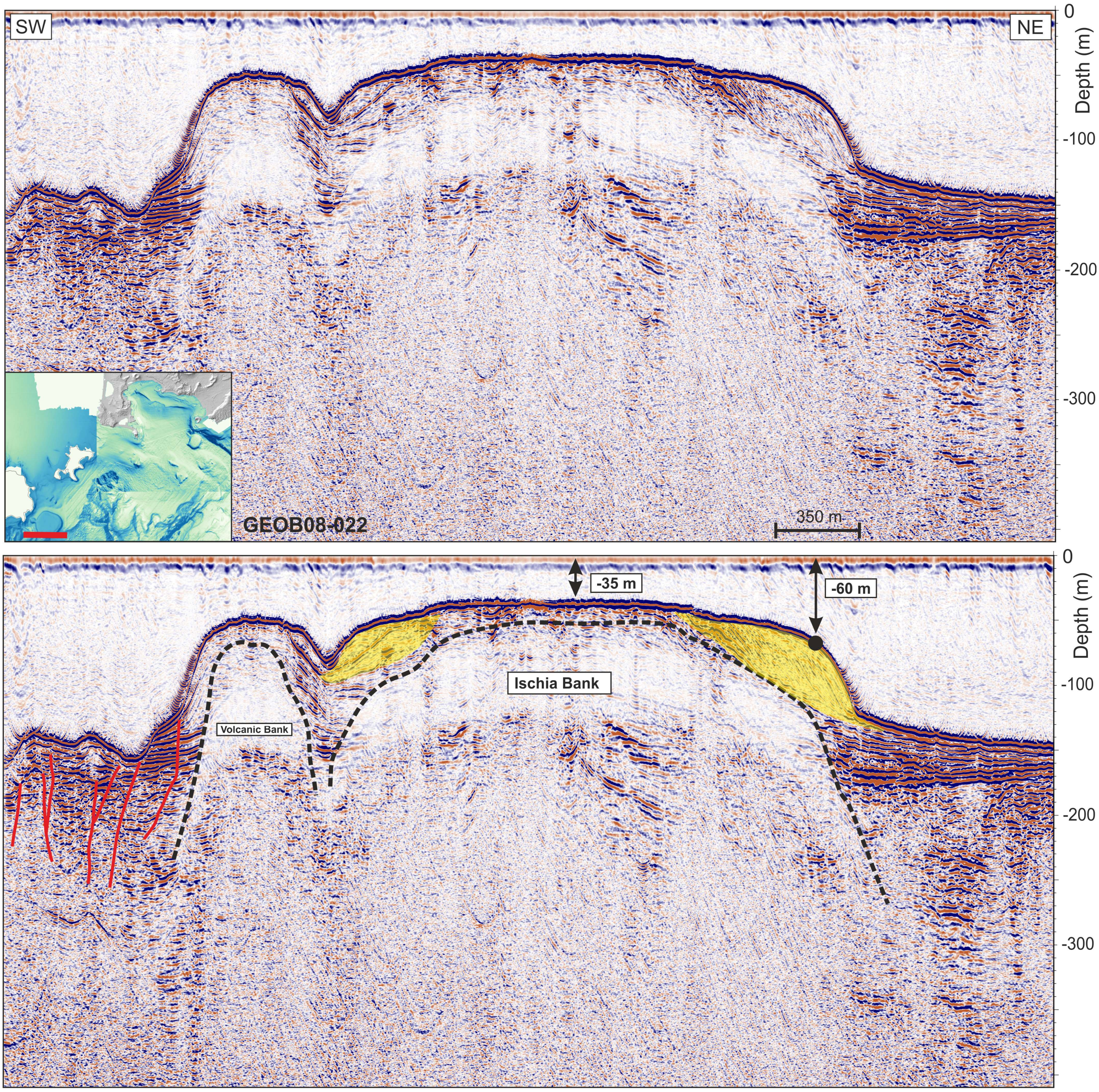

Figure 3.8. Uninterpreted (top) and interpreted (bottom) CAFE seismic profiles in the external sectors of Ischia island.

3.3. Inferred age for RSL indicators

3.3.1 Chronostratigraphy in the Pozzuoli Bay

The ages assigned to the RSL indicators described above rely on the correlation with the chronostratigraphy proposed by Natale et al. (2021). In this study, the seismic sequences identified in the Pozzuoli Bay are correlated with the depositional units and unconformities recognised and dated in the La Starza succession by Isaia et al. (2019) (Tables S1; Figs. 3.9). The seismic horizons used in the present study for correlating the shelf indicators with indirectly dated horizons in the basin fill are labelled following the terminology of Natale et al. (2021).

The base of PW1 is traced in the lower part of a semi-transparent package resting above a series of medium to high-amplitude, semi-continuous reflectors (Figs. 3.4a, 3.5a) and can be correlated with seismic horizon H4 (Fig. 3.9a). In the La Starza succession, this horizon is found in the uppermost part of a foreshore-shoreface depositional unit dated at ~9.6 ka, which provides a constraint for the onset of PW1. The top of PW1 is represented by a high-amplitude and continuous reflector that, towards the basin, forms the base of a package of mid-to low-amplitude reflections (horizon H5; Figs. 3.9a, 3.4a, 3.5a). This package is correlated in the La Starza succession with the end of Epoch 2 and was followed by marine deposits whose base is dated at ~9.1 ka (Isaia et al., 2019), and thus provide the age for the demise of PW1.

The aggrading fill AF1 that overlies PW1 on the shelf is largely formed by a transparent seismic facies (Figs. 3.9a, 3.4a, 3.5a), interpreted as a predominant siliciclastic marine succession without a significant volcaniclastic contribution (Natale et al., 2020). The transparent seismic facies is followed by mid-amplitude parallel and continuous reflections, whose base is identified as H5ab (Figs. 3.9a, 3.4a, 3.5a). According to Natale et al. (2021), this change in seismic facies indicates the maximum water depth attained during the development of AF1 that lasted until ~5.9 ka (Fig. 3.9a).

AF1 is overlain by compound wedge PW2, which includes two separate bodies, PW2a and PW2b. The base of PW2a is not easily recognised in the resurgent central sector, where the lower section of the wedge includes chaotic facies indicative of slumping. Notwithstanding, PW2a develops above reflector H6ab (Fig. 3.4b), which in the basin ends the seismic sequence with mid-amplitude continuous reflectors and is dated at ~5.2 ka (Fig. 3.9a).

Reflectors between H7 and H8 limit a transparent seismic facies that testify to prevailing marine deposition (Fig. 3.9a). Onland, this seismic facies may be correlated to the deposition of a paralic-foreshore deposit known as “Pozzuoli Unit”, dated between ~4.5-4.4 ka (Isaia et al., 2019). The Pozzuoli Unit's deposition ends with a short uplift phase started at ~4.4 ka (Fig. 3.9a). This uplift caused the development of an abrasion surface between ~4.4 ka and ~4.2 ka, associated with an erosive truncation in the La Starza succession and included between reflectors H8 and H8bc (Fig.

3.9a). This uplift phase caused the erosion of the upper part of PW2a on the shelf, particularly at the resurgent dome (Figs. 3.4b).

Overlying PW2b formed soon after uplift that redistributed the material shed by erosion of PW2a. A series of very high-amplitude, medium-frequency, continuous reflectors are traced from the basin to the upper part of PW2b (Figs. 3.4b, 3.4c). The upper part of these high-amplitude reflections includes the deepest tephra (T1) found in gravity cores in the basin (Fig. 3.4a to b, 3.5a to b), which is dated to ~3.9 ka (Sacchi et al., 2014). In the eastern sector, between Bagnoli and Nisida, tephra T1 is not included in the upper part; instead, it is found in the lowest visible part of PW2b (Fig. 3.4d). The medium-amplitude reflector (H9) that tops this sequence is traced upslope toward the shelf and forms the youngest clinoforms within PW2b (Figs. 3.4a to 3.4d, 3.5a, 3.5c, 3.5d). Reflector H9 has an estimated age of ~3.7 ka. It is correlated to the last known eruption in the southern coastal sector of the caldera of Epoch 3b (Sacchi et al., 2014; Natale et al., 2021) (Fig. 3.9a).

The aggrading fill AF2, which underlies the modern shelf, developed after ~3.7 ka. This aggradation is interrupted by three minor progradation events (PW3, PW4, PW5). Detailed constraints on the age of these shallower wedges are not available because of the difficulty of tracing the horizons calibrated by gravity cores (Fig. 3.9a) above the abrasion surface that forms the base of the shelf. Based on the model illustrated in the method sections and detailed in a later section, the ages for these seismic bodies were estimated based on historical RSL falls and thus uplift events documented onland.

Based on archaeological data, Aucelli et al. (2021) suggested the existence of a short-lived uplift that affected various sectors of the Pozzuoli Bay at ~2.1 ka, followed by stability until ~1.9. The ~2.1-1.9 ka (100 BCE-100 CE) stability is associated with the development of PW3 (Fig. 3.9a). A second stability moment, long-established by *lithophaga* borings in the *Serapeum* columns and elsewhere at Pozzuoli (Bellucci et al., 2006; Mohrange et al., 2006), led to the formation of PW4 at ~1.4-1.2 ka (600-700 CE). Finally, a link between the development of PW5 and the M. Nuovo unrest is proposed. Specifically, PW5 formed in a stability moment after the documented uplift phase occurred at 1430-1536 CE that preceded the 1538 CE eruption (Di Vito et al., 2016). Considering the short time between the very fast and variable deformation phases that alternated in the last 2 ka, PW3, PW4 and PW5 may have partially also formed during the uplift phases. This is reasonable in terms of magnitude compared with the reduced size of these wedges and their poor development.

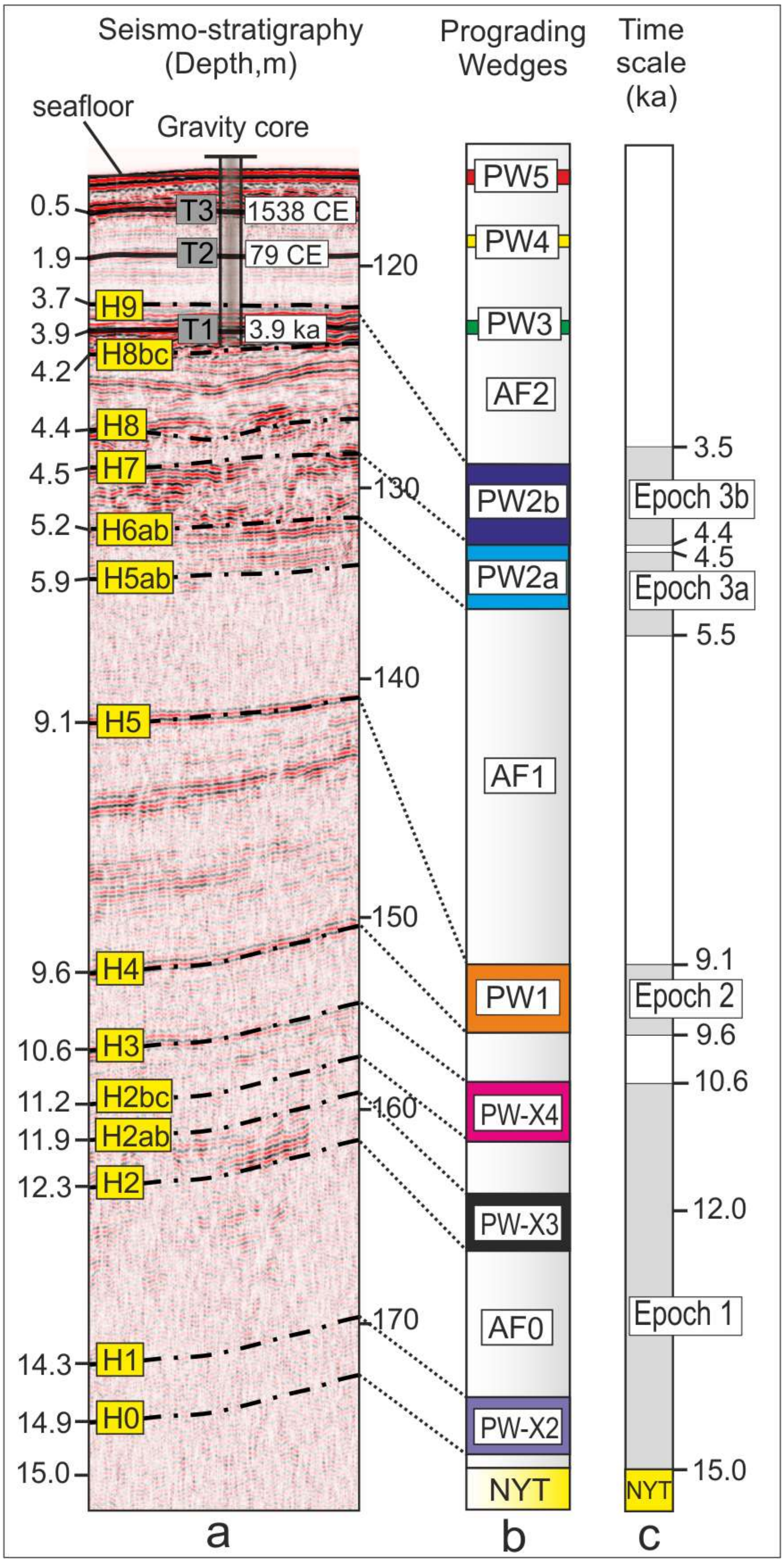

Figure 3.9. a) Seismo-stratigraphic frame of the post-NYT caldera fill, showing key reflectors. The shallower reflectors T1 to T3 (solid black lines) have been calibrated with gravity cores (after Sacchi et al., 2014). The deeper reflectors (dashed and dotted lines) are labelled after Natale et al. (submitted). b) Chronological position of seismo-stratigraphic bodies. c) Volcanic epochs (after Smith et al., 2011).

3.3.2 Chronostratigraphy in the Posillipo-Miseno offshore

The seismic horizons used to correlate the seismo-stratigraphical indicators found outside the NYT caldera are derived from the seismic age attribution of Natale et al. (2021) and Steinmann et al., 2018 (Table S1; Fig. 3.9a).

The base and the top of PW-X1 have been dated using the seismic age attribution of Steinmann et al. (2018), who assigned an age of 18 ka, related to the end of the LGM, to the abrasion surface that developed above it. Thus, the formation of PW-X1 can be attributed to the period between 18.5 and 18 ka, corresponding to the final phase of the LGM when the lowstand had reached its maximum development. The abrasion surface that overlies PW-X1 on the shelf is largely formed by very high-amplitude seismic reflectors (Figs. 3.7a, c, d) (Steinmann et al., 2016).

The base of PW-X2 is traced in the lower part of a semi-transparent package corresponding to a high-amplitude to chaotic reflectors correlated with seismic horizon H0 (Figs. 1.16d, 3.9a, 3.7a, c, d). According to Natale et al. (2021), this horizon corresponds almost to the top of NYT and is dated at ~14.9 ka, which provides a constraint for the onset of PW-X2.

The top of PW-X2 is represented by a high-amplitude and continuous reflector that forms the base of a package of mid-to low-amplitude reflections (horizon H1; Figs. 3.9a, 3.7a, c, d). This seismic horizon is dated at 14.3 ka and thus provide the age for the demise of PW-X2.

The base of PW-X3 corresponds to the lowermost of a continuous, high-amplitude reflectors package (horizon H2), dated at 12.3 ka (Fig. 3.9a). The top of PW-X3 is traced at the end of this package of continuous reflectors and is labelled as horizon H2ab, dated at 11.9 ka. Reflectors H2ab and overlying H2bc limit a transparent seismic facies that testifies to prevailing marine deposition in a short time between PW-X3 and PW-X4 (Fig. 3.9a).

The base of PW-X4 coincides with the end of this transparent facies and the appearance of medium to low-amplitude reflectors. The base of these reflectors is correlated with horizon H2bc, dated at 11.2 ka. The top of PW-X4 coincides with horizon H3 that closes this sequence of medium-amplitude seismic reflectors, and is dated at 10.6 ka.

3.4 Location, depth distribution and ages of archaeological RSL indicators

The archaeological indicators considered here are distributed along the coastal belt of Campi Flegrei and have an inferred age of ∼2.1 to ∼1.8 ka BP (I BCE-II CE) (Table S2; Fig. 2.6, 3.10). Figure 3.10 shows their depth distribution between -2 and -5 m, with the depth already corrected for the functional height. Thus, Fig. 3.10 highlights the distribution and depth of Roman-age relative sea levels.

East of the CF caldera, a buried pier (R1) from the ancient Naples harbour defines an RSL at -2.4 m (Vacchi et al., 2019) (Fig. 2.7a). Moving westward, from Naples to Nisida Island, the RSL from archaeological markers smoothly increases from -2.7 to -3.3 m. In detail, the RSL from fish tanks R2 (Pappone et al., 2019) (Fig. 2.7b), R3 (Aucelli et al., 2019) (Fig. 2.7c) in Naples City, and site 1 (Fig. 2.8c) along the Posillipo coast lie at depths of -2.7, -3.1 and -3.2 m, respectively.

Within the CF caldera, Roman pier R4 south-east of Nisida Island defines an RSL at -3.3 m (Aucelli et al., 2019) (Fig. 2.7d). In the resurgent dome sector, the *Serapeum* marble floor R5 close to Rione Terra yields an RSL position at -3.1 m (Bellucci et al., 2006) (Fig. 2.7e). Roman pier R6 off to Rione Terra provides a deeper RSL at -3.7 m (Aucelli et al., 2018) (Fig. 2.7f). Moving westward from Rione Terra to Baia, an RSL depth increase of about 1 meter (from -3.1 to -4.2 m) is observed. Markers off to Monte Nuovo, represented by harbour structures (site 2), bollards (site 3, Fig. 2.8a), ancient roads (site 4) and fish tanks (site 5, Fig. 2.8d) related to the ancient "Portus Iulius", provide RSL depths between -3.8 m and -4.2 m. The Roman pier R7 provides a similar depth of -3.8 m (Aucelli et al., 2020) (Fig. 2.7g).

In the offshore of Baia, the road at Punta Epitaffio (site 6) and the fish tank at Castello di Baia (site 7, Fig. 2.8e), define the deepest (-44 m) RSL position in the Pozzuoli Bay. In the western side of the caldera, the RSL position from fish tanks in Bacoli (site 8) and Punta Pennata (site 11, Fig. 2.8f), harbour structures (sites 9, 10) and bollards (site 12, Fig. 2.8b) show a monotonic decrease in depth of about 1 m, from -4.4 to -3.4 m. Moving from Bacoli to Miseno, the fish tanks (sites 13, 14, 15) yield RSL depths that slightly increase from -3.4 to -3.7 m.

The fish tank (site 16) at Torregaveta is located at the external side of the caldera, and its RSL point lies at a depth of -3.7 m. Moving away from the caldera, the bollard R8 at Procida Island provides an RSL at -4.5 m (Putignano et al., 2014) (Fig. 2.7h). For this analysis, a fish tank (site 17) is also considered at Sorrento, ~30 km southeast of the Pozzuoli Bay, which yields an RSL at -1.2 m.

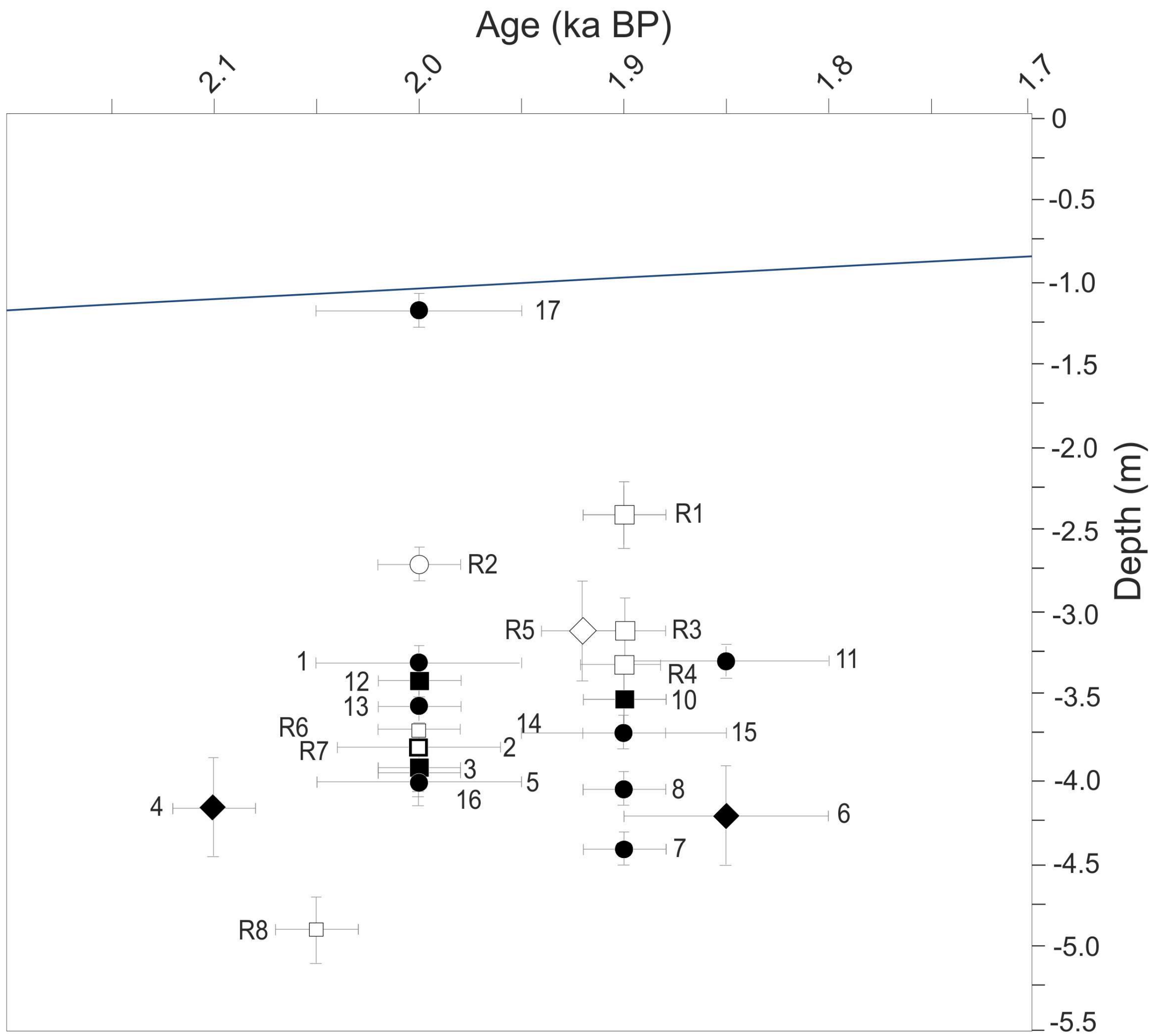

Figure 3.10. Depth distribution of fish tanks, harbour structures and onland constructions. Black dots numbered 1 to 17 are original data. White dots labelled R1 to R8 are published data. Blue solid line: predicted sea-level curve (from Lambeck et al., 2011).

Chapter 4 – Discussion

4.1 Time history of vertical movements in the Campi Flegrei caldera offshore

The present position of RSL indicators detected in seismic profiles and morpho-bathymetric data reflects a combination of processes, including deformation at a local (volcano-tectonic) or regional scale and global sea-level changes that have occurred since their development. When considering their original formation depth, the position of indicators provides quantitative information on the cumulative RSL that occurred since then (Table S1). Independently from their age, all the indicators are currently located below their estimated formation depth and thus experienced net subsidence (Fig. 4.1).

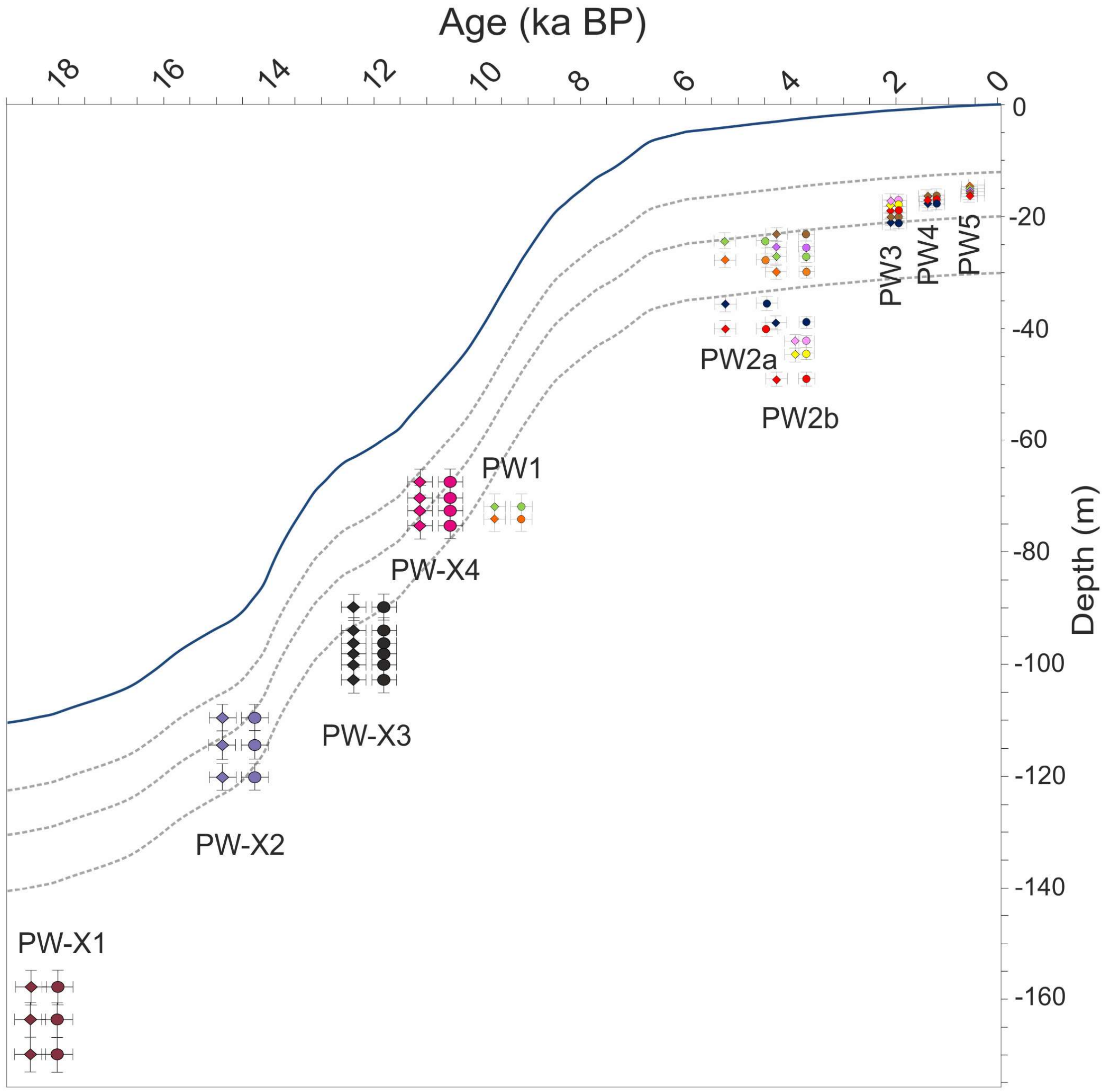

Figure 4.1. Depth distribution of PWs shelf-edge. Blue solid line: predicted sea-level curve (from Lambeck et al., 2011). Grey dashed line: curve of PW paleo-bathymetry. Coloured diamonds and dots are the oldest (base) and youngest (top) edges of individual PWs, respectively.

However, by considering the stacking pattern of sequentially younger prograding and aggrading seismic units, the vertical movement of specific markers through time can be reconstructed. Figures 4.2a to h show eight curves illustrating the time-dependent vertical movements of individual seismo-stratigraphic indicators in different structural sectors of the Pozzuoli Bay. Specifically, profiles offshore Miseno (0805) and Castello di Baia (1218) provide insights into the vertical movement history at the western caldera rim. Profiles in the Baia offshore (0806), Bagnoli (0905), and Nisida (0801) are representative of the caldera collar. Profiles offshore La Starza-Pozzuoli (1223), Rione Terra-Accademia (1401), and Monte Nuovo (0902) give hints on the behaviour of the resurgent dome sector (Fig. 2.1).

Afterwards, by correcting for the PW paleobathymetry depth (storm-wave base level) and removing the contribution of the sea-level rise, it was possible to derive the vertical displacement path at different locations (Figs. 4.2a to 4.2h).

The reconstruction of incremental RSL and vertical displacements returns to ∼10 ka in the caldera's western rim and ∼5 ka in the central and eastern sectors.

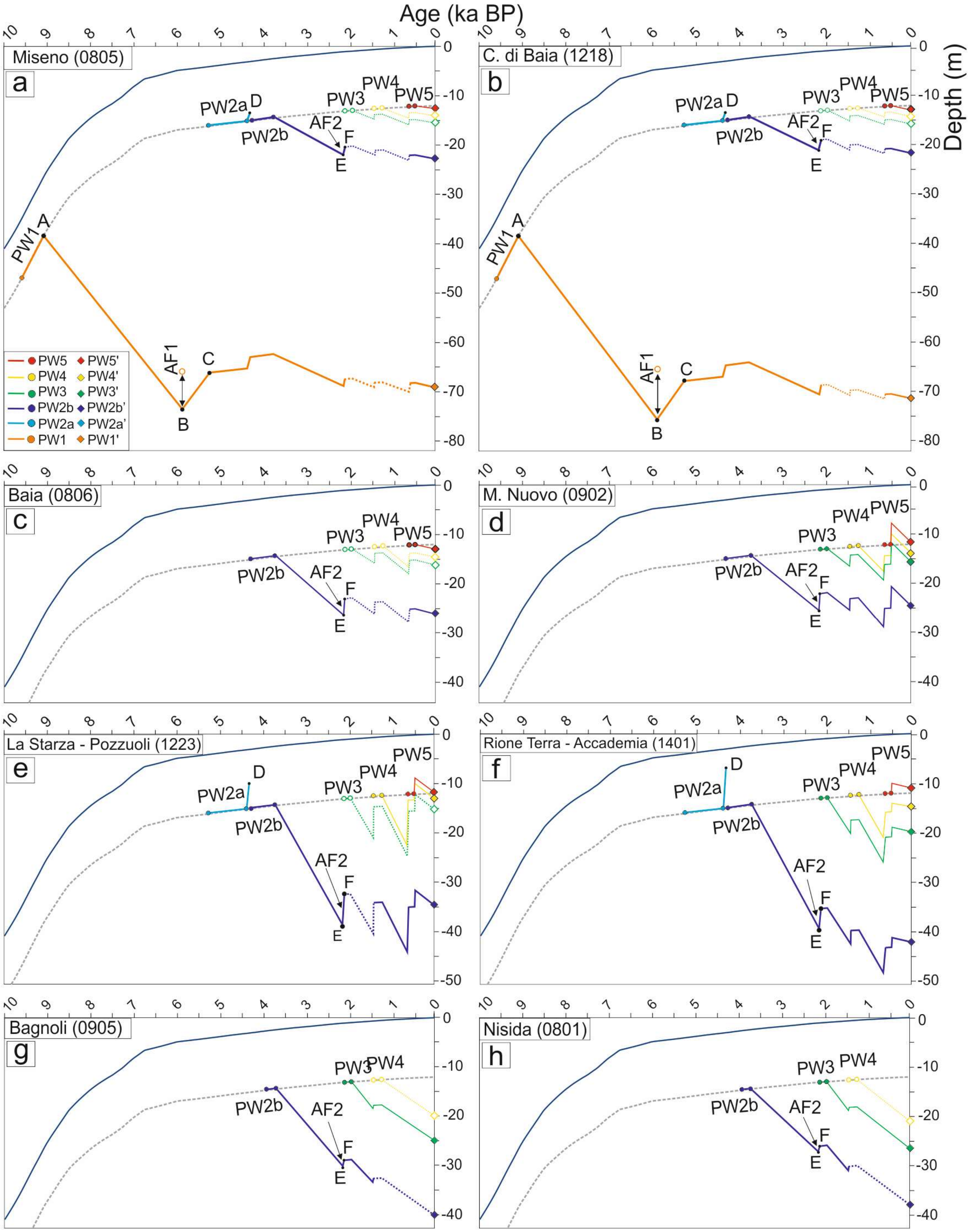

Figure 4.2 (a to h). Time-dependent vertical movement at selected locations in the Pozzuoli Bay (Fig. 5a) derived from prograding wedges and Aggrading Fills seismo-stratigraphic indicators. Blue solid line: predicted sea-level curve (from Lambeck et al., 2011). Letters A to F indicate paleodepths of specific PW markers at key moments of the ground deformation history. Grey dashed line: wave-base level curve.

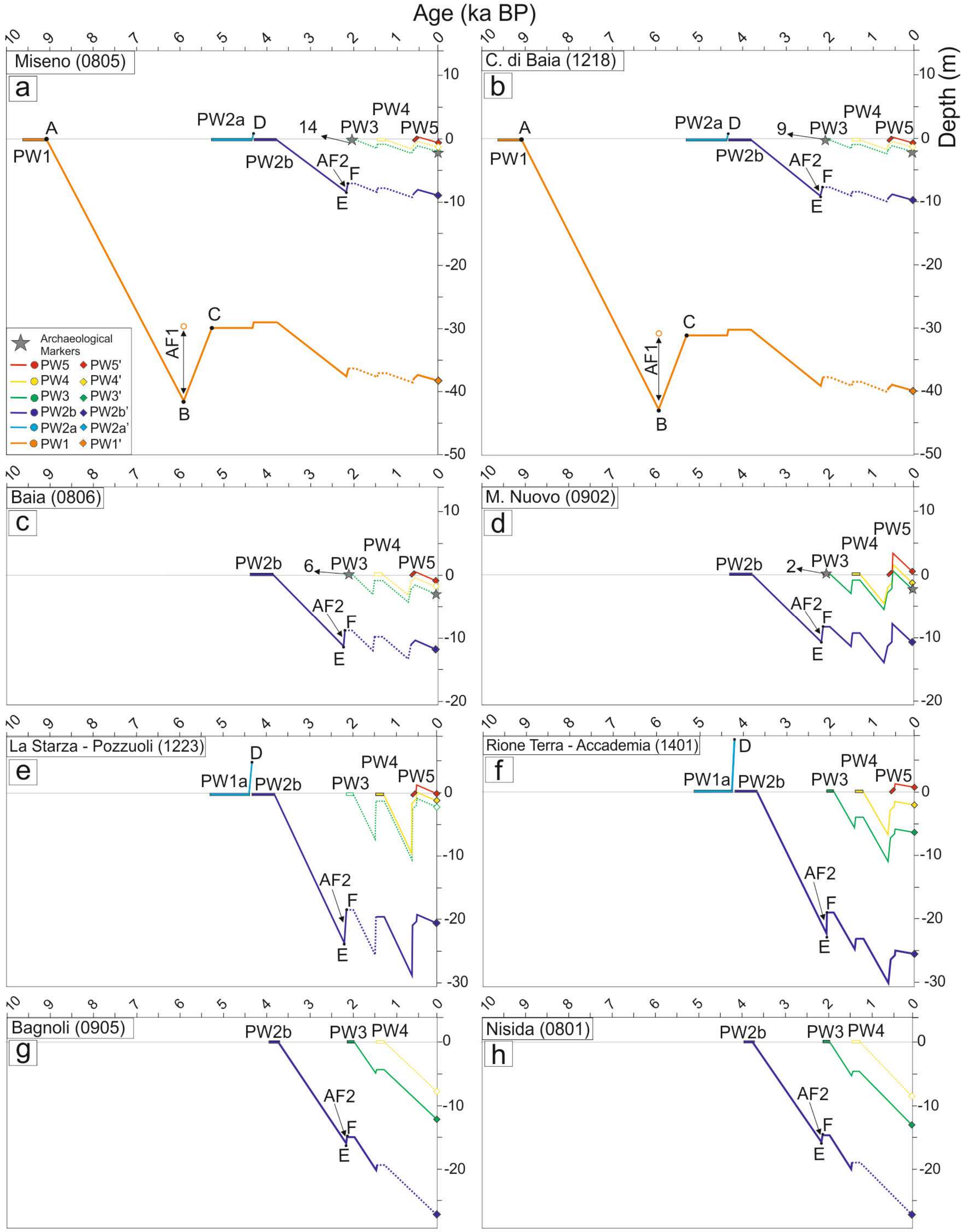

Figure 4.3 (a to h). Vertical Deformation derived from Prograding Wedges and Aggrading Fills seismo-stratigraphic indicators (coloured bars) and archaeological indicators nearby seismic lines (grey stars with site number). Letters A to F indicate paleodepths of specific PW markers at key moments of the ground deformation history. Grey dashed line: wave-base level curve.

In the western side, marker PW1 formed between 9.6-9.1 ka during a fast interval of sea-level rise (Figs. 4.2a, 4.2b). Growth of the wedge indicates a period of RSL still-stand (Fig. 2.3a) that is interpreted as the occurrence of uplift. Although this uplift is not recorded in seismic images, the growth of PW1 during a monotonic sea-level rise suggests that uplift occurred before 9.6 ka and set stability conditions for the wedge formation (Figs. 4.2a, 4.2b).

It could be argued that the formation of prograding wedges depends not only on the tectonic contribution but also on other factors, including the sediment supply, the paleo-morphology and the variations of the velocity of sea level rise. Indeed, the rate of sea level change has probably varied during transgressions in the last 18 ka (Zecchin et al., 2013).

The hypothesis proposed in this thesis is that the formation of the PWs is associated with the transition between two different segments of the RSL cycle, coincident with uplifts and subsidences, respectively, as documented onshore. In particular, the PWs formed at the end of an uplift phase that led the sea-floor at the position at the storm-wave level, and the development of first clinoforms occurred. Our correlation with the onshore seismo-stratigraphy provided by Natale et al. (2020; 2021) excludes the hypothesis that the PWs formation can be ascribed only to variations of the sea-level velocity. Indeed, a very tied stratigraphic correlation between events of deformation found onshore, and the development of PWs in the offshore has been found. This is reasonable comparable in terms of ages and magnitudes of the documented episodes of uplifts and subsidences.

Deactivation of PW1 (point A, Figs. 4.2a, 4.2b) and ensuing deposition of AF1, characterised by prominent transparent facies, denote an RSL rise. AF1 coincides with the subsidence phase documented onland at La Starza and offshore by a volcaniclastic-free marine sequence between ~9.1 and ~5.9 ka (Isaia et al., 2019; Natale et al., 2021). Isaia et al. (2019) estimated a ~65 m maximum paleobathymetry for this marine sequence. The estimated paleobathymetry and the 10 m thickness of AF1 were used to predict a depth of -75 m for PW1 at ~5.9 ka (point B, Figs. 4.2a, 4.2b). Based on the reconstruction carried out in this study, it is assumed that this depth represents the maximum deepening toward the end of AF1 deposition. It is not excluded that maximum deepening could have occurred more abruptly, and a low-stand might have developed earlier than ~5.9 ka. It is also assumed that AF1 mostly formed during the subsidence phase, and the deposition during the ensuing shallowing phase was minimal.

The maximum subsidence between ~9.1 and ~5.9 ka is estimated using the 45 m depth separation (DS) between the original paleobathymetry (35m below present) for the top of PW1 (point A, Figs. 4.2a, 4.2b) and its -75 m depth reached at ~5.9 ka (point B). By considering a 15 m incremental sea-level rise (SLR) and a 10 m maximum thickness (MT) of AF1 at the shelf (Figs. 3.4a, 3.4b, 4.2a, 4.2b), with an estimation of 40 m of maximum subsidence S (Figs. 4.2a, 4.2b) using the notation:

$$S=DS-SLR+MT \tag{1}$$

According to the reconstruction of La Starza sequence, subsidence in the dome resurgence area waned ~5.9 ka and was replaced by rapid uplift (Isaia et al., 2019; Natale et al., 2021). The inferred age for onset of PW2a (~5.2 ka) is slightly younger than the ~5.9 ka commencement of uplift at La Starza (Isaia et al., 2019). It is assumed that such time lag of some centuries exists in the offshore, too. The RSL rise related to subsidence had shifted the shelf depositional system landward between 9.1-5.9 ka, regarding the interval between ~5.9 ka (start of uplift) and ~5.2 ka (onset of PW2a) as the time required to bring the present shelf break back to the wave-base level.

The uplift phase started at ~5.9 ka is constrained using the present 50 m depth separation (DS) between PW1 and PW2a, which currently lie at 70 m and 25 m depth, respectively (diamonds PW1' and PW2a', Figs. 4.2a, 4.2b). This 50 m DS must have existed at 5.2 ka when PW2a started forming above PW1 (point C). PW1 in the western sector must have been uplifted 15 m, considering a 5 m sea-level rise during this period (Figs. 4.2a, 4.2b).

The growth of PW2a between ~5.2-4.5 ka documents a decrease of uplift coincident with a substantial slowing of the SL rise (Figs. 4.2a to 4.2h). The development of PW2a offshore is consistent with the decrease of uplift documented at La Starza during this period (Isaia et al., 2019).

A renewed uplift at the shelf is documented by the superposition of two distinct wedges (PW2a and PW2b), which form a compound down-stepping geometry (Fig. 2.3b) observed in the resurgent sector between La Starza and Rione Terra-Accademia (Figs. 3.4b, 3.4c) and in the western side of the bay off to Miseno and Baia (Fig. 3.4a). This uplift is correlated with the abrupt event reported at La Starza between 4.4 ka and 4.2 ka by Isaia et al. (2019). Onshore, the ~4.3 ka uplift was preceded by short-time subsidence documented at La Starza by the marine/transitional sequence deposition known as the "Pozzuoli Unit" (Isaia et al., 2019). Because of the later uplift, the shelf does not preserve the record of this subsidence. However, a short-lived transgressive phase is recorded by stratal architecture in the basin (Natale et al., 2021).

Uplift led to the development of the main abrasion surface (AS) imaged offshore, which eroded the basal part of PW2a. The amount of uplift has been estimated through a graphical reconstruction of the geometry of PW2a, using as constrain its preserved basal part and a size comparison with PW2b. Specifically, the missing foreset-topset transition of PW2a was estimated by using the overlap of its existing part, represented by the equivalent foreset-topset transition within PW2b (inset in Fig. 2.3b). The amount of uplift has different values in the resurgent dome for the western sector (point D, Figs. 4.2a, 4.2b, 4.2e, 4.2f). Between La Starza and Accademia, uplift was 5-10 m. In the western caldera, between Baia and Miseno, the estimates are minor uplift (<2 m). Following the uplift at ∼4.4 ka, PW2b formed during a phase of stability that lasted until 3.7 ka (Figs. 4.2a to 4.2h). In the eastern sector, the development of PW2b is recorded only after ∼3.9 ka on the edge of the Nisida volcanic edifice (Fig. 3.4d, 3.5d). This occurrence may be related to the near coeval eruption of Nisida (~3.9 ka, from Arienzo et al., 2016) that might have destroyed the older part of the wedge.

After ∼3.7 ka, aggradation fill AF2 developed above PW2b and AS (Figs. 3.4a to 34d, 3.5a to 3.5d) during a minimal SL rise testifying to the beginning of the recent most subsidence. Subsidence was monotonic between ∼3.7-2.1 ka, and after ∼2.1 ka, three short-term uplift pulses interrupted it. The time-dependent pattern of markers displacement is constrained using the present depth separation (DS) between a sequentially developed couple of wedges PW2b'-PW3', PW3'-PW4', and PW4'-PW5' (Figs. 4.2a to 4.2h). These wedges are presently stacked at depths that increase with their age because of the long-term subsidence. The DS between a wedge couple indicates the net subsidence occurred during their sequential development. However, the existence of the wedges testifies the interruption of the subsidence, thus to short-lived uplifts.

The pattern of vertical movement after ∼2.1 ka when the uplift pulses occurred was reconstructed, combining the DS between sequential PWs and estimates of subsidence coming from geoarchaeological observations, specifically from the Pozzuoli *Serapeum* (Bellucci et al., 2006; Di Vito et al., 2016).

The sum of subsidence (S) of the older wedge of the coupled PWs and the SLR between them, minus DS, provides the uplift (U) preceding growth of the youngest ones:

$$U=S-DS+SLR \qquad (2)$$

Because the subsidence at the *Serapeum* is probably a maximum estimate because of the location of this site at the apex of the down-lifting resurgent dome, its value has been scaled proportionally for the entire shelf based on the current DS estimates for the wedge stacks. In addition, the displacement estimates from archaeological data have been used to infer the pattern of movement in sectors where one or more wedges are lacking (dotted parts of curves in Figs. 4.2a to 4.2h, 4.3a to 4.3h).

Using notation (1), the thickness of AF2 and the DS between PW2b and PW3 (diamonds PW2b' and PW3' in Figs. 4.2a to 4.2h) has been used to estimate the amount of maximum deepening that occurred between ~3.7-2.1 ka. This depth (point E, Figs. 4.2a to 4.2h) indicates the accommodation space created by subsidence and a limited (1 m) sea-level rise. A 2-3 m thickness has been considered for AF2 in the western sector between Miseno and Monte Nuovo (Figs. 3.4a and 4.2a to 4.2d), 8 m for La Starza-Pozzuoli (Figs. 3.4b, 4.2e), 10-12 m for Rione Terra-Accademia (Figs. 3.4c, 4.2f) and 3-4 m for Bagnoli and Nisida (Figs. 3.4d, 4.2g, 4.2h).

The largest subsidence in the resurgent dome area (25-27 m) is found from La Starza to Rione Terra-Accademia (Figs. 4.2e, 4.2f). Subsidence was 8-10 m (Figs. 4.2a to 4.2d) in the western sector and 12 m in the eastern sector off Bagnoli and Nisida (Figs. 4.2g, 4.2h). Considering that this time interval was characterised by a lack of volcaniclastic input (Fig. 4.2a) that could have caused loading compaction, the subsidence is mostly related to volcano-tectonic processes.

The first short-term uplift led to the formation of PW3 at ~2.1 ka, and its age is anchored to geo-archaeological data from Aucelli et al. (2021) offshore La Starza. Accordingly, growth of PW3 occurred during 200 years of ground stability between 2.1-1.9 ka. The uplift is portrayed by estimating the vertical displacement of older PW2b (between points E and F, Figs. 4.2a to 4.2h). The uplift is estimated to have reached 3 m in the western (Baia to Miseno) and eastern sectors (Bagnoli to Nisida) and 4-7 m in the central sectors (Monte Nuovo to Accademia) (Figs. 4.2a to 4.2h). Uplift is not recorded in the southwestern sector where PW3 is lacking (Fig. 3.1).

After ~1.9 ka, subsidence prevailed until 1.4 ka and led to the deactivation of PW3. The 7 m subsidence of the resurgent dome at the *Serapeum* site (Bellucci et al., 2006; Figs. 4.2e, 4.2f) extrapolates to 5 m in the eastern sector (Figs. 4.2g, 4.2h) and in the northwest between Baia and M. Nuovo (Figs. 4.2c, 4.2d). In the western sector from Baia to Miseno, subsidence is 2 m (Figs. 4.2a, 4.2b).

The second historical uplift occurred at ~1.4 ka and affected the entire coast of the Pozzuoli bay (Cinque et al., 1991; Bellucci et al., 2006). As reported by Bellucci et al. (2006), uplift peaked at 7 m between Rione Terra and Accademia (Figs. 4.2a to 4.2h) and is estimated that it reached 1 m in the western (Baia to Miseno) and eastern sectors (Bagnoli to Nisida), and 3 m off Monte Nuovo. Following uplift, growth of PW4 took place during 200 years of ground stability between 1.4-1.2 ka.

After ~1.2 ka, subsidence renewed until ~0.6 ka. The 10 m subsidence taken for the *Serapeum* (Figs. 4.2e, 4.2f) translates to 7 m between Baia and Monte Nuovo (Figs. 4.2c, 4.2d). In the western (Baia to Miseno, Figs. 4.2a, 4.2b) and the eastern (Bagnoli to Nisida, Figs. 4.2g, 4.2h) caldera sectors, subsidence reached 5 m.

At ~0.6 ka, 100 years of uplift (1430-1536 CE) preceding the Monte Nuovo eruptive unrest (1536-1538 CE) affected the whole caldera, from a maximum of >8 m in the Pozzuoli area to a minimum of <2 m in the peripheral sectors (e.g., Bellucci et al., 2006; Di Vito et al., 2016). Oppositely, in the two years before the eruption, large uplift (>12 m) centred in the area around the future Monte Nuovo and had minimal values elsewhere (<1 m).

PW5 is estimated to form during the pre-eruptive unrest (1430-1536 CE) when the largest coastal deformation is reported at the resurgent dome (Di Vito et al., 2016). The observation that PW5 is well developed between Accademia and Monte Nuovo (Fig. 3.1) supports the age attribution provided in this study. The amount of uplift is estimated based on the present separation depth between PW4 and PW5 (diamonds PW4' and PW5'; Figs. 4.2a to 4.2h, 4.3a to 4.3h).

After the ~0.6-0.5 ka uplift, the CF caldera offshore underwent monotonic subsidence that lasted until the middle of the last century and reached values of 2-4 m (Figs. 4.3a to 4.3h). The last bradyseismic unrest that started around 1950 is too young to be recorded at the investigated depths.

4.2 Implications for the last ~10 ka caldera evolution

The existence of significant post-NYT ground uplift and subsidence at the Campi Flegrei caldera was previously recognised through investigation of vertical changes in facies of marine and volcaniclastic deposits currently uplifted above sea-level at La Starza Terrace (Marturano et al., 2018; Isaia et al., 2019; Vitale et al., 2019). These studies were limited to the coastal area and chiefly provided clues for the vertical deformation history of the resurgent dome (Fig. 1.4). The seismo-stratigraphic markers have been used to estimate ground deformation in the offshore part of the resurgent dome and its peripheral sectors. In addition, the use of archaeological data tied to sea level was used to link the onshore and offshore reconstruction during the last ~2 ka BP.

Growth of wedge PW1 during a ground stability period at 9.6–9.1 ka underpins the existence of a previous uplift. Although, this uplift is documented at La Starza (Isaia et al., 2019) and detected by seismo-stratigraphic analysis in the Pozzuoli Bay (Natale et al., 2021). As noted previously, PW1 is only observed in the western sector of the bay (Fig. 3.1). There is no evidence for the development of PW1 elsewhere because either the wedge never formed or, more likely, and it was dismantled by erosion during later uplifts caused by younger volcanism. In light of the reported significant (~70 m) dome uplift onshore (Isaia et al., 2019), uplift likely occurred in the offshore sectors.

Similarly, subsidence (~9.1-5.9 ka) is documented only in the western sector of the bay. Subsidence at this time is reported in the resurgent dome area onland (Marturano et al., 2018; Isaia et al., 2019) and testified by stratal architecture in the offshore (Natale et al., 2020; 2021). The computed subsidence rate (15 mm/a) is close to the estimate proposed in the above studies for the resurgent dome, supporting a linked ground deformation in the two sectors.

The rapid growth of the central dome lasted between ~5.9-5.2 ka led to the formation of PW2a when uplift slowed down, and Epoch 2 commenced (Fig. 3.9c). The estimated uplift during dome resurgence in the western sector is 15 m (Figs. 4.2a, 4.2b), one order of magnitude less than the vertical displacement (100 m) estimated for the central dome (Marturano et al., 2018; Isaia et al., 2019). This discrepancy may reflect the lateral variability in the effectiveness of the deformation source, centred beneath the Pozzuoli area (Fig. 3.1).

PW2a was interrupted at ~4.4 ka by a brief uplift phase until ~4.2 ka. Uplift peaked (10 m) offshore Pozzuoli-La Starza and is observed with a lesser magnitude (2 m or less) in the western sector (Figs. 4.2a to 4.2h). Although the estimations involve some degree of uncertainty in reconstructing the eroded PW2a, which constrains uplift, its value is broadly comparable to the coeval uplift estimated at La Starza (Isaia et al., 2019).

After ~3.7 ka, subsidence affected all the offshore caldera and continued steadily until 2.1 ka. The estimated subsidence during the 3.7-2.1 ka time interval ranges from a minimum of 5-10 m in the ring fault zone to a maximum of 20-25 m in the caldera collar and at the central resurgence (Figs. 4.2a to 4.2h). Indeed, a subsidence rate of 14 mm/a has been estimated off La Starza (profile 1223, Fig. 4.2e), which matches the value proposed by Marturano et al. (2018) in the conterminous area onshore. The dome sector between Rione Terra and Accademia exhibits the steepest subsidence gradient, still reflected in the total deformation (Fig. 4.2f). This marked south-east asymmetry of deformation may reflect the combination of the collapse of the central dome and processes along the ring-fault zone in the eastern flank of the caldera.

Since ~2.1 ka, three short-term uplift pulses superposed but did not overwhelm the subsidence initiated at ~3.7 ka. The three stability moments testified by wedges PW3, PW4, and PW5 suggest dome resurgences, accompanied by previous uplift episodes but not by eruptions except for the 1538 CE unrest, with venting peripheral to the maximum uplifted area (Di Vito et al., 2016). The cumulative effect of these uplifts produced a small (1 m) positive bulge centred offshore the central dome in the long-term subsidence trend (Fig. 4.4). Oppositely, uplift did not significantly counteract subsidence in the eastern sector, which likely highlights the predominance of processes associated with the ring faults.

The net subsidence since ~3.7 ka in the eastern part of the ring fault zone computed on PW2b occurred at a rate of 7 mm/a (Figs. 4.3g, 4.3h), a value comparable to that recorded by younger PW3 (Fig. 4.4). When the effects of the post-2.1 ka uplifts are removed, the subsidence rate in this sector approaches 10 mm/a (Figs. 4.3g, 4.3h). Offshore the resurgent dome (La Starza), the net subsidence since ~3.7 ka is 5 mm/a, whereas, since ~2.1 ka, it is 1 mm/a. Without the contribution of the later uplifts, subsidence in the last 3.7 ka offshore La Starza would approach 14 mm/a (Figs. 4.3e to 4.3f). The subsidence rates in both the resurgent dome and the eastern ring fault detracted of later uplifts show values broadly comparable to the 17 mm/a subsidence estimated between 9.1-5.9 ka in the western ring fault, possibly highlighting a cyclic recurrence of volcano-tectonic deflection during the Holocene.

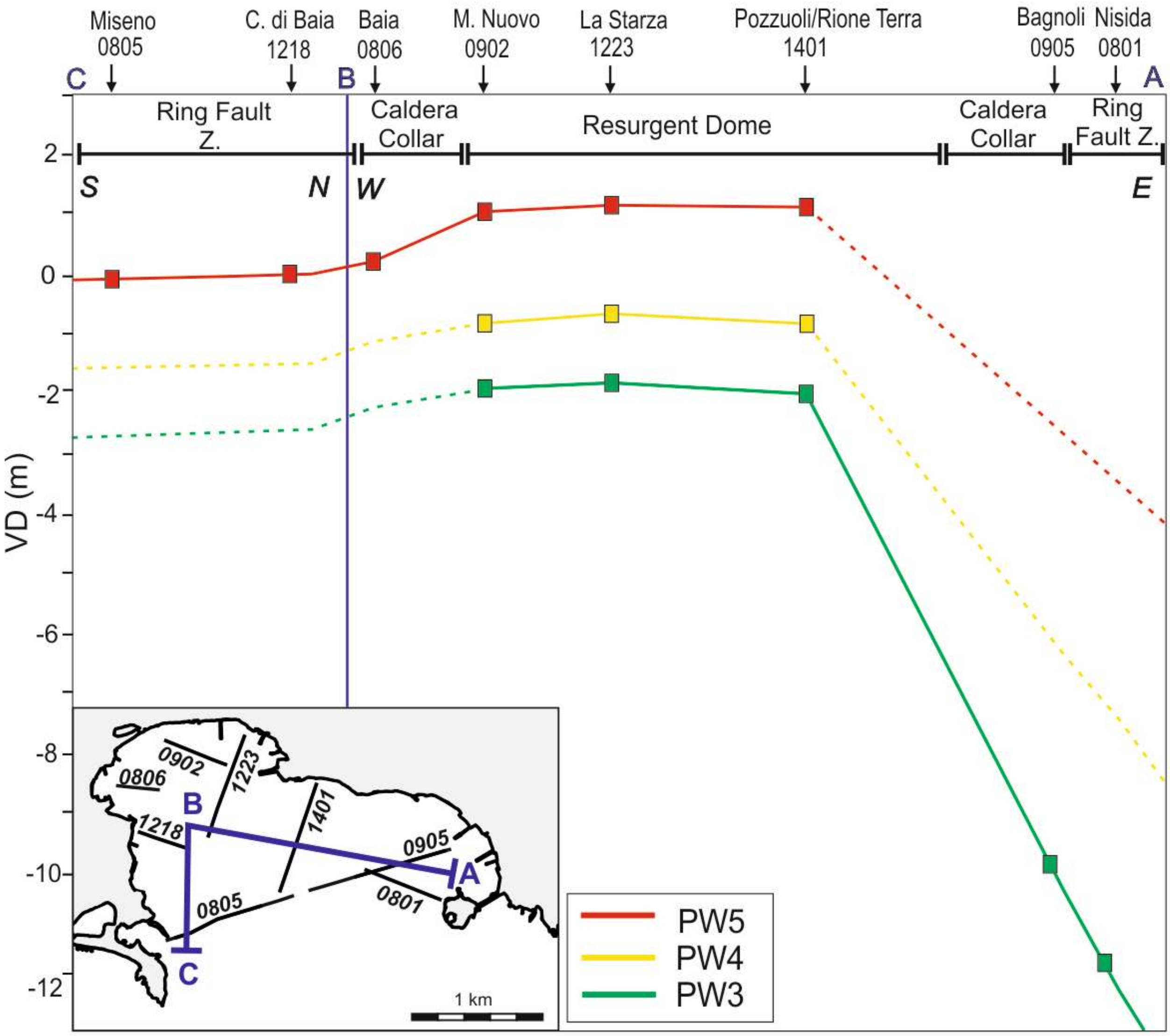

Figure 4.4. Vertical deformation (VD) of markers PW3, PW4 and PW5 in the last 2.1 ka along with lines AB and BC (inset). The PWs detected in seismic profiles have been projected almost orthogonal to the lines.

4.3 Vertical movements outside the Campi Flegrei caldera in the last ~18 ka

The regional subsidence in the last 18 ka has been estimated in the external part of the CF caldera through the vertical displacement analysis of PW-X1, PW-X2, PW-X3 and PW-X4. Outside the Pozzuoli Bay, where the wave energy likely reaches greater depths, the formation depth for PWs has been estimated to be 25 m differently from the 12 m in the more repaired bay setting. This estimation has been carried out through the observation of the difference in depth between the inner margin (-140 m) and the shelf-edge (-165 m) of PW-X1 (Fig. 3.7d).

PW-X1 has been observed in the southernmost part of the Pozzuoli Bay, at the border with the two main canyons (Dohrn and Magnaghi). This wedge formed at the end of the LGM because of the protracted sea-level fall that, during this time, reached a maximum depth of 120 m. PW-X1 developed between 18.5 and 18 ka and is now found ~30-40 m below the PW formation curve. So, PW-X1 suffered subsidence of about 35 m in 18 ka, at a rate of ~2 mm/a.

The development of PW-X2 to PW-X4 between 10 and 14 ka in the external offshore of the CF caldera is attributable to two hypotheses. The first one is related to the ground movements related to the formation of the submerged volcanic edifices (Nisida, Penta Palummo and Miseno Banks). A second hypothesis involves the decreasing rate of the sea-level rise that in this time-lag suffered many slowdowns due to brief minor glacial periods (es. Younger Dryas). The calculated average subsidence trend for these wedges have been estimated to be 1.5 to 2 mm/a moving from east to west (Fig. 4.5).

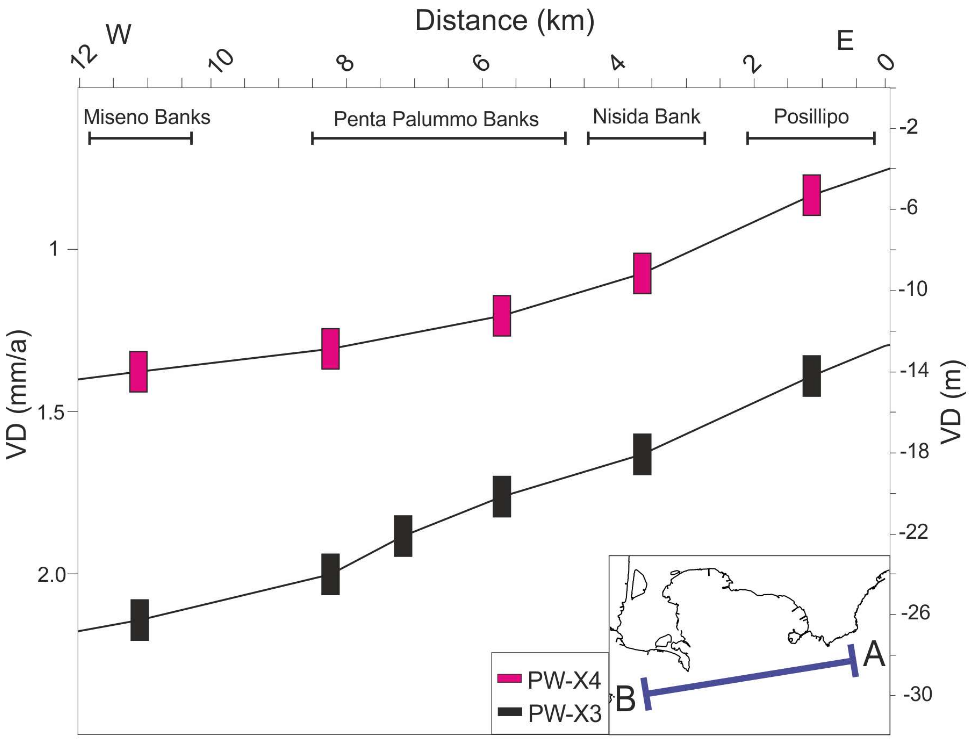

Figure 4.5. Vertical deformation (VD) of PW-X3 and PW-X4 in the last 12 ka, along with an ENE-WNW profile. The PWs detected in seismic profiles have been projected orthogonally to the lines.

4.4 Spatial variations in ground deformation during historical time

Considering the predicted sea-level curve (Lambeck et al., 2011), the Roman age (~2 ka BP) archaeological markers analysed in this study, independently from their location, have experienced a net although variable subsidence depending on their location (Table S2; Figs. 3.10, 4.6).

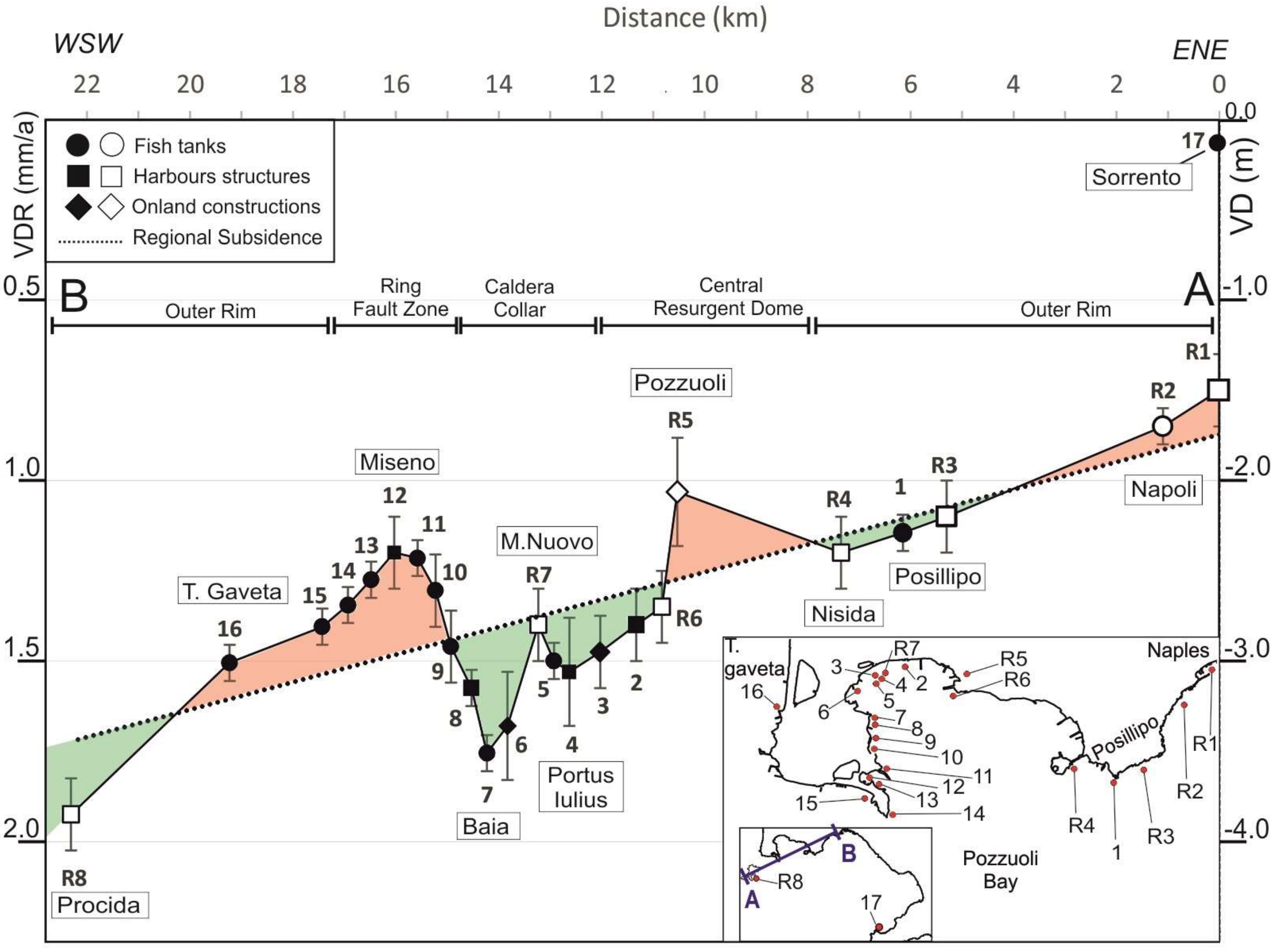

Figure 4.6. Vertical deformation (VD) and rate (VDR) from archaeological markers distributed along with a NE-SW trending profile (A-B, inset). Site 17 is not projected on the profile and is indicative of an external reference frame. The solid line is the net displacement of markers, and the dotted line is a linear fit to data indicative of a regional subsidence trend. The green and red areas show deviations between the net displacement and the calculated background subsidence and represent the local contribution of uplifts and subsidence, respectively. RSL data derived from fish tanks, harbour structures, and onland constructions are represented with dots, squares, and diamonds. Black dots represent original observations, and white dots are published data (Aucelli et al., 2018, 2020; Bellucci et al., 2006; Putignano et al., 2017; Vacchi et al., 2019; Pappone et al., 2019).

To estimate the historical deformation trend in the CF caldera area, from Naples to Procida Island, projected each marker position has been projected, corrected for sea-level change, tide and functional heights, onto a NE-SW oriented profile (Fig. 4.6). This Roman sea-level distribution against the Sorrento site has been benchmarked, whose position indicates quasi-stability (site 17, Figs. 3.10, 4.6). The profile highlights clear differences in the vertical land movements between adjacent sectors that display positive and negative shifts from monotonic subsidence, labelled as regional (Fig. 4.6). The regional subsidence increases from 1.5 m (0.5 mm/a) near Naples in the east to 4.0 m (2 mm/a) at Procida Island within a ~25 km distance. The short-wavelength patterns appear to be controlled by their location within different caldera structural sectors and indicate local-scale processes (Fig. 4.6).

Sites R1 and R2 at Naples fall outside the caldera rim and document subsidence very close to the regional curve, with hints of a modest counterbalancing uplift (Fig. 4.6). Moving westward along the profile, higher subsidence (2.2 m) relative to Naples is documented by the Roman pillars, and fish tanks (sites R3, 1, R4) submerged off Nisida Island and Posillipo. This area lies near the outer caldera rim and closely follows the regional trend (Fig. 4.6).

West of Nisida, a local uplift superposed on the regional subsidence is documented by the Pozzuoli *Serapeum* site R5, which corresponds to the central resurgence zone (Fig. 4.6). Sites R6 to site 7 from Pozzuoli to Baia document increasing subsidence up to 3.5 m as testified by the submerged archaeological sites of *Portus Iulius* and Baia. Only site R7, lying offshore Monte Nuovo, shows an uplift that realigns the site to the regional curve.

Differently, the coastal sector from Baia to Miseno lies on the transition between the caldera collar and the ring fault zone and shows a local uplift that brings the sea-level markers (sites 10 to 15) well above the regional trend (Fig. 4.6). West of here, the local uplift progressively wanes (sites 12 to 16), and Torregaveta site 16 almost aligns with the regional subsidence. The westernmost site at Procida Island (R8) exhibits subsidence larger than that predicted by the linear trend. Different fits can ameliorate this inconsistency without changing the significance of the local processes.

Unlike seismo-stratigraphic markers, which allow reconstructing incremental positive and negative vertical movements in the last ~2 ka, archaeological data only provide the net subsidence during this time frame. Notwithstanding, the observation of displacement paths of PW3 at several sites terminates at the present position of archaeological markers (numbered black stars) supports the age assignment for the three youngest wedges provided in this thesis (Figs. 4.2a to 4.2h).

4.5 Significance of regional and local ground movements in the last ~2.1 ka

As outlined above, archaeological data support the results of seismo-stratigraphic analysis and provide a denser dataset to evaluate spatial variations in the competing effects of uplift and subsidence caused by intra-caldera and extra-caldera phenomena during historical times. The small-wavelength ground movements superposed on the regional subsidence curve reflect the contribution of local sources related to the caldera dynamics. The net result is generally non-uniform subsidence, indicating a predominance of regional processes (Fig. 4.6).

The local processes display a wavelength of 3-5 km, such as the well-known uplift of the resurgent dome centred at Pozzuoli (site R5). Archaeological data indicate that the rim sector in the west experienced local uplift as well (Fig. 4.6). This uplift possibly ensues from a flexural response to caldera collapse in the hanging-wall of the rim fault. In between these two sectors of local uplift, the collar displays enhanced subsidence that peaks at Baia (site 7) in the western caldera collar. This surplus of negative displacement concerning the regional trend reflects the active processes across the ring fault zone. Within this subsiding zone, site R7 shows a localised uplift (Fig. 4.6) that has been related to the 1430-1536 CE unrest, which counteracted the regional subsidence

The wavelength of the regional processes cannot be defined by the archaeological data distributed from Procida to Naples. Therefore, the site of Sorrento is considered s a reliable benchmark to estimate the regional tectonic processes that affect the entire Campanian margin. The northward projection of Sorrento site 17 on the profile suggests that the regional subsidence trend may vanish at an additional 20-25 km to the east (Fig. 4.6). This projection would place the Sorrento site and the termination of the regional subsidence close to the border between the Campanian Plain and the Southern Apennines. Although this reconstruction is schematic, it does not account for additional processes related to the emplacement of the Somma-Vesuvius volcanic edifice. It is consistent with the location of the Sorrento site at the southern border of the Campanian Plain (Fig. 1.2). The rate is comparable to the oldest wedges PW-X3 and PW-X4 (Fig. 4.6).

The eastward-increasing regional subsidence evidenced by archaeological data and by PWs outside the caldera, thus not affected by intra-calderic movements, may reflect the transition between the uplifting orogen and the deeply-foundered Tyrrhenian back-arc basin (Fig. 1.2).

Conclusions

This thesis provides the first quantitative assessment of ground movements in the internal and external parts of the Pozzuoli Bay, which represents the offshore part of the high-risk Campi Flegrei caldera. The reconstruction relies on the alternation of prograding and aggrading seismic units in high-resolution reflection profiles. The key indicators for the reconstruction are several generations of PWs that document the position of the coeval wave-base level. PWs were previously used in regions of relatively slow tectonic deformation to estimate the long-term displacement of the sea-bed. This study represents the first attempt to apply this method in a complex volcanic area dominated by high-frequency ground oscillations tuned by volcano-tectonic processes.

The proposed reconstruction highlights that PWs formed at the end of an uplift phase when a period of ground stability favoured the redistribution of sediments at the shelf-break. The PW continued growing until the onset of the subsidence part of the cycle sank the sea-bottom beneath the wave-base level. Under this circumstance, aggradation follows to fill the accommodation space created by subsidence. Both the PW and overlying aggradation fill could be destroyed by stronger, new uplifts that led to the development of abrasion surfaces.

The analysis carried out in this study covers the entire caldera in the Pozzuoli Bay and allows us to appreciate the lateral variability of volcano-tectonic displacements. The obtained results complement previous studies on intra-caldera sediments exposed at La Starza succession that uplift and subsidence alternated during Holocene dome resurgence. The ground movements in terms of uplift found offshore are minor than those found in the central part of the resurgence onshore, reflecting the radial variability of the deformation pattern.

The occurrence of PW1 between Castello di Baia and Miseno first documents ground displacement in the western part of the ring fault zone during the early caldera evolution, which may reflect spatially clustered intra-caldera volcanic activity during Epoch 2. The well-developed growth of PW2 and the down-stepping relation between PW2a and PW2b offshore Pozzuoli and La Starza document the resurgence of the central dome during Epoch 3 with at least two pulses of uplift. Notwithstanding uplift, in the shelf, net subsidence prevailed to date. Subsidence started at the end of Epoch 3 (3.7 ka), and its rate decreased at 2.1 ka when punctuated by short uplift episodes documented by the development of smaller-size PW3 to PW5.

The younger PWs (PW3, PW4 and PW5) are characterized by a lateral extension of about 50 m developed in about 200 years. This contrasts with the 500 m lateral size of older PW1, PW2a and PW2b that formed in a longer time frame of 800-1000 years. These differences in size and time duration of older and younger PWs highlight that deformation has been characterized by differential signals: 1) a long-wavelength (several hundred years) time component, when larger, well-developed

PWs formed; and 2) a short-wavelength (100-200 years) time component when PWs with smaller size formed.

The occurrence of PW-X1 in the southernmost part of the Pozzuoli Bay documents the oldest RSL still stands in the datasets of seismo-stratigraphical markers analysed in this thesis. PX-X1, developed between 18.5 and 18 ka and found at 30-40 m below the PW formation curve, suffered subsidence at 2 mm/a. The net subsidence estimated by the analysis of the wedges PW-X3 and PW-X4 is likewise 2-3 mm/a, moving from east (Posillipo) to west (Procida).

Archaeological indicators tied to past sea-level integrated high-resolution seismo-stratigraphic data and provided a link between long and short-term displacements. Analysis of the spatial distribution of Roman age coastal structures allowed disentangling the contribution of regional tectonics from the local, volcano-tectonic signal. The regional signal has a spatial wavelength of over 50 km, an order of magnitude larger than the signal associated with intra-caldera processes.

The westward-increasing regional subsidence evidenced by archaeological data and PWs outside the caldera reflects the transition between the uplifting orogen and the deeply-foundered Tyrrhenian back-arc basin. This subsidence likely stems from crustal thinning processes that control volcanic phenomena in the Campi Flegrei region.

The multidisciplinary approach presented here highlights the suitability of high-resolution seismic images coupled to directly accessible coastal data (e.g. geo-archaeological structures) to investigate partly or totally submerged calderas of the world-spanning the sea-land transition.

Site	Line	Marker	Age (ka BP)	Paleo-sea-level (m)	Elevation (m)	Age U. (±ka)	Depth U. (±m)
Miseno	0805	Base PW1	9.6	-35.0	-69	0.2	2.0
		Top PW1	9.1	-26.0	-69	0.2	1.9
		AF1	5.9	-4.8	-74	0.2	1.3
		Base PW2a	5.3	-4.1	-21	0.2	1.2
		Top PW2a	4.4	-3.2	-21	0.2	1.1
		AS	4.3	-3.1	-10	0.1	1.1
		Base PW2b	4.3	-3.1	-22	0.2	1.1
		Top PW2b	3.7	-2.5	-22	0.2	1.0
		AF2	2.1	-1.4	-22	0.2	0.8
		Base PW5	0.6	-0.3	-12	0.0	0.5
		Top PW5	0.5	-0.1	-12	0.0	0.5
		AF2	0.1	0.0	-13	0.0	0.5
C. di Baia	1218	Base PW1	9.6	-35.0	-71	0.2	2.0
		Top PW1	9.1	-26.0	-71	0.2	1.9
		AF1	5.9	-4.8	-75	0.2	1.3
		Base PW2a	5.3	-4.1	-22	0.2	1.2
		Top PW2a	4.4	-3.2	-22	0.2	1.1
		AS	4.3	-3.1	-10	0.1	1.1
		Base PW2b	4.3	-3.1	-23	0.2	1.1
		Top PW2b	3.7	-2.5	-23	0.2	1.0
		AF2	2.1	-1.4	-20	0.2	0.8
		Base PW5	0.6	-0.3	-12	0.0	0.5
		Top PW5	0.5	-0.1	-12	0.0	0.5
		AF2	0.1	0.0	-14	0.0	0.5
Baia	0806	Base PW2b	4.3	-3.1	-25	0.2	1.1
		Top PW2b	3.7	-2.5	-25	0.2	1.0
		AF2	2.1	-1.4	-20	0.2	0.8
		Base PW3	2.1	-1.2	-15	0.0	0.5
		Top PW3	1.9	-1.0	-15	0.0	0.5
		AF2	1.4	-0.8	-18	0.0	0.5
		Base PW4	1.4	-0.7	-14	0.0	0.5
		Top PW4	1.2	-0.6	-14	0.0	0.5
		AF2	0.6	0.0	-18	0.0	0.5
		Base PW5	0.6	-0.3	-12	0.0	0.5
		Top PW5	0.5	-0.1	-13	0.0	0.5
		AF2	0.1	0.0	-14	0.0	0.5
M.Nuovo	0902	Base PW2b	4.3	-3.1	-24	0.2	1.1
		Top PW2b	3.7	-2.5	-24	0.2	1.0
		AF2	2.1	-1.4	-18	0.2	0.8
		Base PW3	2.1	-1.2	-15	0.0	0.5
		Top PW3	1.9	-1.0	-15	0.0	0.5
		AF2	1.4	-0.8	-19	0.0	0.5
		Base PW4	1.4	-0.7	-13	0.0	0.5
		Top PW4	1.2	-0.6	-14	0.0	0.5
		AF2	0.6	0.0	-19	0.0	0.5
		Base PW5	0.6	-0.3	-11	0.0	0.5
		Top PW5	0.5	-0.1	-11	0.0	0.5
		AF2	0.1	0.0	-15	0.0	0.5
La Starza	1223	Base PW2a	5.3	-4.1	-30	0.2	1.2
		Top PW2a	4.4	-3.2	-30	0.2	1.1
		AS	4.3	-3.1	-7	0.1	1.1
		Base PW2b	4.3	-3.1	-33	0.2	1.1
		Top PW2b	3.7	-2.5	-33	0.2	1.0
		AF2	2.1	-1.4	-17	0.2	0.8
		Base PW3	2.1	-1.2	-14	0.0	0.5
		Top PW3	1.9	-1.0	-14	0.0	0.5
		AF2	1.4	-0.8	-10	0.0	0.5
		Base PW4	1.4	-0.7	-12	0.0	0.5
		Top PW4	1.2	-0.6	-13	0.0	0.5
		AF2	0.6	0.0	-13	0.0	0.5
		Base PW5	0.6	-0.3	-11	0.0	0.5
		Top PW5	0.5	-0.1	-11	0.0	0.5
		AF2	0.1	0.0	-17	0.0	0.5
Rione Terra	1401	Base PW2a	5.3	-4.1	-34	0.2	1.2
		Top PW2a	4.4	-3.2	-34	0.2	1.1
		AS	4.3	-3.1	-3	0.1	1.1
		Base PW2b	4.3	-3.1	-42	0.2	1.1
		Top PW2b	3.7	-2.5	-42	0.2	1.0
		AF2	2.1	-1.4	-19	0.2	0.8
		Base PW3	2.1	-1.2	-18	0.0	0.5
		Top PW3	1.9	-1.0	-15	0.0	0.5
		AF2	1.4	-0.8	-22	0.0	0.5
		Base PW4	1.4	-0.7	-13	0.0	0.5
		Top PW4	1.2	-0.6	-13	0.0	0.5
		AF2	0.6	0.0	-21	0.0	0.5
		Base PW5	0.6	-0.3	-10	0.0	0.5
		Top PW5	0.5	-0.1	-11	0.0	0.5
		AF2	0.1	0.0	-17	0.0	0.5
Bagnoli	0905	Base PW2b	4.3	-3.1	-36	0.2	1.1
		Top PW2b	3.7	-2.5	-40	0.2	1.0
		AF2	2.1	-1.4	-20	0.2	0.8
		Base PW3	2.1	-1.2	-17	0.0	0.5
		Top PW3	1.9	-1.0	-24	0.0	0.5
		AF2	1.4	-0.8	-19	0.0	0.5
		Base PW4	1.4	-0.7	-14	0.0	0.5
		Top PW4	1.2	-0.6	-19	0.0	0.5
		AF2	0.6	0.0	-17	0.0	0.5
		Base PW5	0.6	-0.3	-12	0.0	0.5
		Top PW5	0.5	-0.1	-15	0.0	0.5
		AF2	0.1	0.0	-14	0.0	0.5
Nisida	0801	Base PW2b	3.9	-2.7	-34	0.2	1.1
		Top PW2b	3.7	-2.5	-38	0.2	1.0
		AF2	2.1	-1.4	-20	0.2	0.8
		Base PW3	2.1	-1.2	-15	0.0	0.5
		Top PW3	1.9	-1.0	-24	0.0	0.5
		AF2	1.4	-0.8	-19	0.0	0.5
		Base PW4	1.4	-0.7	-13	0.0	0.5
		Top PW4	1.2	-0.6	-20	0.0	0.5
		AF2	0.6	0.0	-17	0.0	0.5
		Base PW5	0.6	-0.3	-12	0.0	0.5
		Top PW5	0.5	-0.1	-17	0.0	0.5
		AF2	0.1	0.0	-14	0.0	0.5
Posillipo	1504	Base PW-X4	11.2	-53.0	-66	0.3	1.5
		Top PW-X4	10.6	-48.0	-66	0.3	1.5
		Base PW-X3	12.3	-62.0	-90	0.3	2.0
		Top PW-X3	11.9	-59.0	-90	0.3	2.0
Nisida Bank	026	Base PW-X3	12.3	-62.0	-90	0.3	1.5
		Top PW-X3	11.9	-59.0	-90	0.3	1.5
Penta Palummo EAST	098	Base PW-X3	12.3	-62.0	-96	0.3	2.0
		Top PW-X3	11.9	-59.0	-96	0.3	2.0
		Base PW-X2	14.9	-93.0	-110	0.3	3.0
		Top PW-X2	14.3	-90.0	-110	0.3	3.0
		Base PW-X1	20.0	-116.0	-167	0.3	5.0
		Top PW-X1	18.0	-105.0	-169	0.3	5.0
Penta Palummo WEST	044	Base PW-X4	11.2	-53.0	-70	0.3	1.5
		Top PW-X4	10.6	-48.0	-70	0.3	1.5
		Base PW-X3	12.3	-62.0	-98	0.3	2.0
		Top PW-X3	11.9	-59.0	-98	0.3	2.0
		Base PW-X2	14.9	-93.0	-115	0.3	3.0
		Top PW-X2	14.3	-90.0	-115	0.3	3.0
		Base PW-X1	20.0	-116.0	-165	0.3	5.0
		Top PW-X1	18.0	-105.0	-165	0.3	5.0
	1403	Base PW-X3	12.3	-62.0	-100	0.3	2.0
		Top PW-X3	11.9	-59.0	-100	0.3	2.0
Miseno Banks	082	Base PW-X4	11.2	-53.0	-72	0.3	1.5
		Top PW-X4	10.6	-48.0	-72	0.3	1.5
		Base PW-X3	12.3	-62.0	-102	0.3	2.0
		Top PW-X3	11.9	-59.0	-102	0.3	2.0
		Base PW-X1	20.0	-116.0	-170	0.3	5.0
		Top PW-X1	18.0	-105.0	-170	0.3	5.0
Procida	1304	Base PW-X4	11.2	-53.0	-74	0.3	1.5
		Top PW-X4	10.6	-48.0	-74	0.3	1.5
	1404	Base PW-X4	11.2	-53.0	-75	0.3	1.5
		Top PW-X4	10.6	-48.0	-75	0.3	1.5

Table S1. Seismo-stratigraphic markers dataset. PW: Prograding Wedge. AF: Aggrading Fill. U: uncertainty.

N°	Site Name	Coordinates (Lat/Long)	Sea-level marker	Age (BCE/CE)	Age (ka BP)	Paleo-sea-level (m)	Measured Elevation (m)	Tide (m)	FE (m)	Age Uncertainity (±ka)	Depth Uncertainity (±m)	R.L.	Date of surveys	Reference
1	Posillipo-Gaiola	40°47'30", 14°11'15"	FT	50 BCE-50 CE	2.00	-1.00	-3.1	-0.03	0.2	0.1	0.05	A	01/10/2009 08:20 UTC	This paper
2	Portus Julius	40°49'44", 14°05'40"	DK	37 BC	2.00	-1.00	-3.3	-0.10	0.5	0.2	0.04	C	30/10/2009 12:50 UTC	This paper
3	Pozzuoli	40°49'46", 14°06'10"	DK, BL	37 BCE	2.00	-1.00	-3.3	-0.29	0.4	0.2	0.02	B	21/06/2002 10:30 UTC	This paper
4	Portus Julius	40°49'47", 14°05'41"	RD	100 BC	2.10	-1.10	-3.3	-0.16	0.7	0.3	0.02	C	18/10/2008 13:50 UTC	This paper
5	Portus Julius	40°49'39", 14°05'37"	FT	37 BC	2.00	-1.00	-3.6	-0.20	0.2	0.1	0.02	A	10/10/2008 12:30 UTC	This paper
6	Punta Epitaffio	40°49'20", 14°04'31"	RD	100-200 CE	1.85	-0.85	-3.2	-0.01	1.0	0.3	0.05	C	07/10/2009 11:40 UTC	This paper
7	Castello di Baia	40°48'33", 14°04'58"	FT	100 CE	1.90	-0.90	-4.3	0.09	0.2	0.1	0.02	A	08/10/2009 11:10 UTC	This paper
8	Bacoli P.ta Cannito	40°48'15", 14°04'59"	FT	100 CE	1.90	-0.90	-3.6	-0.30	0.2	0.1	0.02	A	21/06/2002 11:25 UTC	This paper
9	Castello di Baia	40°48'41", 14°04'58"	DK	100 BC-100 CE	2.00	-1.00	-3.6	0.08	0.4	0.2	0.02	A	08/10/2009 09:20 UTC	This paper
10	Bacoli M. Grande	40°48'02" 14°05'00"	DK	100 CE	1.90	-0.90	-3.2	0.09	0.4	0.2	0.02	C	08/10/2009 11:10 UTC	This paper
11	Miseno-Punta	40°47'36", 14°05'15"	FT	100-200 CE	1.80	-0.85	-2.8	-0.28	0.2	0.1	0.05	A	10/10/2008 11:00 UTC	This paper
12	Capo Miseno	40°47’19” 14°05’21”	HA, BL	36-12 BCE	2.00	-1.00	-2.8	-0.20	0.4	0.2	0.02	B	30/10/2009 11:00 UTC	This paper
13	Capo Miseno	40°46'46", 14°05'25"	FT	100 BCE-100 CE	2.00	-1.00	-3.2	-0.15	0.2	0.1	0.02	A	21/06/2002 07:50 UTC	This paper
14	Miseno-Punta	40°47'13", 14°05'20"	FT	100 BCE-20 CE	2.00	-1.00	-3.2	-0.29	0.2	0.1	0.05	A	10/10/2008 10:30 UTC	This paper
15	Miseno-Miliscola	40°72'02" 14°04'58"	FT	100 CE	1.90	-0.90	-3.4	-0.11	0.2	0.1	0.05	A	30/09/2009 08:30 UTC	This paper
16	Torregaveta	40°48'48" 14°02'35"	FT	80 BCE-20 CE	2.00	-1.00	-3.7	-0.11	0.2	0.1	0.05	A	20/06/2002 14:45 UTC	This paper
17	Sorrento - Bagno dei	40°37’41” 14°22’07”	FT	50 BCE-50 CE	2.00	-1.00	-0.7	-0.12	0.2	0.1	0.02	A	09/10/2009 07:00 UTC	This paper
R1	Napoli - Porto	40°50'15.5" 14°15'18.4"	PR	50 CE	1.90	-0.90	-1.7	-0.30	0.4	0.2	0.02	B		Vacchi et al., 2018
R2	Napoli-Castel	40°49'37.0" 14°14'48.3"	FT	31 CE	2.00	-1.00	-2.4	-0.10	0.2	0.1	0.02	A		Pappone et al., 2019
R3	Posillipo-Marechiaro	40°47'41.5" 14°11'36.0"	PR	I CE	1.90	-0.90	-2.4	-0.40	0.3	0.2	0.02	B		Aucelli et al., 2019
R4	Nisida	40°47'46.1" 14°10'8.18"	PR	I CE	1.90	-0.90	-2.1	-0.20	1.0	0.2	0.02	B		Aucelli et al., 2019
R5	Serapeo	40°49'34.2" 14° 7'14.1"	FL	80 CE	1.92	-1.04	0.0		3.1	0.3	0.02	C		Bellucci et al., 2006
R6	Pozzuoli-Rione Terra	40°49'16.0" 14° 7'3.53"	PR	31 BCE-14 CE	2.00	-1.00	-3.1	-0.20	0.4	0.2	0.02	B		Aucelli et al., 2018
R7	Portus Julius	40°49'34 14° 5'41.5"	PR	37 BC-14 BCE	2.00	-1.00	-3.1	-0.20	0.50	0.20	0.02	B		Aucelli et al., 2020
R8	Procida-Punta	40°45'2.9" 14° 1'31.0"	BL	100 -0 BCE	2.05	-1.05	-4.4	-0.10	0.40	0.20	0.02	B		Putignano et al., 2014

Table S2. Archaeological markers dataset. FT: Fish Tanks. DK: Docks. RD: Roads. HA: Harbour structures. BL: Bollards. FL: Floors. PR: Piers. U: uncertainty. RL: Reliability Level.

References

Acocella, V., Funiciello, R., **1999**. The interaction between regional and local tectonics during resurgent doming: the case of the island of Ischia, Italy. Journal of Volcanology and Geothermal Research, 88, 109–123.

Acocella, V., Cifelli, F., Funiciello, R., **2001**. The control of overburden thickness on resurgent domes: insights from analogue models. Journal of Volcanology and Geothermal Research, 111, 137–153.

Acocella, V., **2007**. Understanding caldera structure and development: An overview of analogue models compared to natural calderas. Earth-Science Reviews, 85, 125–160.

Aizawa, K., Acocella, V., Yoshida, T., **2006**. How the development of magma chambers affects collapse calderas: insights from an overview, in: Troise, C., De Natale, G., Kilburn, C.R.J. (Eds.), Mechanisms of Activity and Unrest at Large Calderas. Geological Society, London, 65– 81.

Albino, F., Pinel, V., Sigmundsson, F., **2010**. Influence of surface load variations on eruption likelihood: application to two Icelandic subglacial volcanoes, Grímsvötn and Katla. Geophysical Journal International, 181, 1510–524.

Antonioli, F.; Leoni, G., **1998**. Siti archeologici e loro utilizzazione quali indicatori per lo studio delle variazioni recenti del livello del mare. Quat. Ital. J. Quat. Sci., 11, 122–139.

Antonioli, F., Anzidei, M., Lambeck, K., Auriemma, R., Gaddi, D., Furlani, S., Orrù, P., Solinas, E., Gaspari, A., Karinja, S., Kovacˇic’, V., Surace, L., **2007**. Sea-level change during Holocene from Sardinia and northeastern Adriatic (central Mediterranean Sea) from archaeological and geomorphological data. Quat. Sci. Rev. 26, 2463–2486. https://doi.org/10.1016/j.quascirev.2007.06.022

Anzidei, M., Lambeck, K., Antonioli, F., Furlani, S., Mastronuzzi, G., Serpelloni, E., Vannucci, G., **2014**. Coastal structure, sea-level changes and vertical motion of the land in the Mediterranean. Geol. Soc. Lond., Spec. Publ. 388, 453–479. https://doi.org/10.1144/SP388.20

Anzidei, M., Bosman, A., Casalbore, D., Tusa, S., La Rocca, R., **2016**. New insights on the subsidence of Lipari island (Aeolian islands, southern Italy) from the submerged Roman age pier at Marina Lunga. Quat. Int. 401, 162-173. https://doi.org/10.1016/j.quaint.2015.07.003

Arienzo, I., Mazzeo, F.C., Moretti, R., Cavallo, A., D'Antonio, M., **2016**. Open-system magma evolution and fluid transfer at Campi Flegrei caldera (Southern Italy) during the past 5ka as revealed by geochemical and isotopic data: The example of the Nisida eruption, Chem. Geol., 427, 109-124, https://doi.org/10.1016/j.chemgeo.2016.02.007

Aucelli, P.P.C., Mattei, G., Caporizzo, C., Cinque, A., Amato, L., Stefanile, M., Pappone, G., **2021**. Multi-proxy analysis of relative sea-level and paleoshoreline changes during the last 2300 years in the Campi Flegrei caldera, Southern Italy. Quat. Int. 602, 110–130. https://doi.org/10.1016/j.quaint.2021.03.039

Aucelli P.P.C., Mattei, G., Caporizzo, C., Cinque, A., Troisi, S., Peluso, F., Stefanile, M., Pappone, G., **2020**. Ancient Coastal Changes Due to Ground Movements and Human Interventions in the Roman Portus Julius (Pozzuoli Gulf, Italy): Results from Photogrammetric and Direct Surveys. Water, 12, 658. https://doi.org/10.3390/w12030658

Aucelli, P.P.C., Cinque, A., Mattei, G., Pappone, G., Rizzo, A., **2019**. Studying relative sea-level change and correlative adaptation of coastal structures on submerged Roman time ruins nearby Naples (southern Italy). Quat. Int., 501, Part B, 328–348. https://doi.org/10.1016/j.quaint.2017.10.011

Aucelli, P.P.C., Cinque, A., Mattei, G., Pappone, G., Stefanile, M., **2018**. First results on the coastal changes related to local sea-level variations along the Puteoli sector (Campi Flegrei, Italy) during the historical times. Alp. Mediterr. Quat., 31, 13–16.

Auriemma, R., Solinas, E., **2009**. Archaeological remains as sea-level change markers: A review. Quat. Int., 206, 134–146. https://doi.org/10.1016/j.quaint.2008.11.012

Becker, J.J., Sandwell, D.T., Smith, W.H.F., Braud, J., Binder, B., Depner, J., Fabre, D., Factor, J., Ingalls, S., Kim, S.-H., Ladner, R., Marks, K., Nelson, S.,Pharaoh, A., Sharman, G., Trimmer, R., von Rosenburg, R., Wallace, G., Weatherall, P., **2009**. Global Bathymetry and Elevation Data at 30 Arc Seconds Resolution: SRTM30_PLUS. Marine Geodesy 32, 355–371.

Bellucci, F., Woo, J., Kilburn, C. R. J., Rolandi, G., **2006**. Ground deformation at Campi Flegrei, Italy: implications for hazard assessment. Geol. Soc. Lond., Spec. Publ. 269, 141–157. https://doi.org/10.1144/GSL.SP.2006.269.01.09

Benassi, G., Ascione, I., **2006**. Implementation and validation of wave watch III model offshore the coastlines of southern Italy. Proceedings of OMAE2006, 25th International Conference on Offshore Mechanics and Arctic Engineering, Hamburg, Germany.

Bevilacqua, A., Flandoli, F., Neri, A., Isaia, R., Vitale, S., **2016**. Temporal models for the episodic volcanism of Campi Flegrei caldera (Italy) with uncertainty quantification. J. Geophys. Res. Solid Earth, 121, 7821–7845. https://doi.org/10.1002/2016JB013171

Branney, M., and Acocella, V., **2015**. Chapter 16 – Calderas, The Encyclopaedia of Volcanoes (Second Edition), Academic Press, 299-315. https://doi.org/10.1016/B978-0-12-385938-9.00016-X

Bruno, P.P., Rapolla, A., Di Fiore, V., **2003**. Structural settings of the bay of Naples (Italy) by seismic reflection data: implications for Campanian volcanism. Tectonophysics, 372, 193–213.

Casalbore, D., F. Falese, E. Martorelli, C. Romagnoli, Chiocci, F. L., **2017**. Submarine depositional terraces in the Tyrrhenian Sea as a proxy for paleo-sea-level reconstruction: Problems and perspective. Quat. Int. 439, 169–180. https://doi.org/10.1016/j.quaint.2016.02.027

Charlton, D., Kilburn, C., Stephen, E., **2020**. Volcanic unrest scenarios and impact assessment at Campi Flegrei caldera, Southern Italy. J Appl. Volcanol. 9, 7. https://doi.org/10.1186/s13617-020-00097-x

Cinque, A., Russo, F. Pagano, F., **1991**. La successione dei terreni di età post-Romana delle Terme di Miseno (Napoli): nuovi dati per la storia e la stratigrafia del bradisisma puteolano. Ital. J. Geosci. 110. 231–244.

Chiocci, F. L., Ridente, D., **2011**. Regional-scale seafloor mapping and geohazard assessment. The experience from the Italian project MaGIC (Marine Geohazards along the Italian Coasts). Mar. Geophys. Res. 32, 13–23. https://doi.org/10.1007/s11001-011-9120-6

Chiodini, G., Paonita, A., Aiuppa, A., Costa, A., Caliro, S., De Martino, P., Acocella, V., Vandemeulebrouck, J., **2016**. Magmas near the critical degassing pressure drive volcanic unrest towards a critical state. Nat. Commun. 7, 13712. https://doi.org/10.1038/ncomms13712

Cinque, A., Rolandi, G., Zamparelli, V., **1985**. L'estensione dei depositi marini olocenici nei Campi Flegrei in relazione alla vulcano-tettonica. Boll. Soc. Geol. Ital.,104, 327-348.

Cioni, R., Pistolesi, M., Rosi, M., **2015**. Plinian and Subplinian Eruptions in: Sigurdsson, H. (Ed.), The Encyclopedia of Volcanoes (Second Edition). Academic Press, Amsterdam, 519–535.

Cole, J.W., Milner, D.M., Spinks, K.D., **2005**. Calderas and caldera structures: a review. Earth-Science Reviews, 69, 1–26.

Columella, De Re Rustica XVII, **30 CE.**

Crosweller, H.S., Arora, B., Brown, S.K., Cottrell, E., Deligne, N.I., Guerrero, N.O., Hobbs, L., Kiyosugi, K., Loughlin, S.C., Lowndes, J., Nayembil, M., Siebert, L., Sparks, R.S.J., Takarada, S., Venzke, E., **2012**. Global database on large magnitude explosive volcanic eruptions (LaMEVE). Journal of Applied Volcanology 1, 1–13.

Deino, A. L., Orsi, G., de Vita, S., Piochi, M., **2004**. The age of the Neapolitan Yellow Tuff caldera-forming eruption (Campi Flegrei caldera – Italy) assessed by $^{40}Ar/^{39}Ar$ dating method. J. Volcanol. Geotherm. Res. 157–170. https://doi.org/10.1016/S0377-0273(03)00396-2

Del Gaudio, C., Aquino, I., Ricciardi, G. P., Ricco, C., Scandone, R., **2010**. Unrest episodes at Campi Flegrei: A reconstruction of vertical ground movements during 1905–2009. J. Volcanol. Geotherm. Res. 195, 48–56. https://doi.org/10.1016/j.jvolgeores.2010.05.014

Di Vito, M. A., Isaia, R., Orsi, G., Southon, J., de Vita, S., D'Antonio, M., Pappalardo, L., Piochi, M., **1999**. Volcanism and deformation in the past 12 ka at the Campi Flegrei caldera (Italy). J. Volcanol. Geotherm. Res. 91, 221–246. https://doi.org/10.1016/S0377-0273(99)00037-2

Di Vito, M. A., Acocella, V., Aiello, G., Barra, D., Battaglia, M., Carandente, A., Del Gaudio, C., de Vita, S., Ricciardi, G., P., Ricco, C., Scandone, R., Terrasi, F., **2016**. Magma transfer at Campi Flegrei caldera (Italy) before the 1538 AD eruption. Sci. Rep. 6, 32245. https://doi.org/10.1038/srep32245

Doglioni, C., **1991**. A proposal for the kinematic modelling of W-dipping subsections-possible applications to the Tyrrhenian-Appennines system, Terra Nova, 3, 423–434.

Evelpidou, N., Pirazzoli, P.A., Saliegec, J.F., **2011**. Submerged notches and doline sediments evidence for Holocene subsidence. Cont. Shelf Res., 31, 1273–1281.

Ferranti, L., Oldow, J. S., Sacchi, M., **1996**. Pre-Quaternary orogen-parallel extension in the Southern
Apennine belt, Italy. Tectonophysics, 260, 325–347.

Geo Marine Survey Systems B.V., **2012**. https://www.geomarinesurveysystems.com/

Guidoboni, E., Ciuccarelli, C., **2011**. The Campi Flegrei caldera: historical revision and new data on seismic crises, bradyseisms, the Monte Nuovo eruption and ensuing earthquakes (twelfth century 1582 AD). Bull. Volcanol., 73, 655-677. https://doi.org/10.1007/s00445-010-0430-3

Hernández-Molina, F.J., Fernández-Salas, L.M., Lobo, F.J., Somoza, L., Díaz del Río, V., Alveirinho Dias, J.M., **2000**. The infralittoral prograding wedge: a new largescale progradational sedimentary body in shallow marine environments. Geo-Mar. Lett. 20, 109–117. https://doi.org/10.1007/s003670000040

INGV website (https://www.ingv.it/)

Isaia, R., P. Marianelli, P., Sbrana, A., **2009**. Caldera unrest prior to intense volcanism in Campi Flegrei (Italy) at 4.0 ka BP: Implications for caldera dynamics and future eruptive scenarios. Geoph. Res. Lett. 36, L21303. https://doi.org/10.1029/2009GL040513

Isaia, R., Vitale, S., Marturano, A., Aiello, G., Barra, D., Ciarcia, S., Tramparulo, F.D.A., **2019**. High-resolution geological investigations to reconstruct the long-term ground movements in the last 15 kyr at Campi Flegrei Caldera (southern Italy). J. Volcanol. Geotherm. Res. 385, 143–158. https://doi.org/10.1016/j.jvolgeores.2019.07.012

Lambeck, K., Antonioli, F., Purcell, A., Silenzi, S., **2004**. Sea-level change along the Italian coast for the past 10,000 yr. Quat. Sci. Rev. 23, 1567–1598. https://doi.org/10.1016/j.quascirev.2004.02.009

Lambeck, K., Antonioli, F., Anzidei, M., Ferranti, L., Leoni, G., Scicchitano, G., Silenzi, S., **2011**. Sea-level change along the Italian coast during the Holocene projections for the future. Quat. Int. 232, 250–257. https://doi.org/10.1016/j.quaint.2010.04.026

Lavecchia, G., **1988**. The Tyrrhenian-Apennines system: structural setting and seismotectogenesis. Tectonophysics, 147, 263–296.

Lyell, C., **1830**. Principles of geology, 1, 511.

Malinverno, A., Ryan, W.B.F., **1986**. Extension in the Tyrrhenian Sea and shortening in the Apennines as a result of arc migration driven by sinking of the lithosphere. Tectonics 5, 227–245.

Marturano, A., Isaia, R., Aiello, G., Barra, D., **2018**. Complex dome growth at Campi Flegrei Caldera (Italy) in the last 15 ka. J. Geophys. Res. Solid Earth. 123, 8180–8197. https://doi.org/10.1029/2018jb015672

Morhange, C., Marriner, N., Laborel, J., Todesco, M., Oberlin, C., **2006**. Rapid sea-level movements and noneruptive crustal deformation in the Phlegrean Fields caldera, Italy. Geol. 34, 93–96. https://doi.org/10.1130/G21894.1

Morhange, C., Marriner, N., **2015**. Archeological and biological relative sea-level indicators. Handb. Sea Level Res., 146–156, doi:10.1002/9781118452547.ch9

Mosher, D.C., Simpkin, P.G., **1999**. Status and trends of marine high-resolution seismic reflection profiling: data acquisition. Geosci. Can., 26, 174–188.

Natale, J., Ferranti, L., Marino, C., Sacchi, M., **2020**. Resurgent dome faults in the offshore of the Campi Flegrei caldera (Pozzuoli Bay, Campania): preliminary results from high-resolution seismic reflection profiles. Bollettino di Geofisica Teorica ed Applicata, 61. https://doi.org/10.4430/bgta0315

Natale, J., Ferranti, L., Isaia, R., Marino, C., Sacchi, M. Spiess, V., Steinmann, L., Vitale, S., **2021**. Integrated on-land-offshore stratigraphy of the Campi Flegrei caldera: new insight into the volcano-tectonic evolution in the last 15 kyr. Basin Research. doi.org/10.1111/bre.12643.

Orsi, G., D'Antonio, M., de Vita, S., Gallo, G., **1992**. The Neapolitan Yellow Tuff, a large-magnitude trachytic phreatoplinian eruption: eruptive dynamics, magma withdrawal and caldera collapse. J. Volcanol. Geotherm. Res. 53, 275–287. https://doi.org/10.1016/0377-0273(92)90086-S

Paoletti, V., D'Antonio, M., Rapolla, A., **2013**. The structural setting of the Ischia Island (Phlegrean Volcanic District, Southern Italy): Inferences from geophysics and geochemistry. Journal of Volcanology and Geothermal Research, 249, 155–173.

Pappone, G., Aucelli, P. P.C., Mattei, G., Peluso, F., Stefanile, M., Carola, A., **2019**. A Detailed Reconstruction of the Roman Landscape and the Submerged Archaeological Structure at "Castel dell'Ovo islet" (Naples, Southern Italy), Geosci. 9, 170. https://doi.org/10.3390/geosciences9040170

Parascandola, A., **1947**. I fenomeni bradisismici del Serapeo di Pozzuoli. Stabilimento tipografico G, Genovese, 117.

Passaro, S., Barra, M., Saggiorno, R., Di Giacomo, S., Leotta, A., Uhlen, H., Mazzola, S., **2013**. Multi-resolution morpho-bathymetric survey results at the Pozzuoli-Baia underwater archaeological site (Naples, Italy). J. Archaeol. Sci., 40, 1268–1278.

Patacca, E., Sartori, R., Scandone, P., **1990**. Tyrrhenian basin Trincardi, F., Corregiari, A., Field, M.E., Normark, W.R., and Apenninic arcs: kinematic relations since late Tortonian 1995. Turbidite deposition from multiple sources: Quatertimes. Mem. Soc. Geol. Ital., 45, 425–451.

Pepe, F., Ferranti, L., Sacchi, M., Bertotti, G., Collura, A.M., Sulli, A., **2014**. Pattern and rate of post-20 ka vertical tectonic motion around the Capo Vaticano Promontory (W Calabria, Italy) based on offshore geomorphological indicators. Quat. Int. 332, 85–98. https://doi.org/10.1016/j.quaint.2013.11.012

Putignano, M. L., Orrù, P. E., Schiattarella, M., **2014**. Holocene coastline evolution of Procida Island, Bay of Naples, Italy. Quat. Int. 332, 115-125. https://doi.org/10.1016/j.quaint.2014.03.003

Ricco, C., Petrosino, S., Aquino, I., Del Gaudio, C., Falanga, M., **2019**. Some Investigations on a Possible Relationship between Ground Deformation and Seismic Activity at Campi Flegrei and Ischia Volcanic Areas (Southern Italy). Geosci. 9, 222. https://doi.org/10.3390/geosciences9050222

Rosi, M., Sbrana, A., **1987**. Phlegraean Fields. Quaderni de “La Ricerca Scientifica”, 114, 1–175.

Sacchi, M., Pepe, F, Corradino, M., **2014**. The Neapolitan Yellow Tuff caldera offshore the Campi Flegrei: stratal architecture and kinematic reconstruction during the last 15 kyr. Mar. Geol. 354, 15–33. http://dx.doi.org/10.1016/j.margeo.2014.04.012

Scarpati, C., Cole, P., Perrotta, A., **1993**. The Neapolitan Yellow Tuff – A large volume multiphase eruption from Campi Flegrei, southern Italy. Bull. Volcanol. 55, 343–356.

Scarpati, C., Sparice, D., Perrotta, A., **2020**. Dynamics of large pyroclastic currents inferred by the internal architecture of the Campanian Ignimbrite. Sci. rep., 10, 1-987 13. https://doi.org/10.1038/s41598-020-79164-7

Simpkin, P.G., Davis, A., **1993**. For seismic profiling in very shallow water, a novel receiver. Sea Technol., 34, 21–28.

Smith, R.L., Bailey, R.A., **1968**. Resurgent Cauldrons. Geological Society of America Memoirs, 116, 613–662.

Smith, V.C., Isaia, R., Pearce, N.J.G., **2011**. Tephrostratigraphy and glass compositions of post-15 kyr Campi Flegrei eruptions: implications for eruption history and chronostratigraphic markers. Quat. Sci. Rev. 30, 3638–3660. https://doi.org/10.1016/j.quascirev.2011.07.012

Somma, R., Iuliano, S., Matano, F., Molisso, F., Passaro, S., Sacchi, M., Troise, C., De Natale, G., **2016**. High-resolution morpho-bathymetry of Pozzuoli Bay, southern Italy. J. Maps. 12, 222-230, https://doi.org/10.1080/17445647.2014.1001800

Steinmann, L., Spiess, V., Sacchi, M., **2016**. The Campi Flegrei caldera (Italy): formation and evolution in interplay with sea-level variations since the Campanian Ignimbrite eruption at 39 ka. J. Volcanol. Geotherm. Res., 327, 361–374.

Steinmann, L, Spiess, V, Sacchi, M., **2018**. Post-collapse evolution of a coastal caldera system: Insights from a 3D multichannel seismic survey from the Campi Flegrei caldera (Italy). J. Volcanol. Geotherm. Res. 349, 83–98. https://doi.org/10.1016/j.jvolgeores.2017.09.023

Vacchi, M., Russo Ermolli E., Morhange. C., Ruello, M. R., Di Donato, V., Di Vito, M. A., Giampaola, D., Carsana, V., Liuzza, V., Cinque, A., Boetto, G., Povedag, P., Boenzif, G., Marriner, N., **2019**. Millennial variability of rates of sea-level rise in the ancient harbour of Naples (Italy, western Mediterranean Sea). Quat. Res. 60, 1–15. https://doi.org/10.1017/qua.2019.60

Varro, De Re Rustica III, **37 BCE.**

Vitale, S., and Ciarcia, S., **2013**. Tectono-stratigraphic and kinematic evolution of the southern Apennines/Calabria-Peloritani Terrane system (Italy). Tectonophysics, 583, 164–182. https://doi.org/10.1016/j.tecto.2012.11.004

Vitale, S., Isaia, R., **2014**. Fractures and faults in volcanic rocks (Campi Flegrei, southern Italy): insight into volcano-tectonic processes. Int. J. Earth Sci. 103, 801-819. https://doi.org/10.1007/s00531-013-0979-0

Vitale, S., Isaia, R., Ciarcia, S., Di Giuseppe, M. G., Iannuzzi, E., Prinzi, E. P., Tramparulo, F.D.A., Troiano, A., **2019**. Seismically induced soft-sediment deformation phenomena during the volcano-tectonic activity of Campi Flegrei caldera (southern Italy) in the last 15 kyr. Tectonics, 38, 1999-2018. https://doi.org/10.1029/2018TC005267

Woodroffe, C., **2002**. Coasts: form, process and evolution. Cambridge University Press. https://doi.org/10.5860/choice.40-6433

Zecchin, M., Catuneanu, O., **2013**. High-resolution sequence stratigraphy of clastic shelves I: Units and bounding surfaces, Marine and Petroleum Geology, 39, 1-25. https://doi.org/10.1016/j.marpetgeo.2012.08.015